DISSERTATION

PLASMA PROCESSING FOR NANOSTRUCTURED TOPOGRAPHIES

Submitted by

Nicholas Alfred Riedel

Department of Mechanical Engineering

In partial fulfillment of the requirements

For the Degree of Doctor of Philosophy

Colorado State University

Fort Collins, Colorado

Spring 2012

Doctoral Committee:

Advisor: John Williams
Co-Advisor: Ketul Popat

Donald Radford
Melissa Reynolds

ABSTRACT

PLASMA PROCESSING FOR NANOSTRUCTURED TOPOGRAPHIES

Plasma and directed ion interactions with materials have been widely observed to create complex surface patterns on a micro- and nano- scale. Generally, these texturizations are byproducts of another intended application (such as a feature formation on a sputtering target) and patterning is considered inconsequential or even detrimental. This work examined the possibility of using these phenomena as primary methods for producing beneficial topographies. Specifically, investigations focused on the use of helium plasma exposure and directed ion etching to create nanostructured surfaces capable of affecting biological interactions with implanted materials. Orthogonal argon ion etching and low energy helium plasma texturization of titanium were considered for use on orthopedic and dental implants as a means of increasing osteoblast activity and bone attachment; and oblique angle etching was evaluated for its use in creating topographies with cell deterrent or anti-thrombogenic properties. In addition, the helium driven evolution of surface features on 6061 aluminum alloy was characterized with respect to ion energy and substrate temperature. These surfaces were then considered for ice phobic applications.

ACKNOWLEDGEMENTS

Funding support for this work was supported in part by the National Science Foundation under Grant # IIP-0945996 and (CBET – 0827827), the National Institute of Dental & Craniofacial Research under grant # R43DE019975, the Colorado Office of Economic Development and International Trade, and Plasma Controls, LLC.

The author would like to thank the following people: Dan Bolchen and the staff at Garth Englund Blood Center for their assistance with drawing blood from healthy volunteers; Jack Clark of Surface Analytics, LLC for his assistance with the white light interferometry; Dr. Timothy Ruckh for his assistance with harvesting mesenchymal stem cells; Dr. Cody Farnell and Dr. Casey Farnell for their consultation and support of the ion sputtering process. The author also wishes to thank Abound Solar for the use of their contact angle testing equipment.

To my mother and father

with love

TABLE OF CONTENTS

1 Introduction

Although most matter in the universe exists as plasma, only ~150 years have passed since the first plasma was artificially created and recognized as a separate state of matter. Plasma exists as a mixture of charged particles (electrons and ions) among neutral (un-ionized) atoms or molecules. The mobility of its charged particle constituents give plasma a high electrical conductivity and allow it to respond strongly to applied electric or magnetic fields. Since its discovery, plasma has been well studied and utilized for a number of applications including: fluorescent lighting, welding and cutting, electric propulsion, and material coating or etching processes.

In this document, the impact of plasma as a means of material etching is examined. Specific focus is given to the self-organized patterns that form on a surface as a result of ion bombardment. Ion etched surfaces have been noted to evolve a number of unique patterns on the micro- and nano- scale, including: nanodots [1], nanoholes [2], and wave-like features [3]. As material engineering advances, the ability to create nano-scale patterns quickly, inexpensively, and at high volume is highly valued. Plasma processing appears to be a viable solution as large areas of material can be rapidly treated, without costly or time consuming preparations. However, the subject of ion induced patterning is still in its infancy and a deeper understanding must be attained before ion etching is viewed as a viable industrial patterning method. It is still unclear what surfaces and features can be evolved and what processing conditions are necessary. To that end, this work examines the use of argon, oxygen and helium ion bombardment to influence the physical patterning or chemical characteristics of titanium and aluminum surfaces.

2 Hypothesis and Specific Aims

Fundamental Hypothesis: Controlled plasma processing creates self-organized surfaces allowing tailored patterning of micro- and nano- scale topographical features or surface chemistries for practical industrial and biomedical applications.

Hypothesis (1): Normal incidence argon etching creates a texturization capable of improving osteoblast response on titanium surfaces.

Specific Aim 1: Argon etch titanium (Ti6Al4V) to create a hierarchical surface topography.

a) Etch the titanium surfaces with argon ions at normal incidence.
b) Characterize the physical changes to the surfaces.
c) Evaluate the ostoeblast response to the surfaces using induced differentiation in a rat marrow stromal cell primary culture.

Hypothesis (2): Oxygen etching titanium (Ti6Al4V) at oblique angles forms an oxide layer which decreases activation of the blood clotting cascade.

Specific Aim 2: Use oxygen etching to evaluate the effectiveness of titanium oxide in reducing blood clotting.

a) Etch the titanium surfaces with oxygen ions to form an oxide layer
b) Physically and chemically characterize the oxygen etched surfaces.
c) Evaluate the clotting response of the treated surfaces and compare the response to an untreated control.
d) Use whole plasma incubation to characterize platelet adhesion and activation.

Hypothesis (3): The needle like structures formed by oblique angle argon etching of titanium (Ti6Al4V) create a surface that naturally deters osteoblasts from adhering or proliferating.

Specific Aim 3: Evaluate the use of angle etching in the creation of a surface capable of decreasing cellular adherence or proliferation

a) Create a uniform surface of needle like formations on the titanium surface.
b) Physically characterize the angle etched surfaces.
c) Evaluate the physical response of hFOB 1.19 cells on the treated surfaces and compare the response to an untreated control.

Hypothesis (4): Helium plasma texturization can be used on titanium to create a surface that exhibits improved cell response over untreated titanium.

Specific Aim 4: Evaluate the use of helium plasma texturization for producing titanium surfaces capable of enhancing osseointegration.

a) Use helium texturization to create a surface on titanium that closely approximates the topographical features of natural bone.
b) Physically characterize the helium texturized surfaces.
c) Evaluate the physical response of cells on the treated surfaces and compare the response to an untreated control.

Hypothesis (5): Helium ion bombardment can be used to produce unique and controllable surface topographies on aluminum.

Specific Aim 5: Use low energy helium ion etching to create a lotus-like structure on aluminum alloys.

a) Characterize the role of ion energy in helium driven nanostructure formation.

b) Characterize the role of substrate temperature in helium driven nanostructure formation.

c) Texturize aluminum to create lotus-like surface features.

d) Evaluate the ice adhesion properties of the helium texturized surfaces.

3 Literature Review

3.1 Cellular Response to Surfaces

One of the leading causes of failure currently limiting the lifetimes of hard tissue implants such as total hip and knee replacements is aseptic loosening; often attributed to sources such as stress shielding or osteolysis from wear debris. Over the past few decades, orthopedic procedures such as hip and knee replacements have become commonplace in most developed nations. It is estimated that by the year 2015, nearly 600,000 hip replacements and 1.4 million knee replacements will be performed in the United States alone [4]. Since these operations are both painful and costly, it would be ideal if the life of the implant exceeded the lifetime of the patient. Unfortunately, these replacement joints often become loose over time and require revision surgeries to re-secure or insert new hardware. The average expected in-service life of total knee replacements ranges from 10 to 15 years before a revision is required [5].

A number of factors influence the successes of these procedures including the competency of the surgeon and the risk of postoperative infections; however, the most critical issue is the interaction between the implant and the surrounding tissue. Direct bone-implant contact appears more advantageous than a fixation with the fibrous tissue that often forms after surgery [6-7]. A weak or underdeveloped interface increases the chance the implant will loosen and a revision will be necessary [8]. In efforts to encourage healthy integration, researchers have focused on modifying the implant surfaces to enhance cellular responses in attempts to increase this osseointegration.

One of the most commonly proposed approaches to enhance implant integration is the addition of bioactive coatings. These coatings work on the premise of using chemical cues or protein bonding to promote cellular adhesion or activity. A few frequently used applications of

this technique are surface functionalization with RGD peptides (to increase integrin binding and cellular adhesion) [9-10] or coating the titanium with a calcium phosphate ceramic to mimic the environment of natural bone [11-12]. Although these techniques have met some success, there are inherent problems to surface coatings as the issues of application, adhesion, durability, and lifetime often come into question. In efforts to avoid these problems, it would be beneficial to control cell response through the introduction of engineered surfaces.

Another potential method to increase the lifetime of an implant is to enhance the affinity of the surface for bone attachment. If the surface of an implant was textured in such a way as to encourage and strengthen the initial bonding of native bone, it would be reasonable to expect the life of the implant to be extended since more time would be necessary to degrade the healthy bone-implant interface. The ultimate goal then becomes the creation of an implant surface that facilitates a bone-implant bond of sufficient strength so that aseptic loosening is no longer a concern.

It is well known that surface topographies on the micro- and nano-scale can heavily influence cellular interactions with an implanted surface [13-19]. The effects of surface structure can be observed in the regulation of cellular adhesion [20-22], bioactivity [23-24] and can even direct cellular differentiation [25]. A few methods of producing these topographies are photo lithography, colloidal lithography [26], electron beam lithography [27], ion beam lithography [28], extreme ultraviolet lithography [29], x-ray lithography [30], dip pen lithography [31], electrospinning [32-33], and anodic oxidation [34]. Although these techniques are effective and produce a variety of surfaces, most are expensive, time consuming, and difficult to translate to a complex three-dimensional structure such as an implant.

3.2 Blood Contacting Surfaces

Thrombus formation on blood contacting medical devices often leads to fibrous encapsulation capable of impeding implant function, sometimes to the point of complete failure. The formation of thrombi also produces an increased risk of embolism, where clot detachment from the material surface may have life threatening implications for patients. To date, all blood contacting devices have been shown to initiate adverse effects *in vivo* [35-36]. Efforts to improve blood compatibility of metallic devices such as stents and artificial heart valves typically focus on altering or coating the surface of the implant such that bulk properties remain unaffected. Recent studies have shown promising responses to surface modified materials including: diamond like coatings [37-39], nitric oxide releasing surfaces [40-41], superhydrophobic topographies [42-45], and titanium oxide films [46-51]. However, coatings often have issues pertaining to cracking, delamination, and overall adhesion [52]. The poor stability and limited durability of most coatings often prove to be detrimental to the long-term success of the implant; therefore the thrombogenicity of blood contacting devices remains a serious concern, eliciting a need for improved natural tissue-material surface integration.

Among the material surface treatments mentioned, titanium oxide coatings are of particular interest due to their promise for enhancing the functionality of widely used implants. Titanium and titanium alloys are often the first choice for bulk implant material, largely due to their comparatively strong biocompatible and mechanical properties. Since titanium readily forms a natural oxide on the surface of the bulk substrate, oxide coatings are particularly suited for application on this material. The improved blood compatibility of titanium oxides is believed to result from a combination of their low surface energy and their n-type semiconductor nature [50-51]. Recent studies have attributed this semiconducting behavior to limiting the charge exchange

between the proteins and the material surface, minimizing the degradation of adsorbed proteins, thereby reducing clot activation [51]. Thus, an improved oxide layer has the potential of further limiting thrombus formation on the material surface.

3.3 Helium Ion Irradiation

Helium implantation has been studied to elucidate damage mechanisms associated with helium diffusion and trapping in materials. Prior research has concentrated on two problem areas: helium formation in container materials during long term tritium storage, and mixed helium plasma exposure on wall materials of fusion reactors limiting reactor lifetime. The damage caused by helium ion irradiation has been documented on a number of materials. Defects such as holes, bubbles, and blisters have been observed on: tungsten [53-56], molybdenum [54, 57], nickel [58-59], copper [55, 59-60], beryllium [61], stainless steel [60, 62-63], titanium [60], aluminum [64-65] and niobium [63] (among many others). The cause of this damage is rooted in the unique atomic effects occurring after helium ion exposure.

As with all noble gasses, helium is chemically inert and has a near zero solubility in metals. The small size of the helium atom allows rapid diffusion as an interstitial through the crystal structure of a material [64]. However, since the electron shell of helium is completely filled, the atom can be trapped in vacancy type defects due to the low electron densities at these sites. This trapping phenomenon can occur naturally at lattice imperfections such as grain boundaries, thermal defects, or flaws induced by forced ion implantation. In addition, helium has an ability to induce self-trapping; at high enough interstitial concentrations, as few as five clustered helium atoms are capable of creating a near-Frenkel pair [66]. This results in the dislocation of an existing lattice atom, leaving a void and a stable helium cluster in its place. Thermodynamic validations of this process have been

presented for body centered cubic (bcc) and face centered cubic (fcc) structured materials [66-68]. This capability enables high fluxes of helium to generate numerous defects in otherwise pristine materials, no longer limiting collection of helium to pre-existing lattice disruptions.

Once helium has formed clusters in a crystal lattice, there is no saturation limit for void production. Binding energies are dependent on the helium-vacancy ratio rather than the physical geometry of the cluster [69-71], resulting in unabated growth and development of helium bubbles. Three additional mechanisms of bubble expansion have also been outlined: vacancy collection, Ostwald ripening, and bubble migration and coalescence [72]. In vacancy collection, bubbles can grow by assimilating thermal or damage vacancies, or build enough pressure (with estimates ranging from 10^6 [73] up to 10^{11} Pa [68]) to deform the surrounding atomic lattice and create additional vacancies through loop punching. Ostwald ripening relies on the dissolution and subsequent diffusion of helium from smaller bubbles into pre-existing larger bubbles. Bubble migration and coalescence is a mechanism where bubbles move randomly through the material under Brownian motion and collide to form larger voids. Transmission electron microscopy (TEM) investigations of helium bubble coalescence in aluminum have shown the process to be rapid, occurring in mere fractions of a second [65, 74].

In addition to the damage traditionally associated with helium exposure (bubbles, holes, and blisters), recent investigations have discovered the helium driven formation of nano-structured surfaces. Most research efforts on the effects of helium irradiation have focused specifically on tungsten and tungsten-alloys as first wall materials in fusion reactors due to favorable properties such as high melting point and low sputter yield. However, low energy helium ion bombardment of tungsten under fusion relevant conditions results in a nano-fibrous matrix (sometimes referred

to as fiberform) [60, 75-82]. An image of the helium induced fiberform structure is shown in Fig. 1 [76].

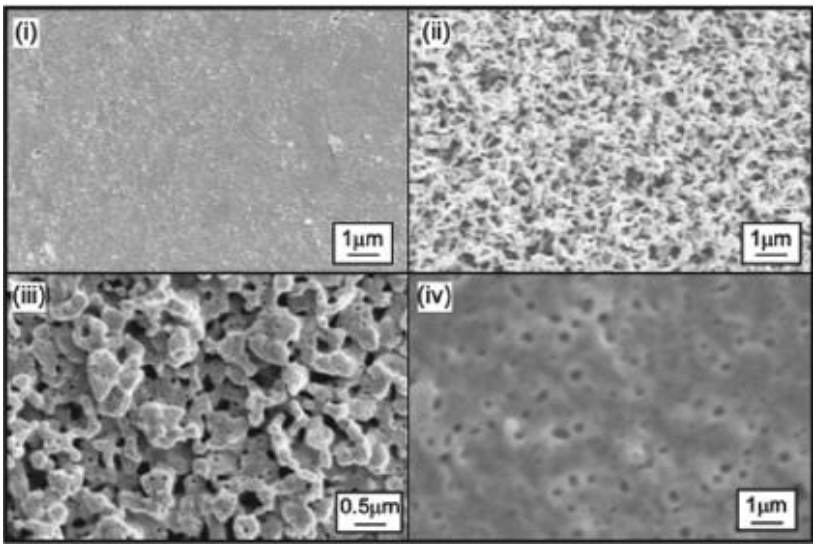

Figure 1 – This image shows tungsten under (i) low temperature helium bombardment, (ii) fiberform formation, (iii) fiberform to pinhole transition, and (iv) pinhole formation. Images (i)-(iii) were at the same helium flux with increasing temperature [76].

The creation of a fiberform structure is dependent on the material temperature, incident ion energy, and ion flux [80]. It is believed that the tungsten surface must be between 1000-2000 K, with impacting ions having energies greater than 20 eV [76]. At temperatures below 1000 K blistering or exfoliation is observed in tungsten [80], while temperatures above 2000 K result in the formation of pits and bubbles [76]. Even in the temperature range where fiberform growth occurs, the characteristics of the nanostructures themselves are also directly correlated with temperature. Most notably the diameters of individual fibers increase with processing temperature [82]. The underlying mechanisms responsible for the evolution of these surfaces are not fully understood, however, the formations are largely attributed to the affinity of implanted helium to coalesce beneath the material surface as well as to increased diffusion rates at elevated temperatures.

Fiberform is considered detrimental to the operation of reactors as fine surface structures decrease thermal conductivity, affect the material mechanical properties, and contaminate the plasma. Fusion researchers have studied helium-induced fiberform in attempts to elucidate the mechanisms of its growth and to find effective mitigation techniques. Despite the harmful nature of these surfaces in fusion reactors, helium ion irradiation may facilitate an approach to the creation of nano-engineered surfaces. Trends observed in the characteristics and topographies produced by the exposure of tungsten surfaces to helium plasma suggest that they may be controlled.

3.4 Ice Resistant Surfaces

The molecular interactions of water with a surface can be characterized by three mechanisms: covalent bonding, electrostatic interaction, and electromagnetic interaction [83-84]. The nature of these interactions is not altered by freezing, therefore the behavior of liquid water on a surface and the adhesion of ice can often be correlated. For this reason, the majority of research in the field of ice resistant surfaces has focused on the utilization of super-hydrophobic surfaces (defined as having a water contact angle larger than 150 degrees and a contact angle hysteresis of less than ~10 degrees).

Super-hydrophobic properties rely on limiting the wettability or contact of a surface with water. The amount of interaction a liquid has with a surface can be described as a balance of free energies and the subsequent surface tension relating to each interface (solid-liquid, liquid-gas, gas-solid). A balance of these interacting forces determines the amount of contact the liquid has with the solid. This is described in Young's equation:

$$\gamma_{SG} = \gamma_{SL} + \gamma_{LG} \cos\theta \qquad \text{Equation 1}$$

Where γ is the surface tension, S the solid, L the liquid, G the gas (or secondary liquid), and θ the contact angle between the solid and the liquid. Young's equation assumes these interactions take place on an ideal surface, free from any roughness or imperfection. To better describe wetting on real surfaces with roughness and imperfections, two models have been developed based on modifications to Young's equation; these are the Wenzel [85] and the Cassie-Baxter models [86]. The difference in these modes of analysis is based on assumptions that the liquid will react to surface irregularities in two distinct manners. In the Wenzel regime, although the surface is roughened, the liquid remains capable of complete contact with the solid beneath. In contrast, the Cassie-Baxter model assumes the roughness of the surface prevents complete contact between the liquid and solid by trapping gas between the two phases. These differences are illustrated in Fig. 2.

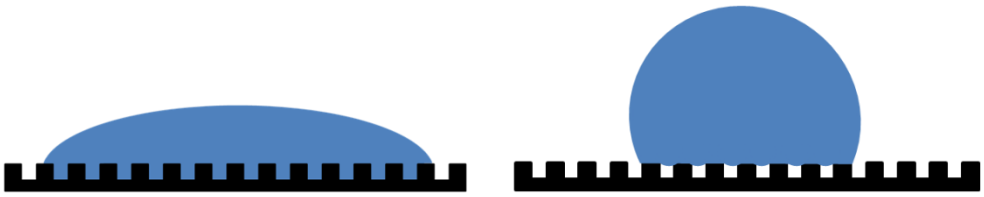

Figure 2 - This image illustrates the differences in wetting theories. (Left) Wenzel wetting model; droplet in complete contact with material surface. (Right) Cassie-Baxter wetting model; pockets of air trapped beneath droplet.

The observed properties of super-hydrophobic surfaces are a result of Cassie-Baxter wetting. Features on these surfaces trap small pockets of air beneath water to prevent complete wetting, thereby minimizing the actual contact area of the liquid/solid interface and increasing the contact angle. This reduction in contact area decreases the force or energy required to separate the droplet from the surface (lowered contact angle hysteresis).

Some of the most successful and robust super-hydrophobic surfaces are naturally occurring; the most common example of which is the lotus leaf. On these leaves, contacting water beads

into nearly spherical dimensions and will roll freely across the surface at small angles of inclination. This phenomenon is often referred to as the "lotus effect" and is highly dependent on the micro- and nano- structure that covers the leaf surface [87-89]. Fig. 3 shows this complex structure [87].

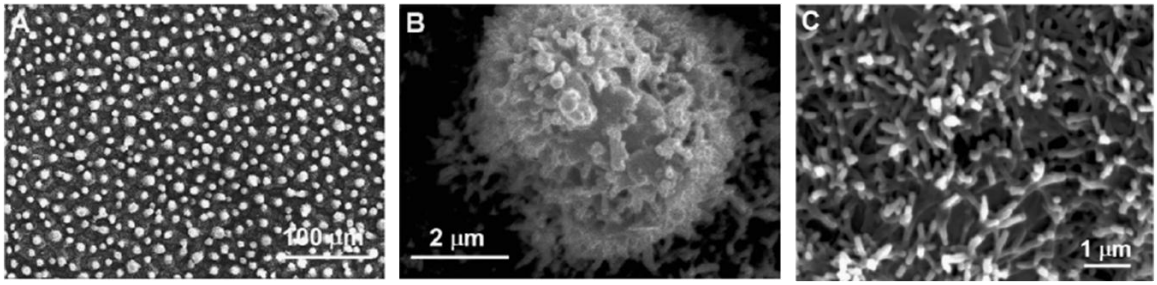

Figure 3 - The surface of a lotus leaf (Nelumbo nucifera) (A) Large scale image of the leaf surface. (B) Magnified image of a surface nodule. (C) Magnified image of the surface between the nodules [87].

This effect is not exclusive to the lotus plant and is seen to varying degrees on a number of other biomaterials. Similar properties have been observed in the wings of butterflies [90-92] and other insects [93-95], bird feathers [96], and specialized features such as the legs of water-striders [91, 97]. In each case, the super hydrophobic nature of the surface is achieved by utilizing hydrophobic materials, like oils and waxes, in combination with complex surface topographies that produce a Cassie-Baxter wetting regime.

Attempts to create synthetic super-hydrophobic surfaces by mimicking the complex surface topographies seen in nature have been very successful. When hydrophobic materials such as polytetrafluoroethylene (Teflon) [94, 98-99], polyacrylonitrile [100],or polypropylene [101-102] (among many others [103-105]) are texturized or patterned to achieve Cassie-Baxter wetting, super-hydrophobicity properties are seen. Many studies have demonstrated significant reductions in ice adhesion on hydrophobic/super-hydrophobic materials [84, 106-110]; though results have

shown that not all super-hydrophobic surfaces are necessarily ice-phobic [111-114]. Frost formation over individual features can prevent Cassie-Baxter wetting and can result in better ice adhesion than untreated surfaces due to the increased surface area provided by complex topographies [114]. These findings have demonstrated that topographical features and the consequential wetting of a surface play an integral role in ice formation and adhesion.

4 Ion Beam Etching Titanium for Enhanced Osteoblast Response

(Specific Aim 1)

4.1 Introduction

As the demand for hip and knee replacements continues to grow, researchers look to increase the operational lifetimes of these implants. Many implant failures are attributed to aseptic loosening caused from the repeated loading of these joints. It is believed that by improving the interface between the implant and natural tissue, implant life could be extended.

A less recognized method for producing an ordered nano-structured surface topography is ion etching. Broad beam ion sources are already commonplace in the field of material processing; most often they are used to sputter targets in the creation of high quality thin films. They have also been used to intentionally modify the surface of material (i.e. exposing grain size in metals that are difficult to polish and/or chemically etch to reveal grain structure [115]). More recently it has been theorized and demonstrated that ion bombardment can produce uniform, highly ordered nano-features on various materials [1-3, 116-119]. Since the topographies produced by this method are in many ways similar to the topographies produced by other tested models, it is reasonable to assume that ion bombarded surfaces may also be conducive to increased cellular adhesion and activity.

This work examines the possibility that a titanium surface bombarded at normal incidence with argon ions can produce a surface capable of increasing osteoblast activity. Although this study uses a directed ion source to texturize the substrates, the underlying theory could be easily translated to complex geometries through the use of plasma immersion techniques [120].

4.2 Materials and Methods

Substrates were prepared from 0.063”x 12”x 20” medical grade Ti6Al4V-ELI sheets (Online Metal Supply). The metal sheets were sheared with a hydraulic press into smaller substrates, approximately 1 cm x 1 cm in area. The substrates were cleaned ultrasonically in baths of Simple Green® solution, water, and finally acetone.

To etch the substrates, an 8-cm ion source was used to create a beam of energetic argon ions. The etching rate was controlled by adjusting the fluence and energy of the bombarding ions. For consistent processing, the beam current was constantly monitored and kept at 100 ± 10 mA. Since the ion distribution across the beam is not uniform, the substrates were placed on a rotating platform to ensure a uniform etch rate and equal exposure for all samples (Fig. 4). Three sets of 56 substrates were etched for five hours with ion energies of 300 eV, 700 eV, or 1100 eV. Three substrates of each preparation were used in every biological evaluation (n = 3).

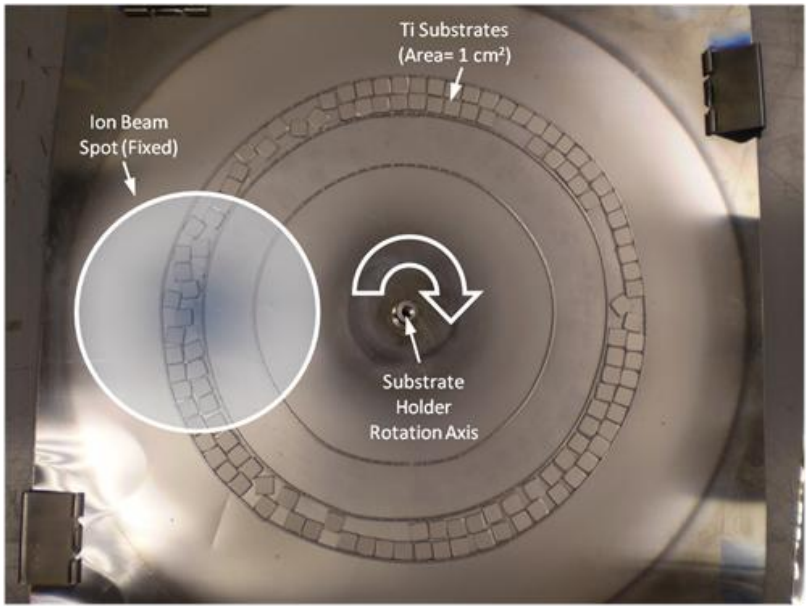

Figure 4 - Pictured is the substrate holder used during the etching of the samples. Since the ion beam is non-uniform, rotating the substrates through the beam in this manner ensures that a nearly identical path is followed by each substrate. This means the exposure time and dose of each sample is almost equal, providing a more uniform etch than setting the samples stationary under the beam.

Weight measurements from a group of substrates (n = 10) processed at each condition were taken before and after processing to calculate the etch depth. The etch rate was found using the density of Ti6Al4V-ELI (ρ = 4.42 g/cm^3), an assumed area A = 1 cm^2, the change in mass (Δm in grams), and the change in time (Δt in hours) using Equation 2:

$$\text{Etch rate}_{\text{Calc}}\ (\text{nm/hr}) = \frac{\Delta m}{\rho * A * \Delta t} * 10^7 \qquad \text{Equation 2}$$

Theoretical values were calculated using the assumptions: that ion current was 100 mA and uniform over the entire beam, beam area at the target was 16 cm in diameter (as measured from etched silhouette of the rotating platform), the density of the titanium alloy was 4.42 g/cm^3, and the substrates were only etched by the beam for one-fifth of the total time (due to the size of the rotating plate). These values were then converted to the appropriate units to provide ion current (j) in C/m^{2}s and the density of titanium (ρ) in kg/m^3. Sputter yield data (Y in atoms/ion) were taken from Yamamura and Tawara [121]. The mass of a single titanium atom (m in kg/atom) and the charge of an electron (e in C) were also necessary. The equation used for the calculations of these theoretical values is shown in Equation 3:

$$\text{Etch rate}_{\text{Theor}}\ (\text{nm/hr}) = \frac{Y * j * m}{\rho * e} \qquad \text{Equation 3}$$

4.2.1 Physical Characterization

After etching, the surfaces of the substrates were examined with a JEOL JSM-6500F scanning electron microscopy (SEM) at a working distance of 10 cm and a voltage of 15 kV. The surfaces were plated with 5 nm of gold to ensure clear imaging.

Water contact angle measurements were also performed on the as-received and etched substrates. Using a FTA1000 B Class (First Ten Angstroms, Inc.) contact angle machine, a droplet of distilled water, approximately 1.26 µL ± 0.05 µL was dropped onto each surface. Immediately after dropping, a camera level with the sample captured an image of the droplet. The image was then processed with the accompanying Fta32 software to give contact angle and droplet volume. Six samples from each preparation were tested (n=6).

4.2.2 Cell Culture

4.2.2.1 Cell Isolation

In order to evaluate the mesenchymal stem cell (MSC) interaction with the substrates, the long bones (femur, humorous, and tibia) were aseptically harvested from two adult Wistar rats immediately after euthanasia. Using scissors and sterile technique, the ends of the bones were severed and maintenance media (α-MEM with 10% fetal bovine serum (FBS, Sigma) and 1% penicillin/streptomycin (pen/strep, Sigma)) was flushed through the medullary cavity and collected. The media was then filtered through a 70 µm porous nylon filter into a clean centrifuge tube to remove any bone chips or other large unwanted debris. A hemocytometer was used to estimate the cell density of the filtered media. The celled media was then diluted to 1 million cells/mL through the addition of warmed fresh media. One mL of this concentration was

seeded on each of the substrates. Prior to seeding, the substrates were cleaned with ethanol, sterilized under an ultraviolet lamp and incubated in fresh media overnight.

4.2.2.2 Seeding and Culture

The cultures were kept incubated in a sterile environment at simulated body conditions of 37 ^{0}C and 5% CO_2. On Day 4, 0.5 mL of the media was removed from the substrates and replaced with an equal amount of fresh media. A full media change was performed on Day 7 using a differentiation media (α-MEM supplemented with 10% FBS, 1% pen/strep, Dexamethasone (10^8 M), ascorbic acid (50 mg/ml), and β-glycerolphosphate (8 mmol)) to force the differentiation of the osteoproginetor cells to an osteoblastic phenotype. This media was replaced every other day for the remainder of the study.

4.2.3 Short Term Cell Response

4.2.3.1 MTT Assay

Early cellular activity was assessed on Day 1 and Day 4 through the use of a MTT (3-[4,5-dimethylthiazol-2-yl]-2,5-diphenyl tetrazolium bromide) assay (Sigma, CGD-1). The assay protocol provided by the company was followed. MTT solution was added to the maintenance media and allowed to incubate at 37 ^{0}C for 3 hours. The mitochondrial dehydrogenases of productive cells cleaved the tetrazolium rings of the MTT solution and resulted in the formation of purple formazan crystals. These crystals were dissolved when the MTT solvent supplied in the kit was added to the solution in the wells. The substrate absorbance was measured spectrophotometrically at a wavelength of 570 nm through the use of a FLUOstar Omega (BMG

Labtech). A background absorbance measured at 690 nm was subtracted from the original reading.

4.2.3.2 Calcein AM Staining

Cell adhesion and spatial organization were assessed qualitatively through calcein AM (Invitrogen) fluorescence staining on Day 1, Day 4, and Day 7. Living cells use nonspecific cytosolic esterases to convert the non-fluorescent calcein AM to fluorescent calcein, which can then be examined. The maintenance media was aspirated and the substrates were gently rinsed with Phosphate Buffer Solution (PBS) to remove non-adherent cells. A 2 µM solution of Calcein AM diluted in PBS was added to each well. To prevent photo-bleaching, the substrates were shielded from light until cells were imaged using appropriate filters on a Zeiss Axioplan 2 fluorescence microscope (Carl Zeiss).

4.2.3.3 SEM Evaluation

Cell morphology was observed on Day 1, Day 4, and Day 7 by Scanning Electron Microscopy (SEM). To prepare the substrates, the cells were placed in a solution of 3% glutaraldehyde (Sigma), 0.1 M sodium cacodylate (Polysciences,Warrington, PA), and 0.1 M sucrose (Sigma) for 45 minutes. Substrates were then soaked in buffer containing 0.1 M sodium cacodylate and 0.1 M sucrose. The cells were then dehydrated by soaking the substrates in increasing concentrations of ethanol (35%, 50%, 70%, 95%, 100%) for 10 minutes each. Further dehydration was achieved by soaking the substrates in hexamethyldisilazane (HMDS, Sigma) for 10 minutes. Before imaging, a 5 nm gold coating was deposited on the substrates to increase conductance of the surface to improve SEM resolution.

4.2.4 Long Term Cell Response

The osteoblast responses on the substrates were assessed once a week for three weeks after the forced differentiation. The time points used for evaluation were as follows: Week 1 (14 days into the study), Week 2 (21 days), and Week 3 (28 days). SEM evaluations of the surfaces were also performed at these time points using the same methodologies previously described.

4.2.4.1 ALP Assay

Osteoblast activity was monitored through the use of an alkaline phosphatase (ALP) colorimetric assay (BioAssay Systems). The correlation between ALP and cellular activity could be made since ALP is a hydrolase enzyme produced as a byproduct of active osteoblasts. The titanium substrates were moved into fresh 24-well plates and 1 mL of a cell lysis reagent (CelLytic M, Sigma) was added to each of the wells and gently shaken for 15 minutes at room temperature. This lysis reagent was then collected and added to a solution of p-nitrophenyl phosphate and magnesium acetate, prepared to kit specifications. The ALP present in the reagent causes a conversion of the p-nitrophenyl phosphate into yellow colored product (p-nitrophenol and phosphate). The reaction rate is directly proportional to the enzyme activity. Substrates were read twice (t = 0 min and t = 4 min) with a FLUOstar Omega (BMG Labtech) at a wavelength of 405 nm to determine this rate.

4.3 Results and Discussion

4.3.1 Etched Titanium Substrate Evaluation

Figure 5 shows the SEM images taken of the processed substrates. After etching the titanium substrates with various ion energies, it was obvious that the higher the energy of the ions, the

more dramatically the surfaces were affected. Substrates etched at 300 eV showed little variation in surface topography from their pre-processed state. The low energy etching on these substrates only served to smooth the sharp imperfections created from the original manufacturing of the titanium sheets. However, the 700 eV and 1100 eV etched substrates yielded a unique topography that appeared to be highly dependent on the grain size and structure of the metal. These higher energies created hierarchical surfaces with uniform features at both the micro- and nano-scale. At the micro-scale, plateaus and valleys ranging in size from 5-15 μm were clearly distinguishable. Many edges of these features appeared to terminate at the grain boundaries of the alloy. This effect is clearly seen in Fig. 6. It has been observed previously that the orientation of the crystal structure affects how susceptible each grain is to etching [122]. Similarly, we believe that the micro-scale coarseness observed is a direct result of an uneven etching of individual grains.

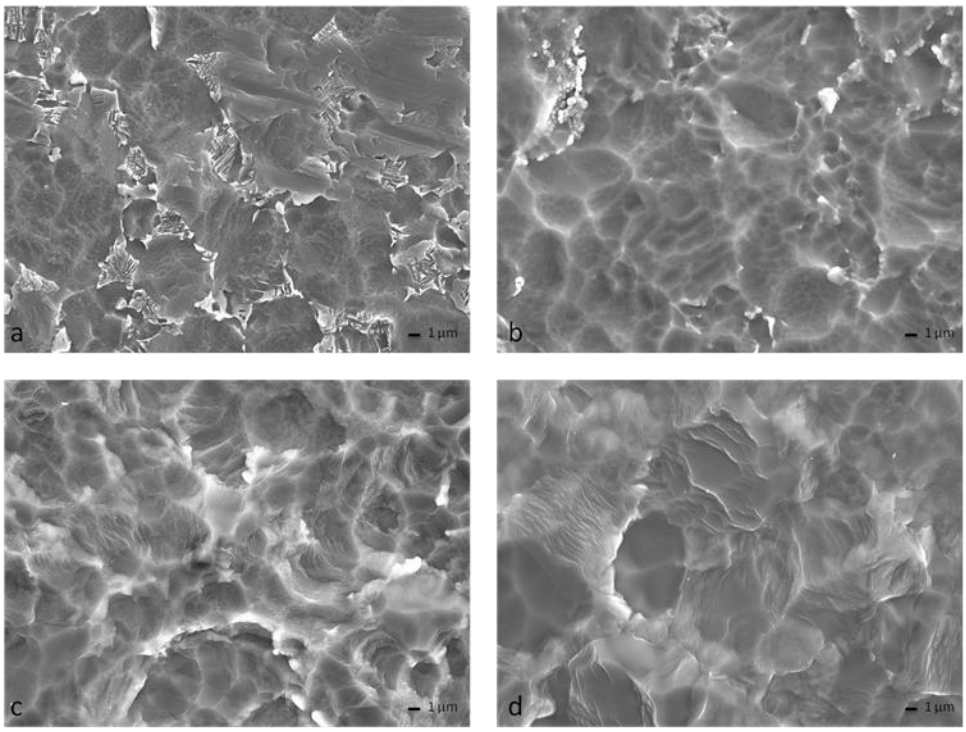

Figure 5 – These SEM images are representative of the surfaces produced by the argon etching (4000X). (a) The unmodified, as-received titanium used for processing and the study control. (b) Titanium substrate after 300 eV etch. (c) Titanium substrate after 700 eV etch. (d) Titanium substrate after 1100 eV etch.

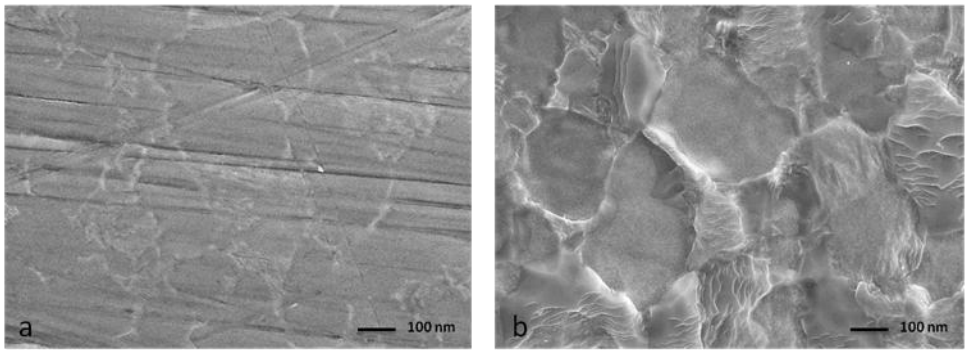

Figure 6 - SEM images comparing a polished Ti substrate (a) to a substrate etched at 1100 eV (b). The features apparent in the etched sample are of similar size and shape to the grain boundaries of the titanium observed on the polished substrate (exposed by minor chemical etch).

At the nano-scale the etching resulted in the formation of regularly spaced ripples, approximately 20 nm apart. The prominence of the nano-features was dependant on the ion energy; the higher the ion energy, the more pronounced the ripples. The 1100 eV etching consistently created well-defined ripple morphology while the 700 eV etch resulted in definition ranging from barely visible to clearly apparent. The differences in ripple morphology from the two higher ion energies are illustrated in Fig. 7. The phenomenon of wave formation has also been reported when argon was used to sputter copper [123] and silver [124]. Ripple formation on the silver substrates was noted to occur at ion energies greater than 800 eV with substrate temperatures ranging from 270-320 K [124]. In this study substrate temperature was not monitored, but the formation of ripples was only apparent on the 700 eV and 1100 eV substrates. One theory behind the evolution of ripple features has been described previously by Bradley and Harper [125].

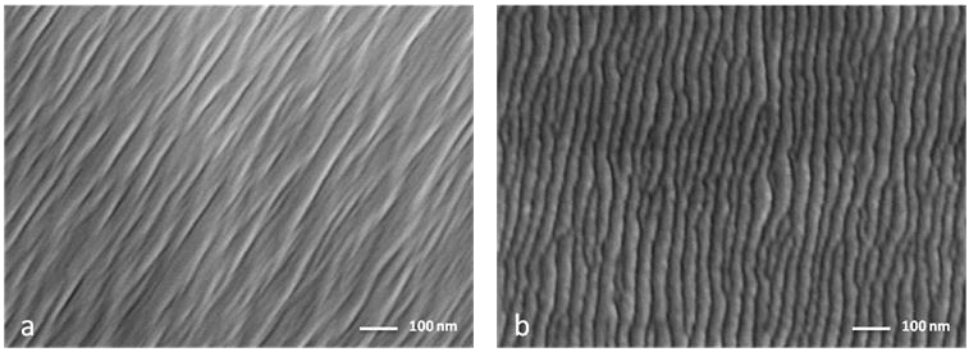

Figure 7 - SEM images of the surfaces taken at 100,000X resolution. (a) Weak ripple formation apparent on the surface of a titanium substrate etched at 700 eV. (b) Fully developed ripples formed on the substrate etched at 1100 eV.

Although these ripples were apparent over most of the etched surface, not all grains showed these formations. Fig. 8 illustrates the differences observed between two bordering grains. Again, this disparity is likely due to variations in orientation of the crystal structure of the alloy and the resulting differences in susceptibility for atomic rearrangement of the surface.

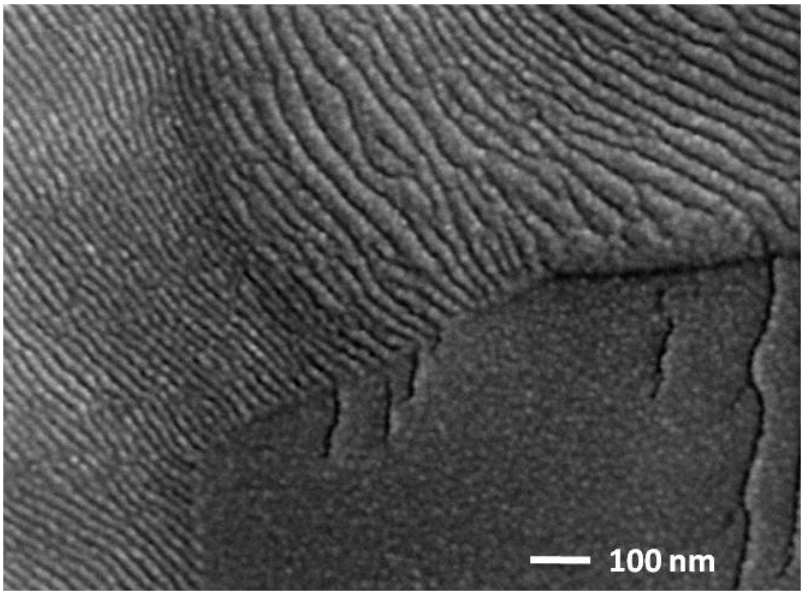

Figure 8 - This image displays the grain dependent contrast of the ripple formation produced by a 700 eV ion etch. Although the rippled nanotopography was produced across most the surface, some grains displayed a resistance. It is probable that some crystallographic orientations inhibit the bombarding ions from causing the atomic rearrangement necessary for these formations to occur.

The average change in mass measured for each ion energy was used to calculate the rate of etching. The results are shown in Table 1. Although there were discrepancies between the calculated and theoretical etch rates, this is not unexpected. The theoretical calculations were made based on the sputtering yields reported by previous researchers with varying methods of etching and measuring the sputter yields. These comparisons were made merely to ensure the results seen were reasonable. The total depth of etching during the 5 hr long process ranged from 550 nm to 2,300 nm as the ion energy was varied from 300 eV to 1100 eV. As expected, the most energetic ions resulted in the highest etch rate.

Table 1 - Calculated etch rates for the varying ion energies.

	300 eV	**700 eV**	**1100 eV**
Calculated etch rate (depth of etch)	108.6 nm/hr	162.9 nm/hr	447.9 nm/hr
Theoretical etch rate (depth of etch)	124 nm/hr	238 nm/hr	310 nm/hr

The water contact angle remained largely unaffected by the argon processing, as shown in Table 2. Since the contact angles are similar, this indicates the substrates have comparable surface energies. There should be no loss of cellular adhesion on the etched substrates due to a difference in free energy.

Table 2 - Results from the water contact angle testing.

	Control Ti	**300 eV**	**700 eV**	**1100 eV**
Contact Angle (Degrees)	54.55 ± 6.54	56.72 ± 4.06	62.85 ± 0.98	58.52 ± 2.02

4.3.2 Short Term Cell Response

The substrates were seeded with a rat MSC population to evaluate the effects of the hierarchical structure on cellular response. Short term evaluation of the MSC reactions to the surfaces began one day after seeding. Calcein AM staining indicated that the cells were able to attach and remain viable across the surface of all the substrates. Fig. 9 shows representative images of the substrates. On Day 1 the number of adherent cells was similar on all of the substrates, except the substrates etched at 1100 eV, which displayed notably fewer cells. This trend continued over Day 4 and Day 7; the substrates etched at the highest energy consistently displayed fewer adhered cells. It is likely that the rougher nature of the 1100 eV surface was

responsible. Cell densities appeared comparable on the 300 eV etched, 700 eV etched, and untreated titanium throughout the evaluation.

The cellular reactions on the 300 eV etched surfaces were similar to those of the 700 eV etched substrates. As early as Day 4, the cells on these substrates were grouping and advanced spreading was evident. By Day 7 the cells on the 300 eV and 700 eV substrates were highly spread, while most cells on the untreated titanium remained in a rounded morphology. This indicates that the topography created by argon ion bombardment at 300 eV and 700 eV had a high cellular affinity and allowed cellular migration. The nano-topography may provide increased surface area and altered protein conformations that encourage cell attachment and spreading.

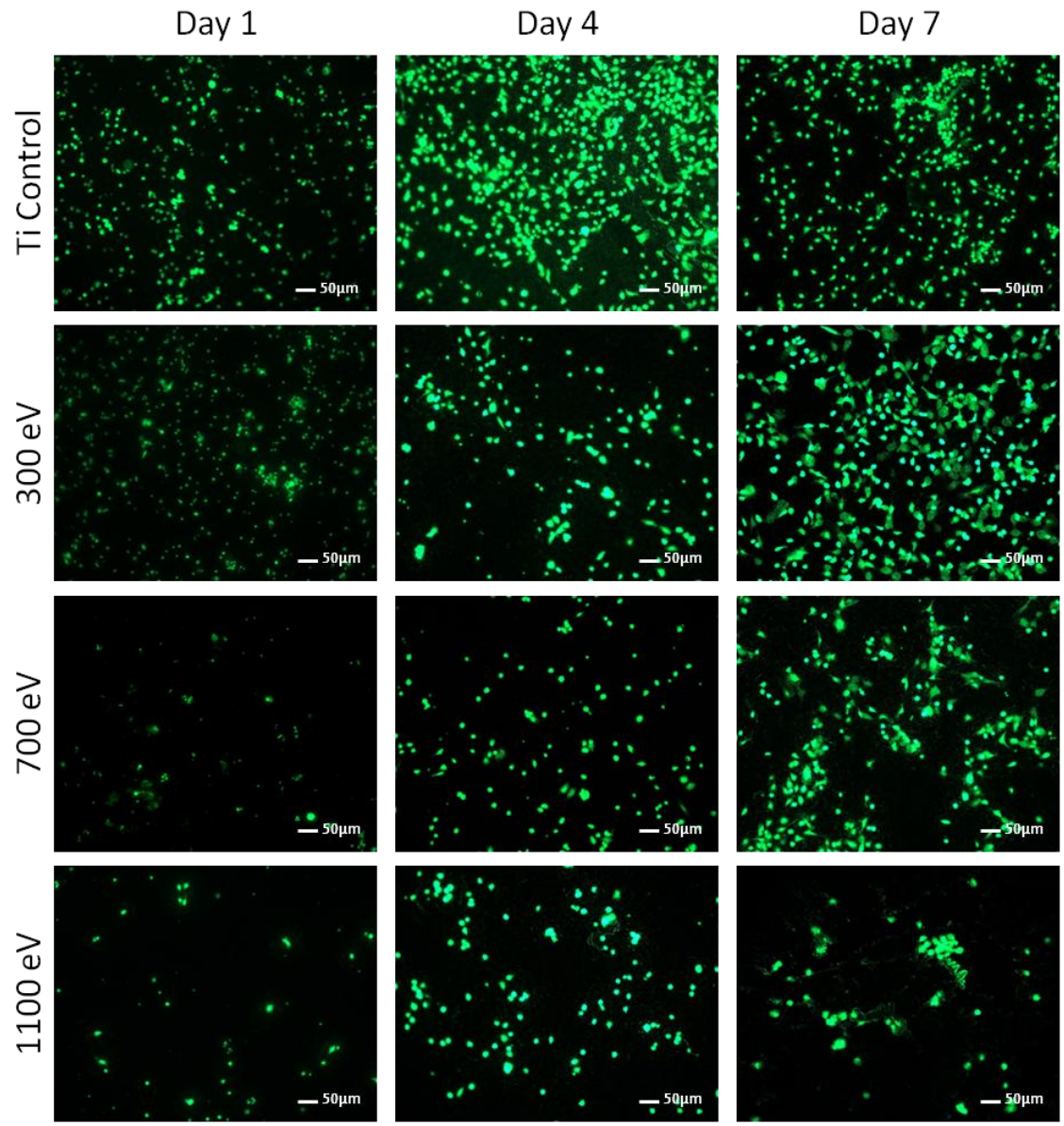

Figure 9 - These are representative images from the Calcein AM cell staining. The control group and 300 eV etched substrates maintained a fairly dense cell population through the course of the first week. Initial attachment on the 700 eV and 1100 eV substrates was not as good. By Day 7, only the 1100 eV substrate still had fewer cells than the other samples. Also by Day 7, the 300 eV and 700 eV preparations were displaying advanced spreading, while the cells on the control and 1100 eV substrates maintained a mostly rounded morphology.

The results from the MTT colorimetric assay are displayed in Fig. 10. At Day 1 there appeared to be similar mitochondrial activity on all substrates. The substrates etched at 1100 eV showed slightly more activity than those etched at the lower energies. This result is surprising given the calcein AM staining showed that the higher energy substrates appeared to maintain fewer living cells. The trend observed on Day 1 continued into Day 4. The 300 eV and 700 eV substrates had absorbance values slightly lower than those of the control, while the 1100 eV substrates performed at levels comparable to the unprocessed titanium.

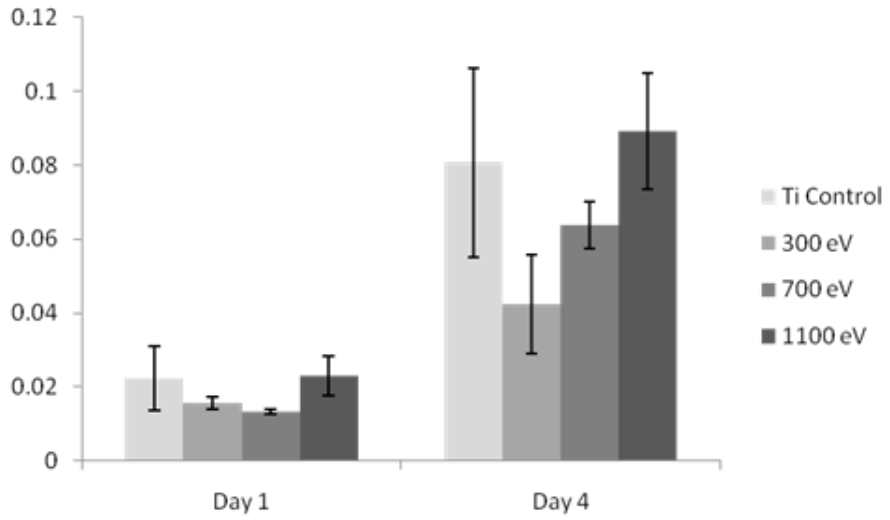

Figure 10 - MTT results for the Day 1 evaluation indicate similar cellular activity levels on all the preparations. Day 4 results display variation in the etched samples, but all levels are still comparable to the activity on the control.

Initial cellular adhesion appeared consistent for all the substrates with the cells maintaining a rounded morphology. By Day 4, the adhered cells were beginning to exhibit a spread morphology and networking with adjacent cells. Behavior was similar for all substrates except those etched at 1100 eV, which seemed to maintain rounded cell morphologies. In 7 days, cell

densities had increased and the morphology was increasingly spread. Figure 11 displays the representative images taken at Day 7. These images confirm the results seen with the Calcein staining, where the cells on the etched substrates demonstrated a higher degree of spreading and appeared to be better adhered to the surface.

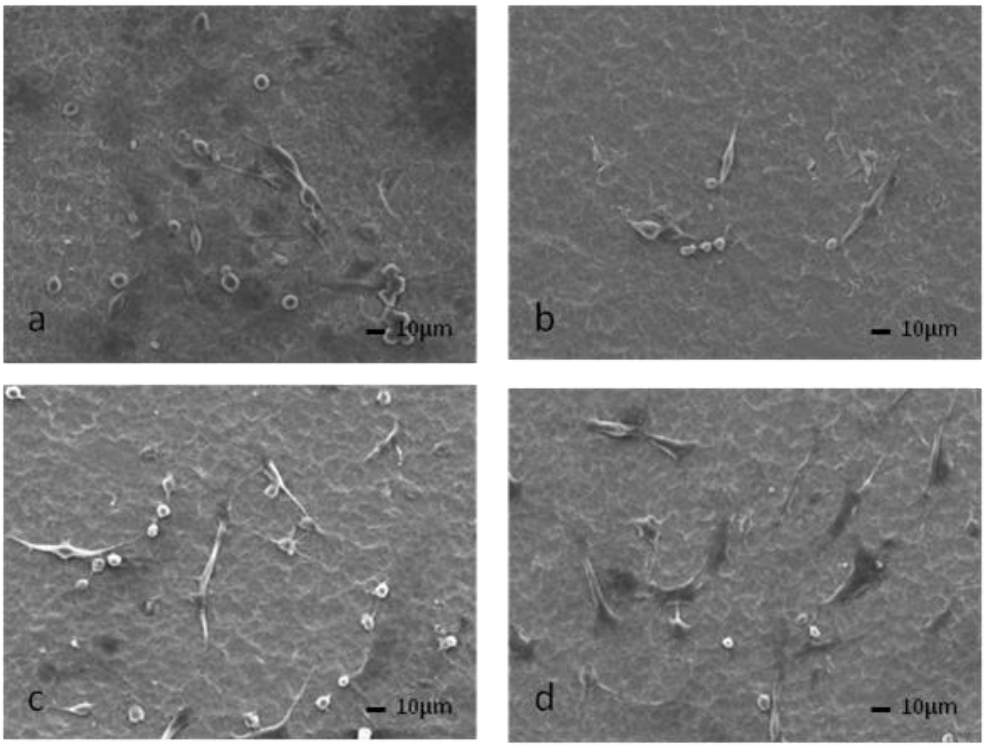

Figure 11 - Representative SEM images taken from the Week 3 evaluation of the substrates (500X). (a) Many cells on the control surface have maintained a rounded morphology. (b) The 300 eV etched substrate displayed fewer cells than the control surface, but most cells were well spread on the surface. (c) The 700 eV substrate displayed similar cell quantities to the control surface, but more cells were in a highly spread morphology typical of osteoblasts. (d) The reaction on the 1100 eV substrate was nearly identical to the reaction on the 700 eV surface.

4.3.3 Long Term Cell Response

Alkaline phosphatase (ALP), an enzyme present in the matrix vesicles deposited by osteoblasts, is thought to play a role in the induction of hydroxyapatite deposition [126]. In the

early stages of biomineralization, ALP is upregulated to supply inorganic phosphates for the mineralization process, however, once mineralization begins, the ALP levels drop before a mature mineralized matrix is formed [127]. These fluctuations in ALP levels have been observed in similar studies [128-129]. The ALP results from this study are given in Fig. 12. Although these readings are not normalized, the values can still be considered representative of osteoblast performance since SEM evaluations of the surfaces suggest similar cell quantities on almost all substrates after the first week. At all time points, the as-received substrates were consistently poor performers compared to the etched substrates. Unfortunately the errors associated with these measurements were too large to draw any definitive conclusions, though there was a perceived increase in ALP activity on all the etched samples. The as-received substrates all performed similarly while there were large variations in the etched samples. The lower values in the etched samples were similar to those seen in the untreated titanium, while the higher values were up to 5 times higher. Large standard deviations resulted from wide fluctuations in measured ALP values and low sample numbers. It is probable that the etching increases osteoblast activity, though suggestive, these results are not conclusive.

The SEM images taken over the long-term evaluation showed that cellular reactions on all surfaces were similar across the duration of the study. The substrates had cell densities that were approximately equal in number with cells exhibiting similar conformation and spreading.

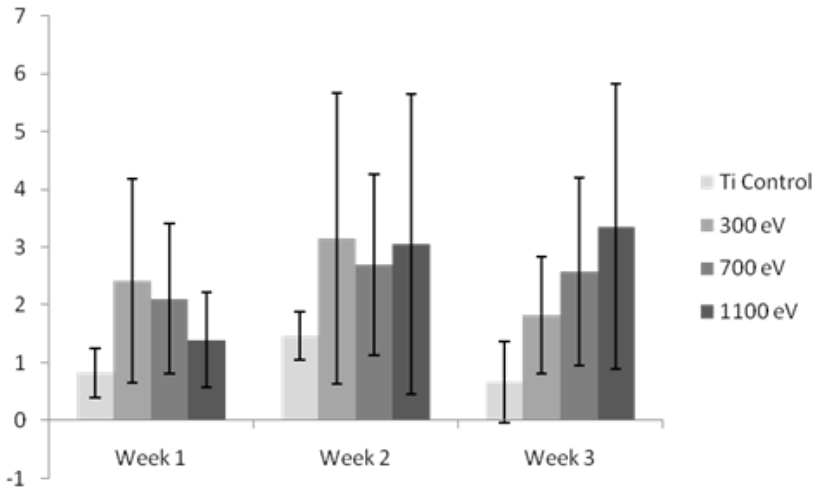

Figure 12 - ALP responses indicated higher average values on the etched substrates in all cases, however the standard deviations of the measurements were too large on the sample size of three to draw any statistically significant conclusions on whether activity was really increased (no significant statistical differences).

4.4 Conclusions

Normal incidence argon ion etching was able to produce a hierarchical topography on a titanium surface. At energies of 700 eV and 1100 eV the surfaces had plateaus and valleys ranging from 5-15 µm in diameter, while at the nano-scale regularly spaced ripples (~20 nm apart) were observed. The etching had a largely positive impact on the cellular interaction over the as-received substrates. Calcein AM staining and SEM imaging confirmed that there was an increase in early cell spreading and mobility. This is likely due to a combination of the imparted nano-texturization and the erosion of large physical obstacles by ion bombardment. The etched substrates had slightly lower but comparable MTT absorbances to the untreated as-received substrates, but the ALP values of the etched were higher. It can be concluded that the argon beam etching provided some improvement, though not dramatic, in the performance over the as-received substrates.

5 Improved Thrombogenicity on Oxygen Etched Titanium Surfaces

(Specific Aim 2)

5.1 Introduction

Thrombus formation on blood contacting biomaterials continues to be a key factor in initiating a critical mode of failure in implantable devices, requiring immediate attention. Titanium is often utilized as an implant material, due to its comparatively strong biocompatible and mechanical properties. The biocompatibility of the material is owed to the dense, inert natural oxide formed on the surface. Upon first exposure to blood, implanted materials are coated with a layer of adsorbed proteins within seconds; these proteins, and the nature of their adsorption (conformation) then determine subsequent cellular response to the surface. The nature of the titanium oxide layer is known to limit the charge exchange between the proteins and the material surface, minimizing the denaturization of adsorbed proteins, thereby reducing clot activation [51]. Therefore, an improvement to the quality of this oxide surface would result in less protein denaturation and improved thrombogenicity.

Although previously most titanium oxide coatings have been deposited as a thin film onto a bulk surface from a secondary source, the potential to dope the implant surface with oxygen and grow the oxide layer from existing material is a possible and promising approach. Oxygen plasma immersion ion implantation (PIII) has been used to produce a range of titanium oxides on titanium and may even be used to increase the thickness of the oxide layer [130-132]. If an improved oxide layer can be evolved from the existing surface of the implant, this eliminates the concerns of coating instability and can prevent premature implant failure.

This study examines the use of oblique angle oxygen ion bombardment to create a high quality oxide layer capable of enhancing the hemocompatibility of Ti6Al4V alloys. Ion beam exposure is fundamentally similar to PIII, in which ions are forced into the near surface regions of the material; however, ion beams can be oriented to varying angles whereas PIII always pulls ions perpendicular to the surface. By bombarding the surface with energetic oxygen ions at a high angle of incidence, the ions and energy of the beam are focused on the near surfaces layers. Atomic redistribution and surface mixing in an oxygen environment may produce a higher quality oxide layer potentially able to reduce thrombogenesis. Oxygen etched surfaces were compared to the unaltered titanium alloy to examine platelet adhesion and activation, whole blood clotting, and protein adsorption.

5.2 Materials and Methods

5.2.1 Fabrication and Characterization of Oxygen Etched Titanium Surfaces

Medical grade Ti6Al4V-ELI titanium alloy sheets (Online Metal Supply, Titanium Joe Inc.) were sheared into workable substrates approximately 1 cm x 1 cm. Substrates were cleaned ultrasonically for 15 minutes in baths of Simple Green® solution, water, and finally acetone. The control substrates used in this study were left unaltered. Further processing with a 16 cm ion source in a low pressure environment (approximately 1.6×10^{-4} Torr during processing) was used to create the oxygen etched surfaces. Gas flow rates through the source and neutralizer were 20 sccm O_2 and 8 sccm Ar respectively. An energetic ion beam consisting of 1200 eV ions at a beam current of 200 mA was used for a 3 hour etch. This beam consisted primarily of oxygen ions, though it is possible small amounts of Ar gas diffusing into the source from the

vacuum chamber were ionized and extracted with oxygen ions. The titanium alloy substrates being etched were placed on an inclined holder so the resulting angle of ion incidence was approximately 75 degrees from the surface normal. Mass measurements were taken before and after etching from 5 randomly placed substrates and used to estimate the depth of etching.

Surface architectures for the oxygen etched and control substrates were evaluated using a scanning electron microscope (SEM, JEOL JSM-6500F). The substrates were imaged without gold coating at 15 keV with a working distance of 10 mm.

The contact angle of distilled water was evaluated by a commercially available goniometer (FTA1000 B Class, First Ten Angstroms, Inc.). A fixed syringe was used to build a droplet above the substrate being tested. Water was carefully added until the droplet pulled free of the syringe needle and fell onto the material surface. Syringe height was adjusted so the droplet fall was no more than 3mm. Contact angles from oxygen etched and control surfaces (n=5) were measured at both the time of drop and 5 minutes after the drop had contacted the surface.

Substrate surface chemistry was evaluated by X-ray photoelectron spectroscopy (XPS). Analysis was conducted on an ESCA Systems X-ray Photoelectron Spectrometer 5800 with a monochromatic Al-Kα-X-ray small spot source (1486.6eV) and multichannel detector. A concentric hemispherical analyzer (CHA), operated in constant analyzer transmission mode, was used to measure the binding energies of emitted photoelectrons. Survey spectra were collected from 0 to 1100 eV with a pass energy of 187.85 eV, and high-resolution spectra were collected for C1s, O1s, and Ti2p peaks with a pass energy of 10 eV. The XPS measures the composition of an area on the surface approximately 400 μm X 700 μm. To compensate for residual charging effects, all spectra were referenced by setting the hydrocarbon C1s peak to 284.8 eV. Data for

percent elemental composition, elemental ratios and peak fit analysis parameters were calculated using Multipack software.

5.2.2 Whole Blood Plasma Incubation on Oxygen Etched Titanium Surfaces

Whole blood from 3 healthy individuals, acquired through venopuncture, was drawn into standard 6 ml vacuum tubes coated with the anti-coagulant, ethylenediaminetetraacetic acid (EDTA). The first tube was discarded to account for the skin plug and locally activated platelets resulting from the needle insertion. The blood vials were centrifuged at 150 g for 15 mins to separate the plasma from the red blood cells (erythrocytes). The plasma was transferred into fresh tubes and used within 2 hrs of removal from the body.

Sterilized substrates were placed in a 24-well plate and incubated with 500 µl of whole human plasma on a horizontal shaker plate (100 rpm) for 2 hrs, at room temperature. Additional analysis was performed to determine the effect of the material surfaces on whole blood plasma components.

5.2.3 Platelet Adhesion on Oxygen Etched Titanium Surfaces

Platelet adhesion was characterized by staining surface-adherent cells with calcein AM live stain. Prior to staining, unadhered platelets were removed by aspirating the whole human plasma followed by two gentle rinses with PBS. The substrates were further incubated with 3 µM calcein-AM solution in PBS for 10 mins at room temperature and imaged using FITC MF101 Green filters with a fluorescence microscope (Zeiss).

Platelet viability was additionally investigated using a commercially available MTT assay kit (Sigma). The MTT assay measures mitochondrial activity of live cells via dehydrogenase

activity. Prior to measuring the MTT activity, the unadhered platelets were removed by aspirating the whole human plasma from the substrates followed by two gentle rinses with PBS. Substrates were incubated with 10% MTT solution in PBS for 3 hrs at 37^{o}C and 5% CO_2. The formazan crystals created by active cells were dissolved by adding MTT solvent, equal (1:1) to the MTT solution. Absorbance of the solution was measured at a wavelength of 570 nm using a plate reader (BMG Labtech). Net absorbance was calculated by subtracting the background absorbance at 690 nm.

5.2.4 Platelet Activation on Oxygen Etched Titanium Surfaces

SEM imaging was used to visualize the platelet activation on oxygen etched and control surfaces. Un-adhered cells were removed by aspirating the whole human plasma from the substrates followed by two gentle rinses with PBS. Adhered cells were fixed and dehydrated on the substrate surfaces prior to imaging. The cells were fixed by incubating the substrates in a solution of primary fixative (6% gluteraldehyde (Sigma), 0.1 M sodium cacodylate (Polysciences), and 0.1 M sucrose (Sigma)) for 45 mins. This was followed by incubation in a solution of secondary fixative (primary fixative without gluteraldehyde) for 10 mins; and consecutive solutions of increasing ethanol concentrations (35%, 50%, 70% and 100%) for 10 mins each. Additional dehydration was accomplished by incubating the substrates in a solution of hexamethyldisilazane (HMDS, Sigma) for 10 mins. Substrates were then air dried and stored in a desiccator until imaged. Prior to imaging, the substrates were coated with a 10 nm layer of gold and imaged at 15kV using a SEM (JOEL JSM 6500F). SEM images were further evaluated to identify the effects of material surface composition on platelet activation. The following

guide was used to determine the morphology and subsequent degree of activation of the adhered platelets:

- Unactivated: Platelets that are normal with a compact central body
- Short-dendritic: Platelets with smaller dendrites and partially activated
- Long-dendritic: Platelets with many long dendrites and completely activated

5.2.5 Whole Blood Clotting on Oxygen Etched Titanium Surfaces

To better understand the thrombogenic effects of oxygen etched titanium, the material-whole blood interaction was evaluated and compared to the control substrates. Whole human blood from healthy individuals was drawn, and immediately 5 μl was dropped onto the oxygen etched and control surfaces in a 24 well plate. The blood was allowed to clot on the substrates for time periods of 15, 30 and 45 mins, after which time the free hemoglobin concentration was measured. To measure the amount of free hemoglobin, the substrates were transferred into 24 well plates with 500 μl of DI water, gently agitated for 30 secs and were left in the DI water for the remainder of 5 mins to release free hemoglobin from the whole blood that was not trapped in the clot. The absorbance of the solution was measured at 540 nm using a plate reader and was plotted against time. The value of absorbance is directly proportional to the concentration of free hemoglobin. Increased amounts of free hemoglobin can be related to a reduction in whole blood clotting on the substrates.

5.2.6 Protein Adsorption on Oxygen Etched Titanium Surfaces

The interaction between key blood serum proteins with oxygen etched and control surfaces were investigated using fibrinogen (FIB), albumin (ALB) and immunoglobulin-G (IgG)

adsorption. Prior to adsorption, all the substrates were sterilized by ultraviolet light exposure while in 70% ethanol for 30 mins, followed by two washes with phosphate buffer saline (PBS). Substrates were incubated in 24 well plates with a 100 µg/ml solution of FIB, ALB or IgG in PBS on a horizontal shaker plate (100 rpm) for 2 hours at room temperature. Following incubation, the protein solution was aspirated and substrates were gently rinsed three times with PBS to remove non-adherent proteins. Protein adsorption was measured using a commercially available bicinchoninic acid assay (BCA, Pierce Biotechnology) and XPS.

To measure the protein adsorption using the BCA assay, the substrates were incubated with 1% sodium dodecyl sulfate (SDS) solution in PBS on a horizontal shaker plate (100rpm) for 1 hr. Following the incubation, the SDS solution with solubilized proteins was collected from each well. This SDS incubation was repeated two additional times and the resulting SDS solution was pooled. The concentration of total adsorbed protein in the pooled SDS solution was then measured colorimetrically using a commercially available BCA assay. Through a protein mediated reduction reaction in an alkaline environment, the protein and assay solution react with each other to produce a chelation exhibiting a strong absorbance at 562 nm. Thus, by measuring absorbance, the concentration of the protein can be determined. Manufacturer provided instructions were followed and the absorbance of the solution was measured at 562 nm using a plate reader. The protein concentration was evaluated in comparison to standard curves for albumin, fibrinogen and immunoglobulin-G. Protein adsorption on the test surfaces was further characterized using XPS, where survey and high resolution scans were used to determine the surface composition of adsorbed proteins and characteristic peaks of adsorbed proteins on oxygen etched titanium and the control surfaces.

5.2.7 Statistical Analysis

Unless otherwise noted, all quantitative results were reconfirmed on at least three different substrates from at least three different plasma populations (n_{min} = 9) and analyzed using ANOVA. Statistical significance was considered at $p < 0.05$. During the analysis, variances among each group were not assumed to be equal and a two sample t-test approach was used to test the significance between the oxygen etched and control surfaces.

5.3 Results and Discussion

5.3.1 Fabrication and Characterization of Oxygen Etched Titanium Surfaces

The architecture of the oxygen etched surface was examined for uniformity and repeatability through SEM imaging (Fig. 13). Oxygen etched substrates showed a consistent morphology across the material surface; features apparent on the control surface had been smoothed and replaced by a scale-like architecture. These changes in topography are characteristic of oblique angle ion etching as observed previously with a variety of materials under similar etching conditions [133-134]. Weight measurements taken from oxygen etched samples indicated an average loss of 0.00038 g. Assuming a substrate area of 1 cm^2 and a density of 4.506 g/cm^3, approximately 850 nm of titanium alloy was sputtered away. The 3 hour processing time was chosen arbitrarily to ensure a steady-state etching condition and repeatable feature formation. This depth of etch is likely excessive suggesting that the etching time could be reduced without compromising the quality of the surface.

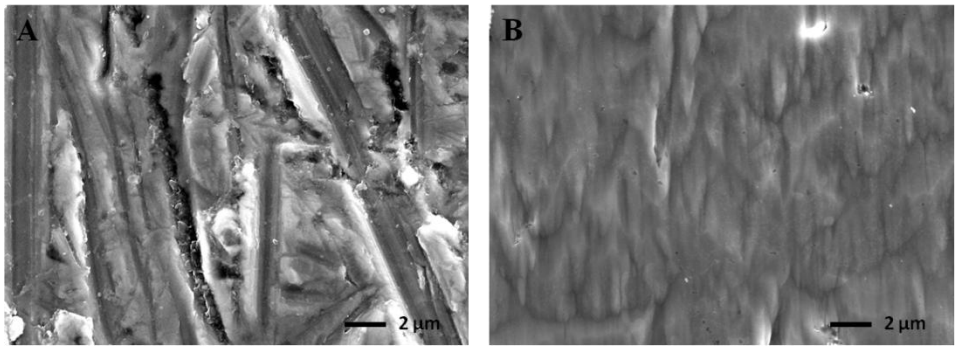

Figure 13 - Representative SEM images (5000× magnification) showing the control substrates (left) and the uniform patterning of plasma-treated titanium surfaces (right).

Changes in surface energy caused by the oxygen etching were assessed by water contact angle measurements. In brief, a droplet of DI water was formed with a fixed syringe until gravity detached the droplet displacing it onto the surface of the material. Images were captured immediately after the droplet contacted the surface and contact angles were analyzed and calculated by the Fta32 software that accompanied the goniometer. The results indicate the contact angle of the control surface was 45.9 ± 5.9 degrees, while the oxygen etched surface yielded a contact angle of 65.4 ± 1.7 degrees. It is commonly accepted that blood compatibility is improved when the hydrophilicity of a surface is increased (unless the surfaces are superhydrophobic) [42, 135-136]. The oxygen etched substrates had a significantly higher contact angle than the control titanium, indicating that etching decreased the surface energy of the substrates. This difference could be attributed to changes in either surface topography or chemistry. Traditional assumptions of increased hydrophobicity would suggest that the oxygen etched substrates should exhibit worse blood compatibility compared to the control substrates. However, the findings of this study (as later discussed) indicate an improvement in blood interactions for the oxygen etched surfaces.

To assess changes in surface chemistry, substrates were characterized by XPS to determine elemental composition (Fig. 14). Results of the high resolution Ti2p scan identify peaks at 458.7eV and 464.6 eV, both of which are attributed to TiO_2. The higher peaks of the oxygen etched surfaces indicate an increase in surface oxide concentration. In the high resolution O1s scan, the primary oxygen peak at 530.1 eV is characteristic of TiO_2. The broadened tail of this peak on the control surface is attributed to signal additions from the adsorbed water on the surface of the material (~ 531.6 eV) and hydroxyl peaks (~ 533.3 eV) [137]. The sharper O_2 peak present on the oxygen etched surface may indicate not only a reduction in OH groups but a shift to a more stoichiometric oxide and a reduction in lattice defects [137-138]. Together, these results are a clear indication of an increased degree of oxidation of the oxygen etched material surface.

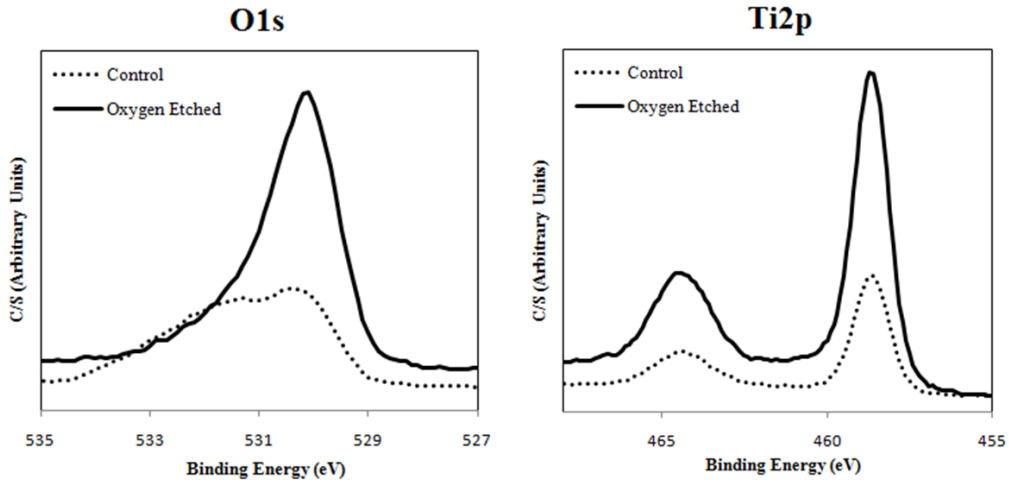

Figure 14 - High resolution XPS scans for oxygen-etched titanium and control surfaces showing elemental composition. The O1s scan indicates a sharper TiO2 peak (530.1 eV) and a reduction in OH bonds (533.3 eV) on the oxygen etched surfaces. High resolution Ti2p scans show more pronounced TiO_2 peaks.

5.3.2 Platelet Adhesion on Oxygen Etched Titanium Surfaces

Platelet adhesion and activation are strong indications of the thrombogenicity of biomaterials and are therefore key factors in determining further biomaterial integration, rejection and additional foreign body responses *in vivo* [139]. In this study, platelet adhesion was evaluated on oxygen etched and control substrates using whole blood plasma for up to 2 hours of incubation. Whole blood plasma is comprised of two main components: platelets and leukocytes, which drive the thrombogenic response *in vivo*. Adhered cells were stained with calcein-AM to allow clear visualization on the material surfaces. Low-magnification (10× and 20×) fluorescence microscopy images show a reduction in platelet adhesion on oxygen etched titanium (Fig. 15). This is likely due to the increased quality of the oxide on the oxygen etched surface, resulting in fewer activation sites for the cells. However, the opposite is readily apparent on the control substrates, with nearly confluent platelet coverage. Further, high-magnification (50×) images identify minimal platelet aggregation and activation on oxygen etched titanium as shown by the reduced degree of dendritic extensions on the adhered cells. The fluorescence microscope images were further analyzed for total cell coverage using the ImageJ software (Fig. 16). These results indicate an approximate 33% decrease in cell coverage on oxygen etched titanium from that on the control substrate. The clear reduction in both platelet and leukocyte activation on oxygen etched titanium potentially identifies the material surface as one eliciting well controlled thrombogenic effects.

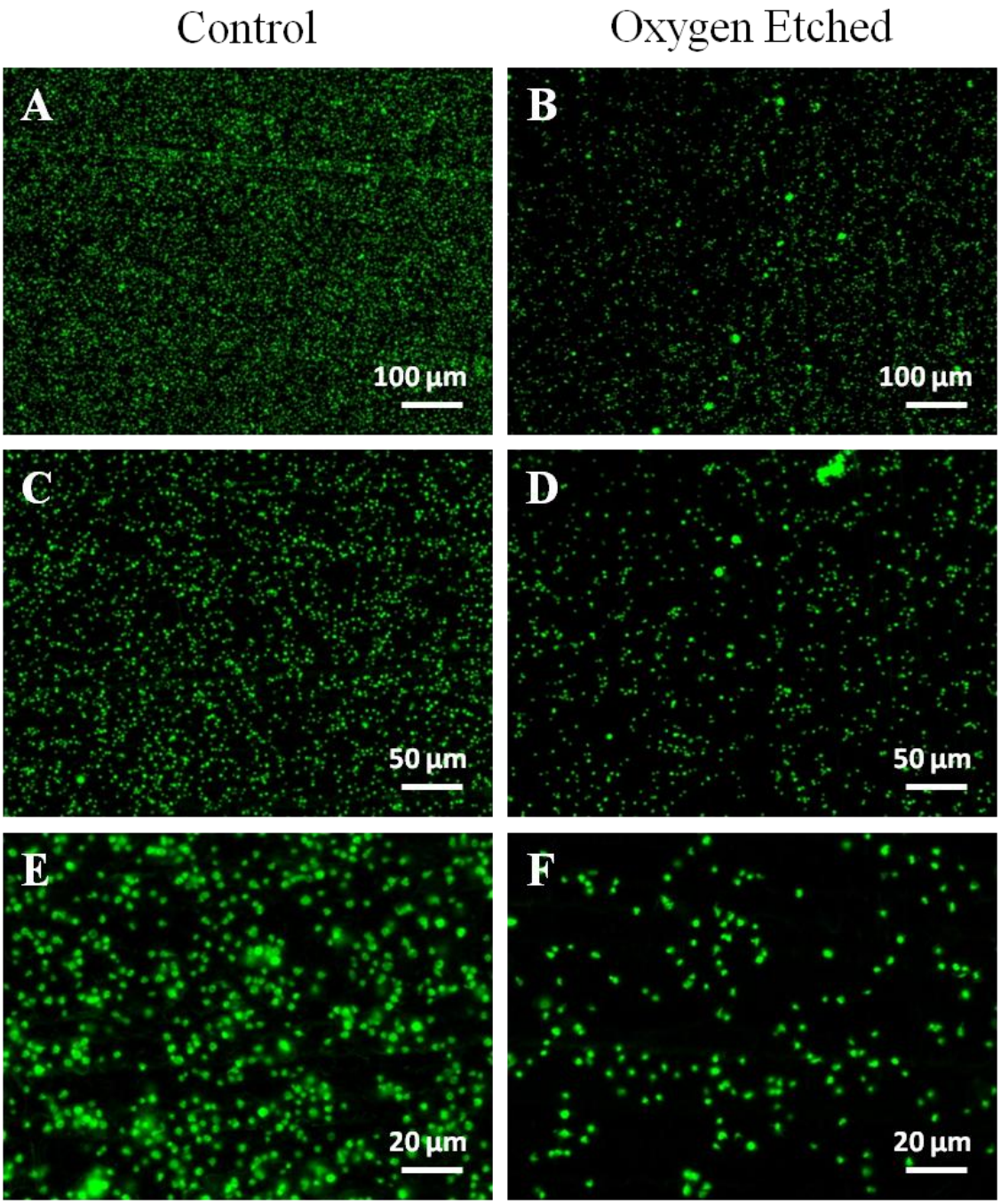

Figure 15 - Representative fluorescence microscopy images of adhered platelets and leukocytes stained with calcein-AM on the oxygen-etched titanium and control surfaces after 2 hours of incubation in whole blood plasma. The images show a decrease in platelet and leukocyte adhesion on oxygen-etched titanium.

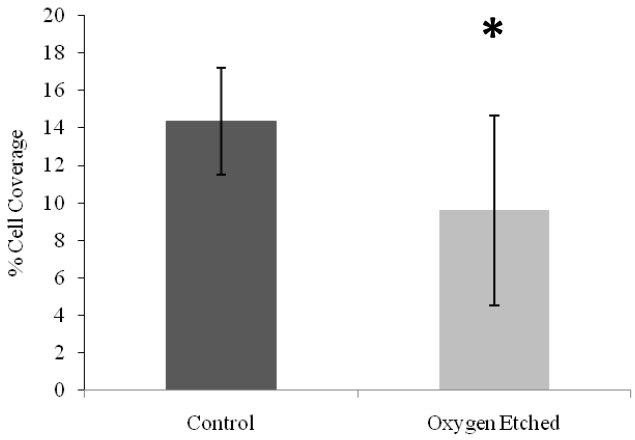

Figure 16 - Cell coverage calculated using the fluorescence images and the Image J software. The results indicate a significant 33% decrease in total cell coverage on oxygen-etched titanium over the control surfaces ($p \leq 0.05$).

Cellular viability was quantitatively measured using a commercially available MTT assay (Fig. 17). Spectrophotometric measurements were used to determine the amount of mitochondrial activity via dehydrogenase activity. These results indicate that the adhered platelets and leukocytes on oxygen etched titanium displayed a slight increase in short-term viability from that on the control substrate for up to 2 hrs of contact time. The minor increase in cell viability on the oxygen etched surfaces may be explained by the preferential adherence of leukocytes. Leukocytes, also known as white blood cells (WBC) include cells such as monocytes and neutrophils, which are at least two times larger than unactivated platelets. Leukocyte adhesion follows platelet adhesion and activation. It is possible that the increased size and nuclei of leukocytes translate to increased mitochondrial activity. Therefore, although the oxygen etched substrates had fewer adhered cells in total, increased leukocyte adherence could account for the higher degree of cellular activity as observed here. This behavior is also evident from SEM images (as discussed in the next section). However, this study is focused primarily on the platelet response due to its direct correlation with overall blood-compatibility.

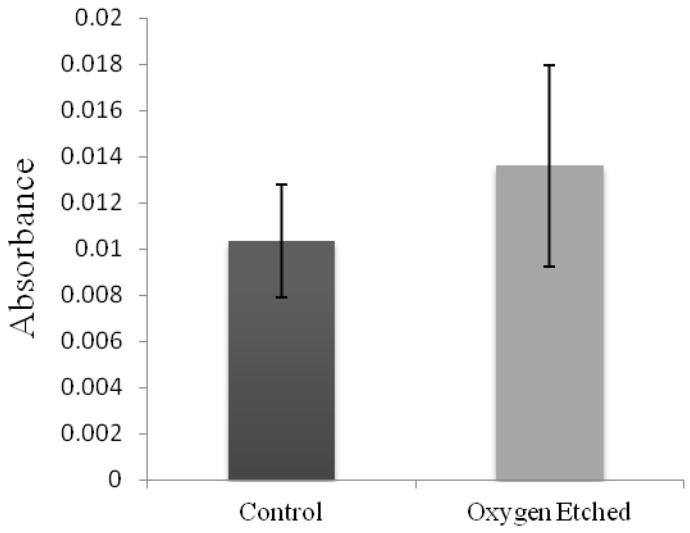

Figure 17 - Cell viability measured using an MTT assay for adhered platelets and leukocytes on oxygen-etched titanium and control surfaces. Cellular viability is higher on oxygen-etched titanium surfaces (though not significant).

5.3.3 Platelet Activation on Oxygen Etched Titanium Surfaces

Cellular interactions with their environment (including cell-cell and cell-extracellular stimulation), result in morphological changes that can be visualized by SEM imaging. Platelet adhesion, activation, aggregation, morphology and subsequent interactions with the oxygen etched titanium surface were investigated after 2 hrs of incubation in whole human plasma (Fig. 18). Low magnification (1000×) SEM images show reduced cellular adhesion and activation on oxygen etched titanium as compared to the control substrate. High magnifications (2500× and 10,000×) indicate a decrease in platelet activation on oxygen etched substrates as compared to the control substrates. Further, the images show increased amounts of leukocytes adhered on oxygen etched substrates; however, there is minimal platelet-leukocyte interaction as compared to controlled substrate. The platelets also exhibit a dendritic morphology on the control

substrates, indicating significant activation. Such behavior is less apparent on oxygen etched substrates.

The SEM images were further evaluated to determine the percentage of the adhered platelets that were unactivated and had a short-dendritic or long-dendritic morphology (Fig. 19). The results indicate greatly reduced activation of platelets on the oxygen etched substrates, where the majority of the platelets had a short-dendritic morphology (~42%) suggesting incomplete activation, followed by platelets that were unactivated (~30%), and fewer platelets with a long-dendritic morphology (~28%) suggesting complete activation. The majority of the platelets on the control substrates displayed a short-dendritic morphology (~51%), followed by platelets with a long-dendritic morphology (~44%), and fewer unactivated platelets (~5%). These results indicate a significant reduction of ~20% of short-dendritic platelets and a significant reduction of ~36% in long-dendritic platelets on oxygen etched titanium as compared to the control substrate. This suggests a significant reduction in platelet activation on oxygen etched substrates as compared to the control substrates.

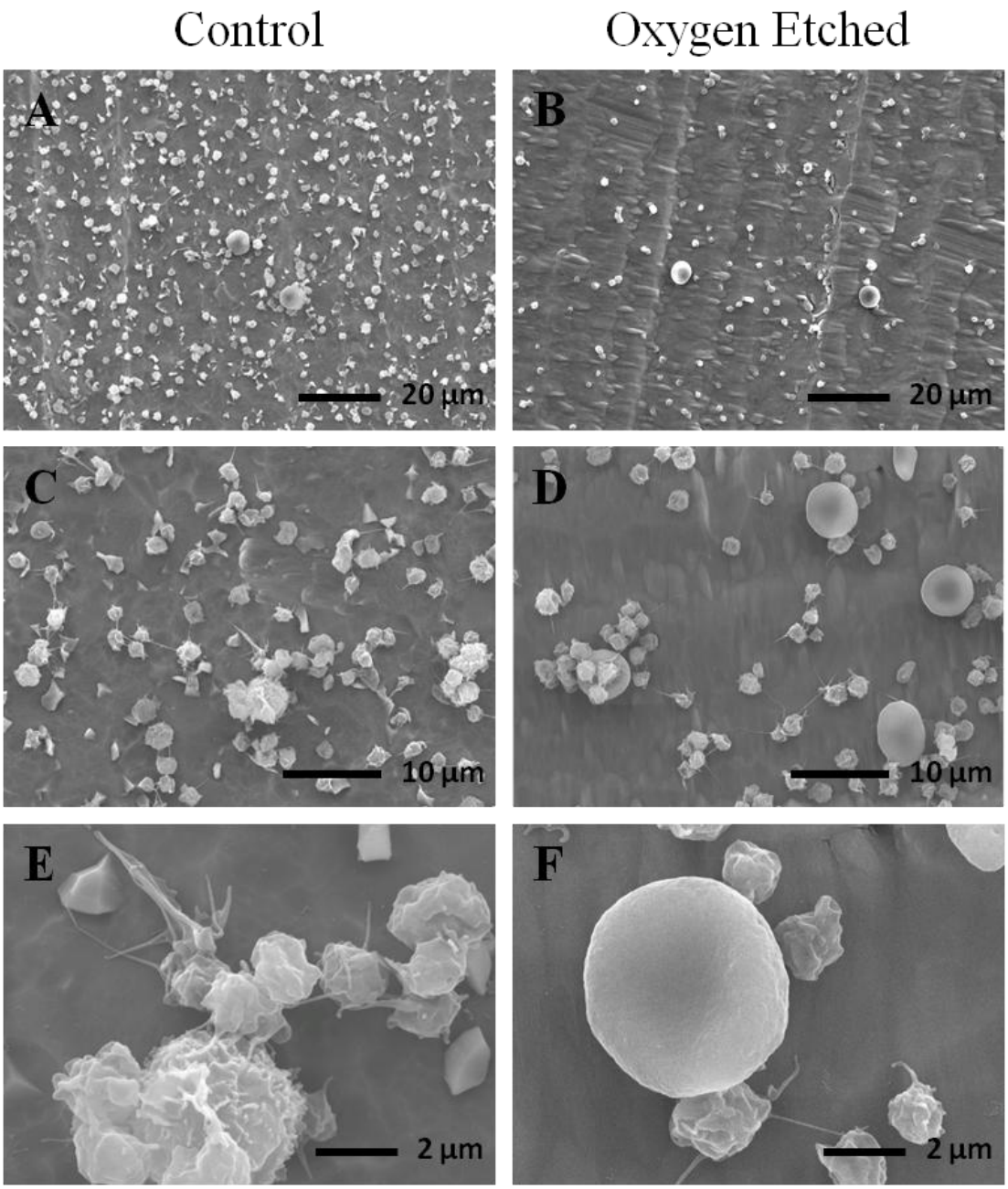

Figure 18 - Representative SEM images of adhered cells on the oxygen-etched titanium and control surfaces after 2 hours of incubation in whole blood plasma. The substrates were coated with a 10 nm layer of gold and imaged at 15 kV. Images show a lower degree of platelet activation, platelet-leukocyte interaction and cellular aggregation on oxygen-etched titanium.

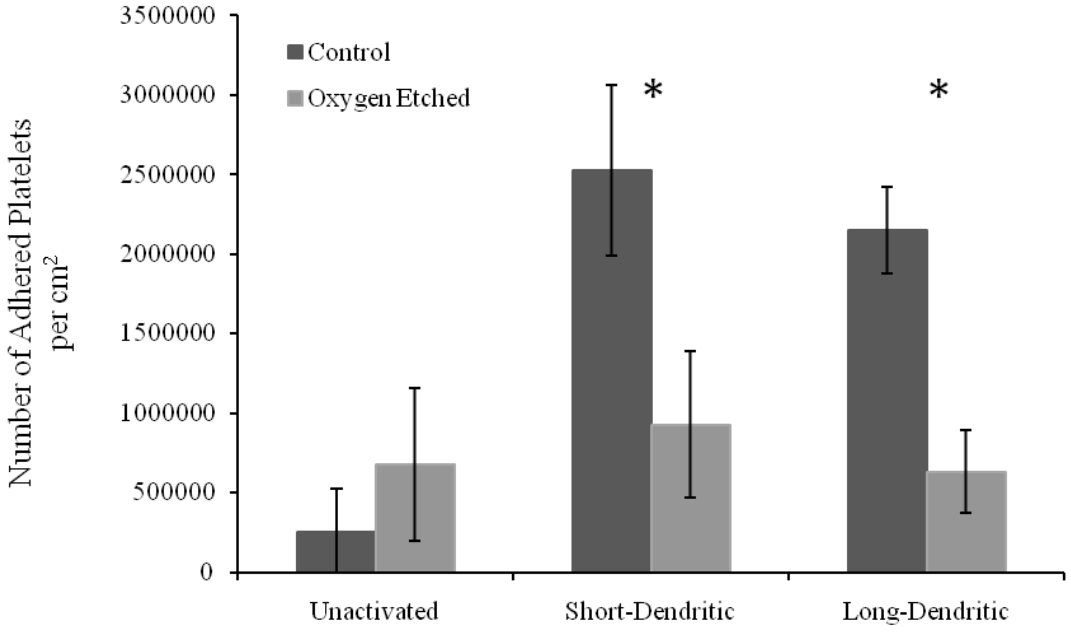

Figure 19 - Distribution of dendritic morphologies of adhered platelets on oxygen-etched titanium and control surfaces as a representation of platelet activation (* indicates statistical significance $p \leq 0.05$).

Surface-specific activation appears to be decreased on the oxygen etched titanium. Thus, the evolved oxide surface likely acts as a suppressant towards mature cellular activation and further aggregation. The opposite of these findings is readily apparent on the control substrates which clearly show increased platelet activation as indicated by the altered morphology and dendritic extensions on the control substrate. Further, control surfaces seem to promote regions of localized platelet-leukocyte adhesion and aggregation. Overall, these results identify a reduction in cellular adhesion and aggregation on oxygen etched titanium as compared to the control substrate, indicating a lower propensity for thrombogenic effects on oxygen etched titanium.

5.3.4 Whole Blood Clotting on Oxygen Etched Titanium Surfaces

The resistance of clot formation on the surface of implants is critical for the long-term success of blood-contacting biomaterials. These results show a higher amount of free hemoglobin for the oxygen etched titanium, indicating a lower degree of whole blood clotting on the oxygen etched titanium as compared to the control substrates (Fig. 20). Although no discrepancy in droplet coverage was noted at the time of testing, contact angle data indicated the control surface had a higher affinity for water. It is possible that blood coverage was influenced by this and the area of blood contact was slightly larger on the controls. However, the observed discrepancy between the control and oxygen etched surfaces remained higher than would be predicted for a corrected contact area. Oxygen etched substrates continued to show reduced clotting after 45 mins of exposure to whole human blood, while the control substrates exhibited nearly complete clotting after only 30 mins. These results indicate a reduced formation of the fibrin network, which corresponds to depleted clot strength, and subsequently, an increased clotting time on oxygen etched surfaces. This reduced clotting on the oxygen etched surfaces is likely attributed to either the reduction of defects in the oxide structure or the resulting lower surface energy. The clot-resistant properties of these surfaces would be useful in applications where clotting is detrimental to the long-term success of blood contacting devices.

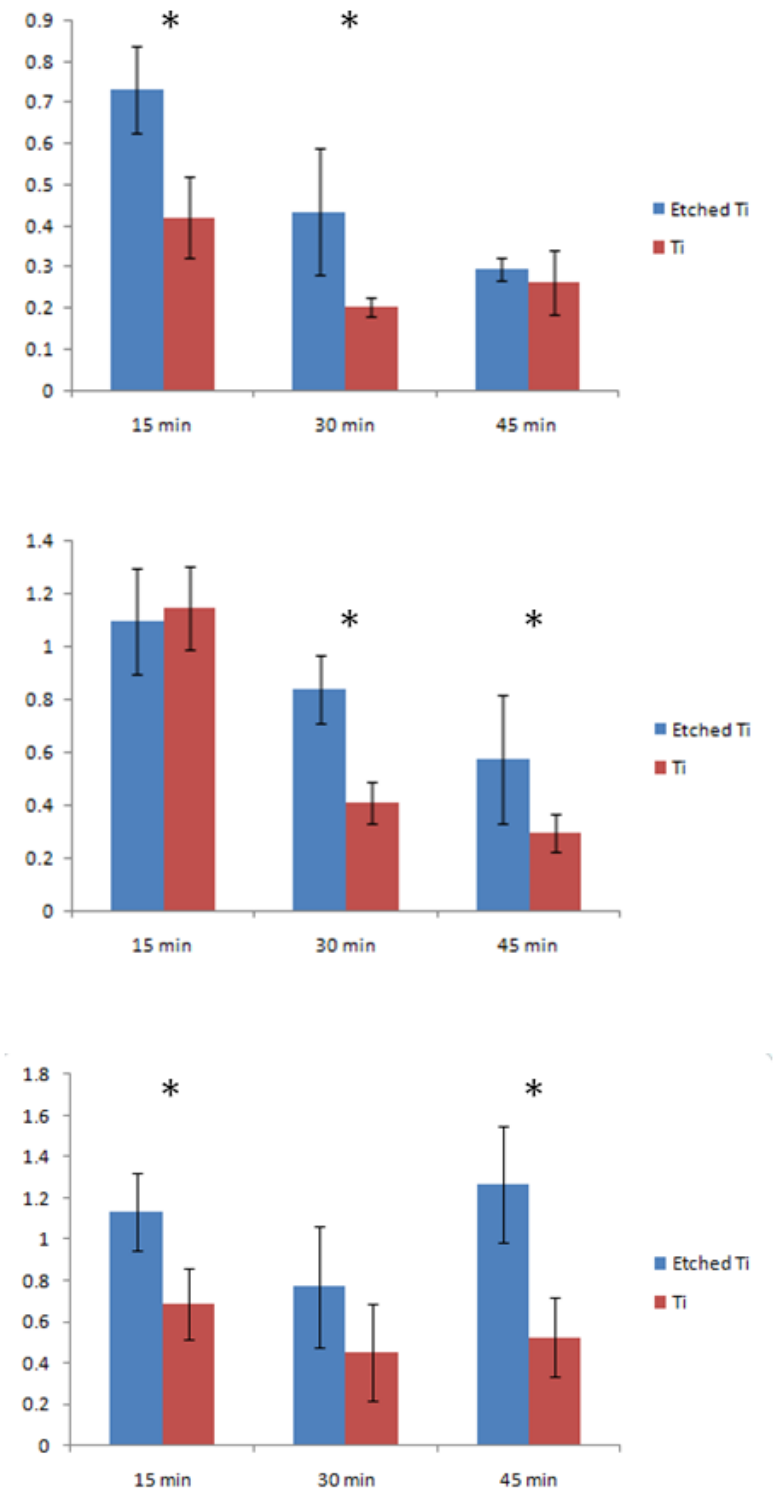

Figure 20 - Results of whole blood clotting kinetics for the three subjects tested. Free hemoglobin concentrations are shown in terms of absorbance on oxygen-etched titanium and control surfaces for up to 45 mins of clotting time (* indicates statistical significance $p \leq 0.05$).

5.3.5 Protein Adsorption on Oxygen Etched Titanium Surfaces

Within seconds to minutes after the biomaterial first comes into contact with blood or tissue, a complex cascade of events is initiated, beginning with protein adsorption [140-141]. This initial physiological reaction is critical in directing a further host response, which ranges from levels of biomaterial integration to complete material rejection and implant failure. It is therefore important to investigate the adsorption of key blood serum proteins (ALB, FIB and IgG) on oxygen etched titanium substrates as compared to the unaltered titanium alloy surfaces. In brief, all substrates were incubated in 100 μg/ml solutions of the aforementioned proteins for 2 hrs. The amount of the protein adhered to the surface of each substrate was determined by a commercially available BCA assay and XPS.

The adsorbed proteins were solubilized with an anionic detergent, SDS, and further quantified using a BCA assay. The results shown here indicate a slight increase in protein adsorption on oxygen etched titanium as compared to the control surfaces (Fig. 21). In addition, ALB adsorption was the lowest, followed by FIB and IgG, on both substrates.

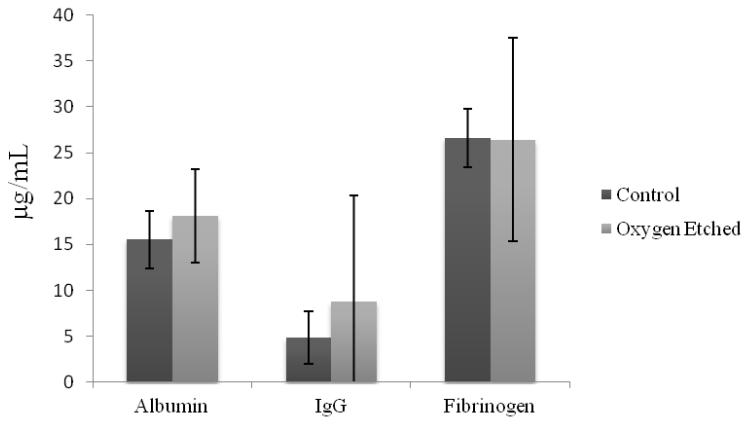

Figure 21 - Protein adsorption of key blood serum proteins (ALB, FIB, IgG) on oxygen-etched titanium and control surfaces determined using a BCA assay. Results show higher amounts of key blood serum proteins on oxygen-etched titanium (though not significant).

Protein adsorption on the test surfaces was further characterized using XPS, where survey and high resolution scans were used to determine the elemental surface composition and characteristic peaks. The XPS results confirmed those identified using the BCA assay, suggesting no significant difference in protein adsorption on the substrates. The presence of C-N and N-C=O peaks in the overall C1s peak is a more precise way to characterize protein adsorption. The C-N and N-C=O peaks are at a shift of 1.0 eV and 2.0 eV respectively from the C-C peak. Hence, high-resolution C1s scans were taken and a peak fit analysis was used to determine contribution of C-N and N-C=O peaks in the overall C1s peak (Fig. 22). These results indicate no significant increase in the intensity of C-N and N-C=O peaks for proteins adsorbed on oxygen etched titanium as compared to the control substrates. The lack of difference in protein adsorption is a possible indication that the depth of oxidation on the oxygen etched and control substrates is similar [142]. Protein adsorption may be optimized for specific applications by precisely tuning the depth of plasma penetration by varying the ion energy.

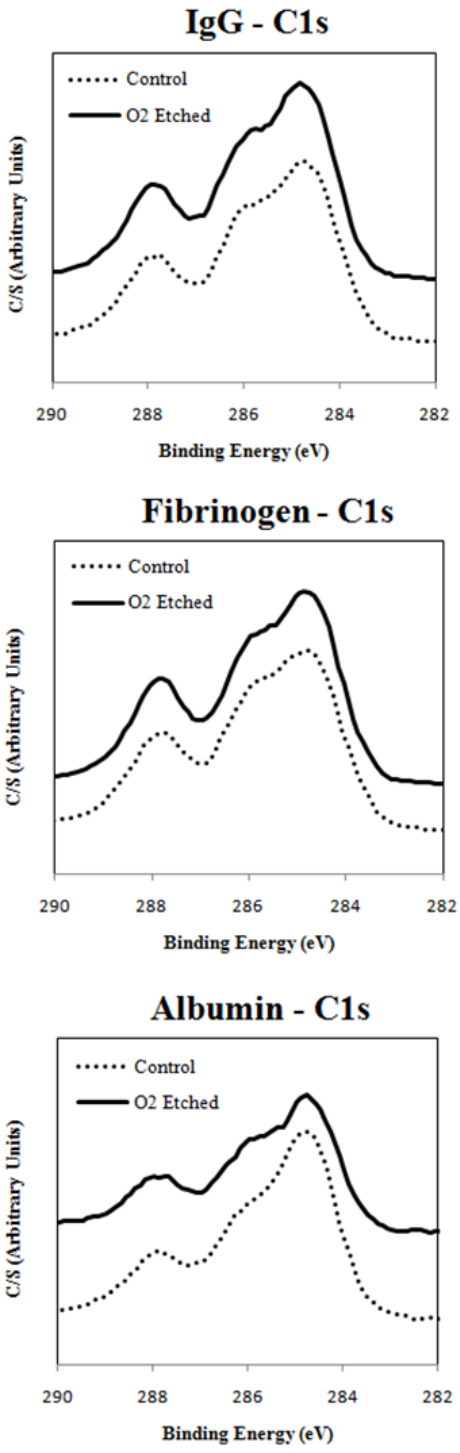

Figure 22 - Protein adsorption of key blood serum proteins (ALB, FIB, IgG) on oxygen-etched titanium and control surfaces determined using XPS. High resolution C1s scans for blood serum proteins adsorbed on oxygen-etched titanium and titanium (medical grade) surfaces showing C-N (285.8 eV) and N-C=O (286.8 eV) characteristic peaks for ALB, FIB and IgG.

5.4 Conclusion

In this work we have evaluated the thrombogenicity of oxygen etched titanium (Ti6Al4V), fabricated by oblique angle oxygen ion bombardment. Oxygen etching produces a higher quality oxide layer than those existing on native titanium surfaces. Our results show decreased platelet/leukocyte adhesion, activation and aggregation, greatly reduced clotting, and a slight increase in protein adsorption on oxygen etched titanium as compared to the control surfaces. Although the increased hydrophobicity of these surfaces would imply an increased clotting response, the results of this study indicate an overall reduction in propensity for thrombogenic effects on oxygen etched titanium. The improved blood reactions observed can likely be attributed to the natural inertness of the oxide as well as a reduction of defects in the oxide structure. Overall, this work provides a foundation for the use of these oxidized material surfaces in blood contacting devices. Further studies are now directed towards developing a method for characterizing and controlling the thickness of the oxide layer, and investigating the effects of varied oxygen etching techniques on thrombogenicity.

6 Ion Etching for Sharp Tip Features on Titanium and the Response of Cells to these Surfaces

(Specific Aim 3)

6.1 Introduction

The development of topographical features on the surface of biomaterials has been largely focused on increasing cellular attachment and subsequent cellular functionality on implants. However, in some cases (such as on stents, drug delivery implants, and transdermal devices) the function of the implant can be hindered due to uncontrolled cell proliferation on its surface. In these situations, it would be beneficial to engineer surfaces capable of resisting cellular adhesion, preventing cells from aggregating on areas that need to remain unobstructed.

Directed ion beam etching has been demonstrated to produce ordered surface features on a number of materials; a few of the more common features observed are dots [1, 3], holes [2], ripples [3, 143], and pyramidal structures [116, 144]. Applications of these ion etched surfaces have seen limited use in the fields of biomedicine, though their potential has been recognized as early as the mid 1980s [145]. Feature formation on biomaterials due to oblique angle argon etching has been previously investigated on aluminum [144] as well as titanium, tantalum, alumina, and stainless steel [133]. These efforts documented the formation of needle-like features on the aluminum, alumina and tantalum, as well as a scale-like topography on the titanium and stainless steel. This work demonstrates the ability of oblique angle ion etching to form a surface of uniform, randomly distributed sharp tipped features on a titanium substrate and evaluates the bio-response of these surfaces for the first time.

Sharp tipped [146] or complexly structured [147-148] nanotopographies have already shown the ability to impact cell conformation and adhesion. The features created here by oblique angle ion etching are similar in form and size to some of those previously tested formed using other methods. This work uses a culture of immortalized osteoblasts (hFOB 1.19) to assess the response of living cells to the needle-like features formed by the oblique etching to determine if these surfaces could also regulate cellular attachment in a similar fashion.

6.2 Experimental

Substrates of titanium alloy Ti6Al4V were machined into 1 cm x 1 cm squares and ultrasonically cleaned with Simple Green®, water, and finally acetone. Stainless steel etching fixtures allowed substrates to be placed under the ion beam and held for ion incidences approximately 30° and 75° from surface normal. Substrates were held at a distance of 4 – 9 cm from the source grids (feature formation appeared to have no dependence on the etching distance for the values used). An 8 cm ion source was used to create a beam of 1200 eV argon ions with a beam current of 100 mA. Processing used a 4 sccm argon flow, and the chamber pressure during etching remained constant at 2.0×10^{-5} Torr. The substrates were etched for 3 hours to ensure steady state feature formation.

The etched and control substrates were evaluated using a scanning electron microscope (SEM, JEOL JSM-6500F). Surface imaging was performed with 15 keV electrons at a working distance of 10 mm. Bare substrates were imaged without a gold coating. Surfaces were also characterized using a Zygo: NewView™ 7300 white light interferometer. The interferometer was equipped with a 100x Mirau objective and 2x optical zoom using a working distance of 0.8 mm. Data were collected and analyzed using the Zygo: MetroPro™ computer software.

A week-long study was performed using an immortalized lineage of human fetal osteoblasts (hFOB 1.19) to assess the reaction of cells to the sharp tipped topographies. Each substrate was seeded with approximately 10,000 cells in 1 mL of media (1:1 mixture of Ham's F12 Medium and Dulbecco's Modified Eagles Medium w/ 2.5 mM L-glutamine [w/o phenol red]; 0.3 mg/ml G418; 10% final concentration of fetal bovine serum). Substrates were incubated at 33.5 °C in a humidified, 5% CO_2, sterile environment for 4 days to allow adhered cells to proliferate on the test surfaces. At the end of the Day 4, the incubation temperature was increased to 39 °C to allow the cells to differentiate into mature osteoblasts.

Cellular activity was assessed on Day 1, Day 4, and Day 5 (Day 1 post differentiation) by a MTT (3-[4,5-dimethylthiazol-2-yl]- 2,5-diphenyl tetrazolium bromide) assay (Sigma, CGD-1). This colorimetric assay measures mitochondrial activity and is used to gauge the health and viability of cells.

Cell adhesion and spatial organization was characterized by staining surface-adherent cells with calcein AM (Invitrogen) live stain on Day 1, Day 4, Day 5, and Day 7. Prior to staining, unadhered cells were removed by gently rinsing the surfaces with PBS. A 3 μM calcein-AM solution in PBS was then added to each substrate before imaging with a fluorescence microscope (Carl Zeiss). Complete protocols for the aforementioned evaluations have been described in a previous publication [143].

6.3 Results and discussion

The oblique angle ion etching resulted in surfaces dominated by randomly distributed, needle-like features (Fig. 23). Although the physical appearance of these protrusions differed with processing angle, the tips of the formations were consistently oriented back towards the

direction of ion origin. It is predicted that the angle of the needle formations is complimentary to the angle of ion incidence, but this has yet to be confirmed. Surface temperature, ion energy, and ion flux all likely play critical roles in determining the evolution of the topography; this is indicated by the disparity in the needle formation seen in this work compared to the scale-like formations previously reported on titanium [133].

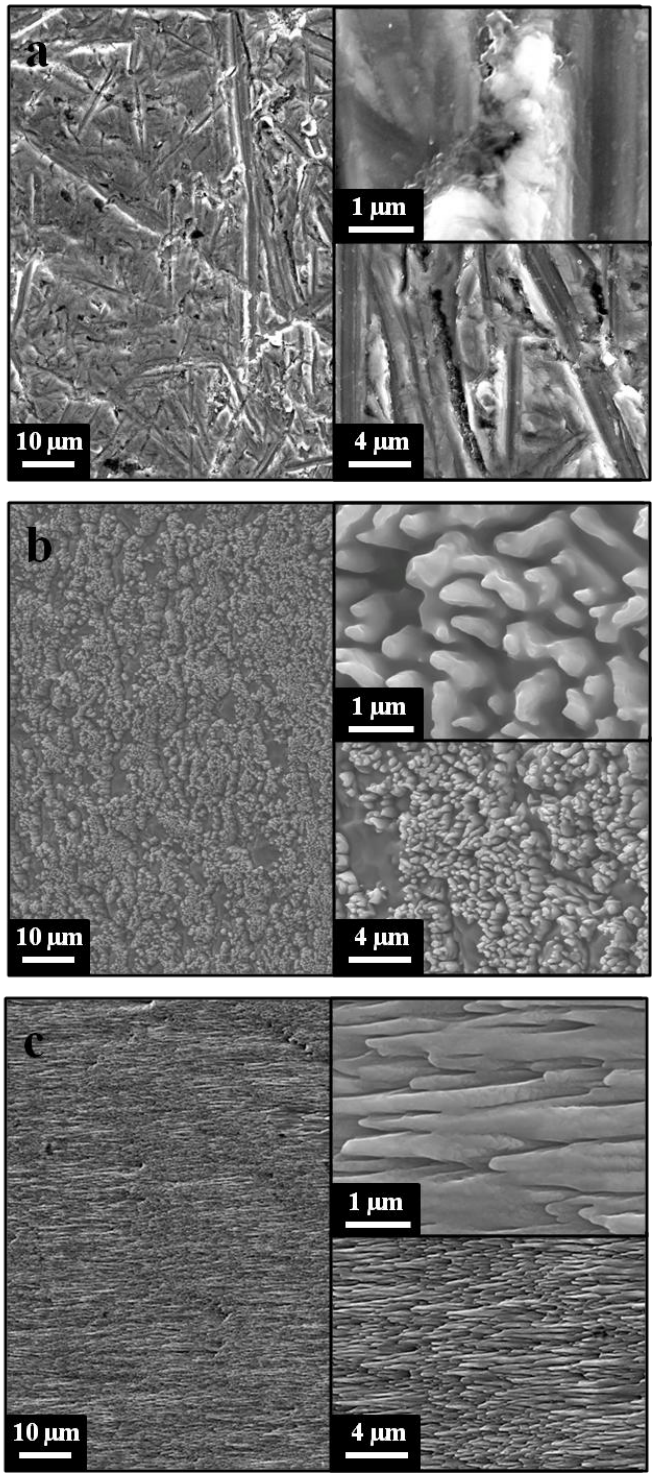

Figure 23 - SEM images showing the titanium surfaces: a) control, b) 30° etch, and c) 75° etch. Needle-like formations were observed on both the etched surfaces with needles oriented toward the impacting ion direction of origin.

Examination of the etched surfaces with the white light interferometer revealed dramatic changes in surface structure (Fig. 24). Although the roughness of the 75° etch remained comparable to the pre-treated state, the roughness of the 30° etch was nearly four times that of the control surface. The needle height above the surface varied, but most points on the 30° etch appeared to extend at least 1 µm from the base. Needles on the 75° etch remained closer to the surface, rarely appearing above 0.5 µm. The unique feature of the 75° etch was that the needles aligned to form ordered grooves across the material; a patterning not observed on the 30° etch.

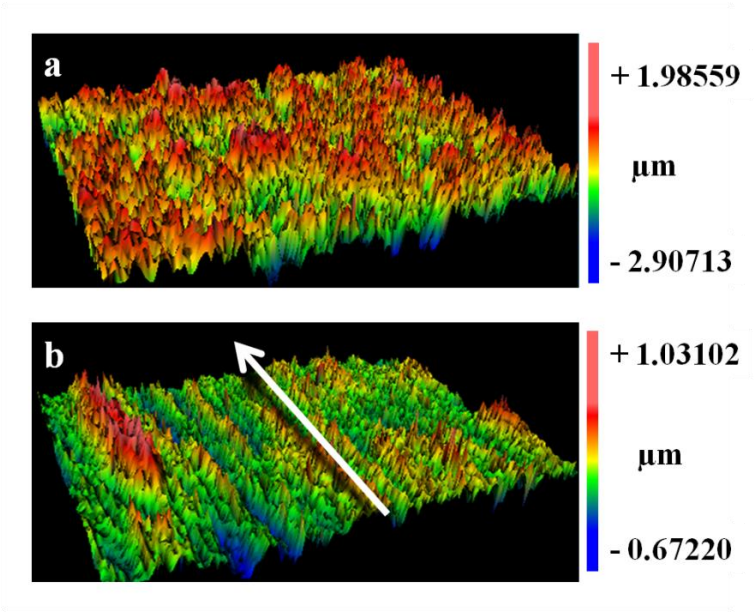

Figure 24 - Scanning white light interferometry revealed the coarse topographies produced by the oblique angle ion etching (a) 30° etch, b) 75° etch; imaged area is 70 µm x 50 µm). A secondary patterning was also revealed on the 75° etched surface; micron sized groves were formed across the surface (b). The length of the grooves run parallel to the direction indicated by the arrow.

The differences in surface topography dramatically affected the conformation of osteoblasts. Figure 25 displays the representative images from the calcein AM staining on Day 5 of the study. At all time points, cells on the control surfaces displayed typical spread morphologies indicative of good adhesion to the titanium. Conversely, cells adhered to surfaces etched at 30° remained rounded with few extensions through the course of the study. Cells on the 75° etched surfaces

also behaved uniquely, showing a preferential elongation following the length of the grooves formed in the surface. These results show agreement with previous observations on similar sharp-tipped and grooved topographies [146].

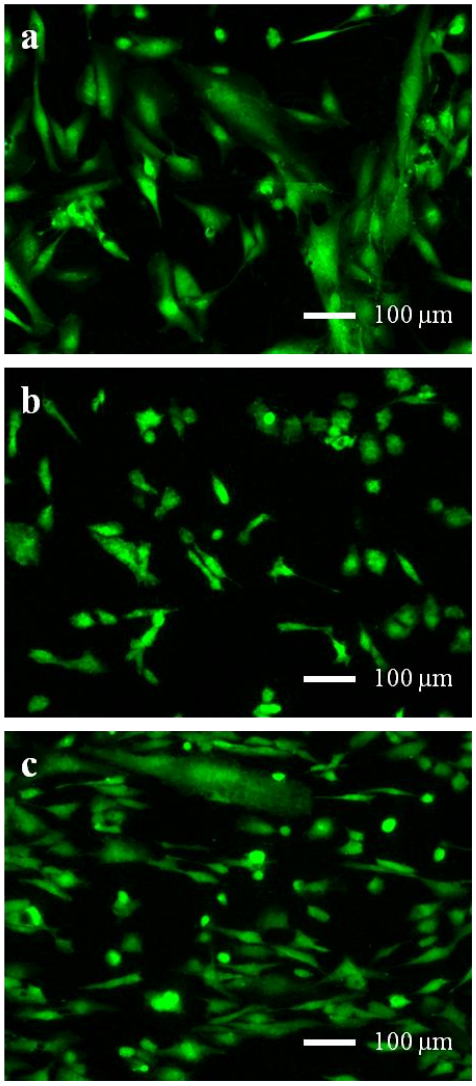

Figure 25 - Calcein AM staining of the hFOBs revealed the influence of these surfaces (a) control, b) 30° etch, and c) 75° etch) on cell morphology. Cells on the control surface (a) displayed a typical spread cell conformation, while those on the 30° etched surface (b) remained mostly rounded. The cells on the 75° etch also displayed a unique reaction to the topography, preferentially elongating with the orientation of the needles (and surface grooves).

Although cell morphologies were greatly influenced by the oblique angle ion etched surfaces, the overall number of adhered cells appeared unaffected. MTT assays showed no significant difference in mitochondrial activity on the surfaces at any time point. This would suggest that cell quantities and health were similar on all conditions. Although the 30° etched topography limited cell extensions, the sharp tips were un-able to reduce the number of cells adhering. It is still possible however, that in a dynamic environment (such as what a stent would experience when exposed to blood flow) cell adhesion would be significantly reduced by the prevention of cell spreading and the 30° etched surface could shed the rounded cells.

6.4 Conclusions

Oblique angle ion etching at 30° and 75° was used create uniform networks of randomly distributed, needle-like structures across the surface of Ti6Al4V. The 30° etching resulted in a sharp-tipped topography, while the needles on the 75° etched surface laid closer to the surface but arranged to create linear grooves in the material. The sharp tips of the 30° etch prevented cells from spreading on the surface, but failed to limit the number of adherent cells. Cells on the 75° etched surface showed preferential elongation along the length of the grooves formed by the needles. Although surfaces similar in nature to those produced in this work have been previously demonstrated, oblique angle ion etching provides a novel method for obtaining these structured surfaces on titanium (and could possibly be extended to other metallic substrates as well). This technique would be particularly useful in applications where traditional fabrication methods such as lithography are prohibited.

7 Low Energy Helium Ion Texturization of Titanium and Relevance to Biomedical Applications

(Specific Aim 4)

7.1 Introduction

Helium irradiation of metals has long been studied in efforts to understand the damaging aspects associated with applications in fusion reactors and tritium storage. Recent studies on tungsten have shown that at elevated temperatures, a high flux, low energy (< 500 eV) helium bombardment can result in extreme modifications and the development of complex surface topographies [60, 75-82]. This is a departure from the traditional methods of exposure that previously relied on high implantation energies (> 20 keV) or the tritium trick to introduce the helium into substrates. The unique trends observed during low energy helium bombardment of tungsten suggest that helium surface texturization may be precisely controlled to engineer surfaces. The porous and complex nature of topographies created during fusion research resemble the micro- and nano- architectures seen in natural bone, and may therefore provide an additional method to enhance osseointegration.

If controlled micro- and nano- porous titanium surfaces could be created, there are a number of potential applications in the field of biomedicine. It is possible that texturized surfaces could increase osseointegration, reducing healing times after surgeries and extending the functional lifetimes of treated hard tissue implants (pedicle screws, dental implants, total joint replacements, etc.).

The effects of high energy (>6 keV) helium ion exposure on titanium have been well documented [149-155]. Under these conditions, the resulting helium bubble formation typically results in the evolution of a nano- porous material. However, the immediate surface of implanted substrates must often be etched or polished away to access the more porous regions due to the increased depth of implantation [155].

This work examines the use of high flux, low energy helium ion exposure of titanium to create porous topographies on the immediate surface, eliminating the need for additional processing. The effect of such surfaces on the viability of living cells is also assessed.

7.2 Materials and Methods

Substrates (1 cm x 1 cm) were water-jetted from 0.127 cm thick medical grade Ti6Al4V-ELI titanium alloy sheets (Online Metal Supply). An ultrasonic cleaner was used to remove contaminants from the substrates; the cleaning consisted of 15 minutes in baths of Simple Green® solution, water, and finally acetone.

7.2.1 Fabrication of Texturized Surfaces by Helium Ions

To perform the helium processing, a custom plasma reactor (modeled after a hollow cathode) was designed and constructed. This reactor consisted of a negatively biased, hollow tantalum cylinder approximately 1.5 cm in diameter with a length of 8.2 cm to act as the cathode, while a grounded stainless steel plate (4 cm x 4 cm) served as the anode. The cathode was placed inside an alumina tube (~2.5 cm inner diameter) to electrically shield the cathode from the walls of the vacuum chamber, limiting unnecessary coupling and isolating the plasma to the reactor interior. Radiation shielding was also wrapped around the outside of the alumina tube to thermally

insulate the interior of the reactor. A schematic illustrating the reactor assembly is given in Fig. 26.

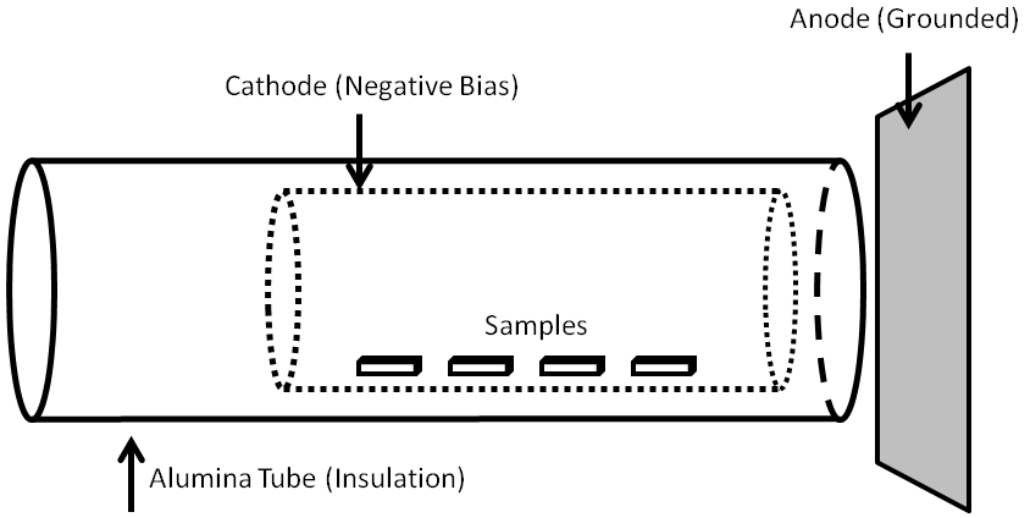

Figure 26 - This illustration demonstrates the configuration of the plasma reactor used to process the substrates. Samples were placed directly onto the inner surface of the cathode tube, and were not independently biased.

An Edwards E2M30 mechanical pump was used to evacuate the vacuum chamber to a baseline of nearly 20 mTorr. During processing, the mechanical pump was left running and the chamber was continuously backfilled with helium to a pressure of approximately 2 Torr. A MDX Magnetron power supply (Advanced Energy) was used to bias the cathode and drive the plasma discharge.

Two conditions were used to process substrates; a 0.5 A discharge and a 1.0 A discharge. In both of these states, under normal operation, discharge voltages ranged between 280 – 320 V. The substrates were processed 3 - 4 at a time for durations of 15 minutes. A Langmuir probe was used to characterize the plasma in the reactor near the substrate locations. During the 0.5 A condition, an electron density of $n_e \sim 2 \times 10^{17}$ m^{-3} and temperature, $T_e \sim 4$ eV were typical. For

the 1.0 A condition, both electron density and temperature increased to $n_e \sim 3 \times 10^{17}$ m^{-3} and $T_e \sim$ 6 eV respectively. Under the neutral density and plasma property conditions present in the tests, the sheath above the substrate surface was collisionless and the energy of the ions impacting the substrates could be estimated from the bias of the cathode, $E_{ions} \approx V_{cathode} - 2T_e$. For the conditions used in the creation of the etched substrates, the energy of the incident ions was ~ 300 eV.

Temperature in the reactor was monitored by submersing a thermocouple (potted in a ceramic compound inside an alumina tube) in the plasma environment during operation. A small band of stainless steel sheet metal was also placed over the thermocouple, allowing the probe to be exposed to a plasma environment that closely simulated the exposure conditions of the substrates.

The helium etched and control substrates were evaluated using a scanning electron microscope (SEM, JEOL JSM-6500F). Surface imaging was performed without gold coating with 15 keV electrons at a working distance of 10 mm.

Substrates were also characterized using a Zygo: NewView™ 7300 scanning white light interferometer (SWLI) with a 100x Mirau objective and 2x optical zoom at a working distance of 0.8 mm. These settings resulted in a scan resolution of approximately 50 nm. Processing consisted of a 4 x 4 stitching of 40 μm bipolar downward scans with plane removal for height balancing as well as a low pass filter to remove unwanted noise. Data was collected and analyzed using the Zygo: MetroPro™ computer software.

7.2.2 Culture of hFOB 1.19 Cells on Helium Etched Surfaces

A week-long study was performed using an immortalized cell line of human fetal osteoblasts (hFOB 1.19) to assess the suitability of helium etched titanium in orthopedic applications. This cell line exhibits rapid cell division at lower temperatures (33.5 °C), while at higher temperatures (39 °C) cell division is slowed and the cells have the ability to differentiate into a mature osteoblastic phenotype. Cells were expanded in culture flasks with maintenance media (1:1 mixture of Ham's F12 Medium and Dulbecco's Modified Eagles Medium w/ 2.5 mM L-glutamine [w/o phenol red]; 0.3 mg/ml G418; 10% final concentration of fetal bovine serum) for approximately 3 weeks to increase cell density before seeding. During expansion, cells were incubated at 33.5 °C in a humidified 5% CO_2 sterile environment.

Helium etched substrates (from both the 0.5 A and 1.0 A processing conditions) and the as-received titanium controls were placed into 24-well culture plates. Substrates were placed in a 70% ethanol bath and simultaneously sterilized by a 30 minute exposure to ultraviolet light. After sterilization, the ethanol was aspirated and substrates were rinsed twice in phosphate buffer solution (PBS). To condition the surfaces for seeding, substrates were allowed to incubate several days in acellular media. Once the conditioning media was aspirated, each substrate was seeded with approximately 10,000 cells in 1 mL of media. Substrates were incubated at 33.5 °C for 4 days to allow adhered cells to proliferate on the test surfaces. At the end of Day 4, the incubation temperature was increased to 39 °C to allow the cells to differentiate into mature osteoblasts.

Cellular activity was assessed on Day 1, Day 4, and Day 5 (Day 1 post differentiation) by a MTT (3-[4,5-dimethylthiazol-2-yl]- 2,5-diphenyl tetrazolium bromide) assay (Sigma, CGD-1). This colorimetric assay measures mitochondrial activity and is used to gauge the health and

viability of cells. Substrates were placed in new 24-well plates and 0.5 mL of a 10% concentration of MTT Solution in fresh media was added to each well. Substrates were incubated for 3 hours at the previously defined temperatures. After incubation, 0.5 mL of MTT Solvent was added to each well and the plates were gently shaken for 10 minutes to facilitate formazan crystal dissolution. Solutions from each of the substrates were titrated and 200 μL were placed into the wells of a 96-well plate. Absorbance was measured at a wavelength of 570 nm with a FLUOstar Omega (BMG Labtech) spectrophotometer; background absorbance at 690 nm was subtracted from these readings.

Cell adhesion and spatial organization were characterized by staining surface-adherent cells with calcein AM (Invitrogen) live stain on Day 1, Day 4, Day 5, and Day 7. Prior to staining, unadhered cells were removed by gently rinsing the surfaces with PBS. A 3 μM calcein AM solution in PBS was then added to each substrate before imaging with a fluorescence microscope (Carl Zeiss).

At all evaluation time points, SEM imaging was used to visualize cell morphology on the helium etched and control substrates. Prior to SEM imaging, un-adhered cells were removed by gently rinsing the substrates twice with PBS. The remaining cells adhered to the substrate surfaces were fixed, dehydrated and coated with a 5 nm layer of gold prior to imaging using protocols previously described [143].

7.3 Results and Discussion

7.3.1 Surface SEM Characterization

The helium ion bombardment resulted in dramatic changes to the surface topography of the titanium substrates (Fig. 27). In both the 0.5 A and 1.0 A exposures, substrates formed a network

of randomly distributed pores. These features were not localized to any specific area, but were uniformly distributed over the substrate surface. Hole size and density varied between the two preparations; the voids on the 0.5 A substrates averaged a sub-micron diameter but were much greater in number while those on the 1.0 A substrates were fewer but several microns in diameter.

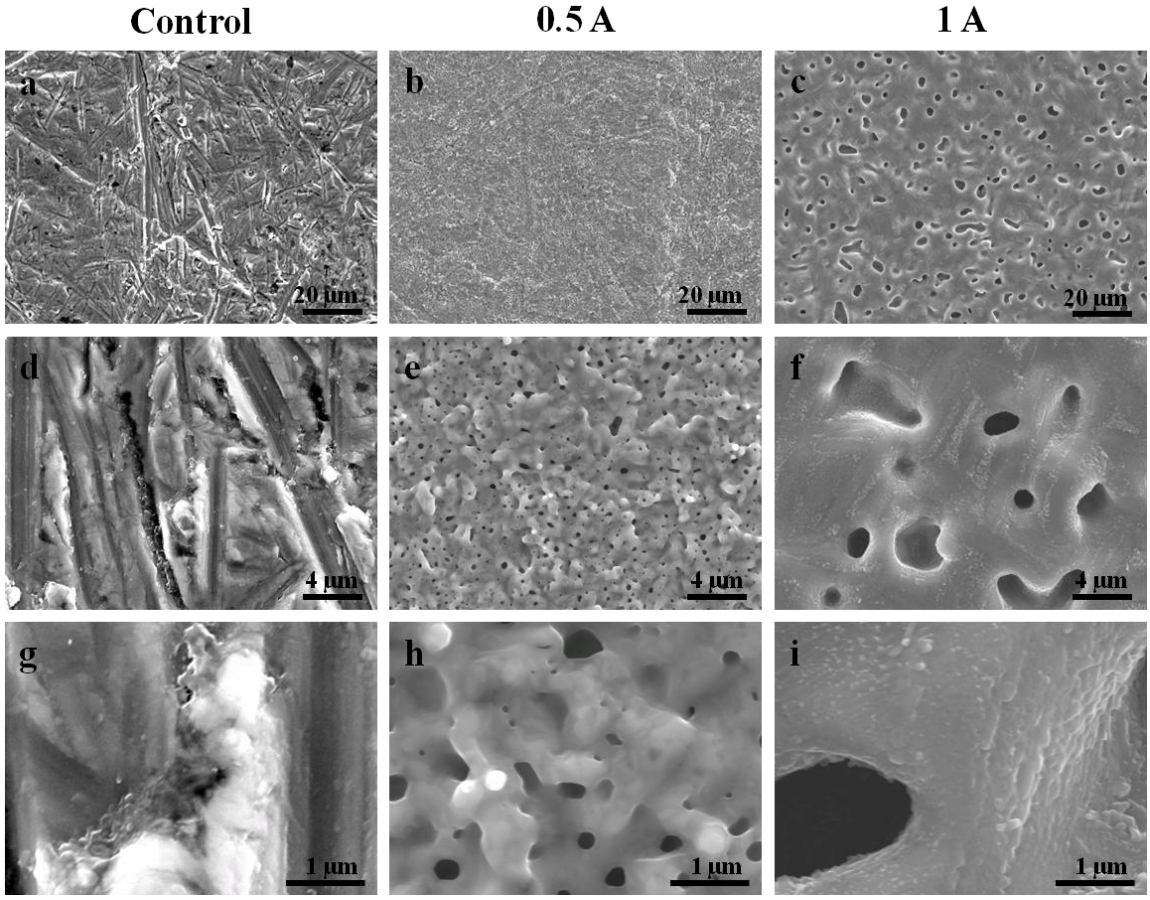

Figure 27 - SEM images showing the effects of the helium bombardment at different magnifications (a-c: x1,000; d-f: x5,000; g-i: x20,000).

The sputter yield for titanium under 300 eV helium irradiation is very low, measured at just 0.05 atoms per ion [156]. The physical removal of material from the surface therefore plays a minimal role in evolution of these features. This was confirmed by mass measurements (with a resolution of 20 μg) taken before and after plasma exposure that indicated no material was lost (data not shown).

It is common for helium irradiation to produce bubbles or voids on or beneath the surface of a material. Although interstitial helium diffuses rapidly through metals due to its low solubility, helium is readily trapped by lattice vacancies or other defects and may remain stable at these positions. In addition, high concentrations of interstitial helium is capable of forming Frenkel defects in a perfect crystal lattice structure to induce self-trapping [66]. These events allow the creation of defects throughout the irradiated near surface so bubble nucleation is not limited to the previously existing defects of the material. It is possible that self-trapping is the dominant mechanism for bubble nucleation under the tested conditions, explaining why hole formation across the irradiated surfaces appears uniform and random instead of being localized to highly defective regions such as grain boundaries.

Once helium clusters have formed, there appears to be no saturation limit to restrict expansion. Three mechanisms of bubble growth have been previously outlined: vacancy collection, Ostwald ripening, and bubble migration and coalescence [72]. In vacancy collection, bubbles can grow by assimilating thermal or damage vacancies or, build enough pressure to deform the surrounding atomic lattice and use a loop punching method to create additional vacancies. Ostwald ripening relies on the dissolution of helium from smaller bubbles, diffusing through the material, and resorbing into larger bubbles. Under the bubble migration and

coalescence mechanisms, bubbles migrate randomly through Brownian motion and collide to form larger voids.

The hole patterning observed on the substrates suggest that growth was dominated by bubble migration and vacancy collection. If Ostwald ripening events were occurring, a variation in void sizes would be evident (ranging from a collection of larger, growing bubbles to smaller, shrinking bubbles). Although there was a disparity in bubble sizes on the 0.5 A substrates, the 1.0 A treatments (with temperatures that would be more permissive to the ripening mechanism) appeared to have no voids less than ~ 1 μm in diameter. This lack of smaller voids not only implies a lack of Ostwald ripening but also suggests an impaired ability for new bubble nucleation or the growth of newer nucleation sites.

Since processing variables such as ion energy and background pressure remained consistent under both treatment conditions, the observed variation in the hole sizes is likely due to a) the difference in ion flux, b) the difference in total ion fluence, or c) the difference in substrate temperatures experienced at each condition. Flux values were computed by dividing measured discharge current of the power supply by the cathode surface area. The 0.5 A condition resulted in a flux of ~ 8.1 x 10^{16} m^{-2} s^{-1} and a total fluence of ~ 7.3 x 10^{19} m^{-2} while the 1.0 A conditions doubled these values (these approximations do not correct for secondary electron emission). During processing, all substrates started at room temperature and were heated only by exposure to the reactor plasma. Substrates processed at 0.5 A were heated to a final temperature of approximately 450 °C, while those processed at 1.0 A were heated to just over 600 °C. Heating was rapid, with the substrates temperatures rising to within 50 °C of their maximum in less than 5 minutes.

If hole formation and the expansion of bubbles were driven solely by the flux or total fluence, one of two outcomes would have occurred: the 1.0 A substrates would have twice the number of holes as the 0.5 A substrates, or there would be roughly the same number of holes but the diameters would be slightly larger to accommodate the increase in helium. Instead, fewer but much larger pores were observed on the 1.0 A substrates indicating a clear increase in bubble mobility and coalescence; factors heavily influenced by temperature but to which changes in flux and fluence are largely inconsequential. It can therefore be concluded that substrate temperature is the most important factor in determining the size and number of pores. This is supported by the nearly identical surfaces noted on tungsten under comparable helium irradiation conditions where pore size was also found to be directly related to the processing temperature [53].

7.3.2 Surface SWLI Characterization

The helium etched substrates were also characterized using scanning white light interferometry to evaluate changes in surface roughness. The scanned area on each substrate was 0.11 mm x 0.08 mm. Table 3 shows the roughness values as calculated by the Zygo: MetroPro™ computer software. Exposure to helium bombardment shows an apparent increase in surface roughness in addition to the development of porosity. A small increase in overall surface roughness was observed on the 0.5 A substrates as compared to the control surfaces. This was largely due to the fact that pore formation occurs on the pre-existing substrate surface and the overall structure was not dramatically affected by the ion bombardment. Scratches and flaws that existed on the surfaces before processing were still distinguishable after the treatment. However, substrates processed at the 1.0 A etched condition had a significantly higher

roughness; nearly double the values of the control and 0.5 A condition. In addition, the 1.0 A surfaces were completely restructured, showing no evidence of prior surface blemishes. Representative images from the scans are shown in Fig. 28.

Table 3 - Several surface roughness parameters were computed for the substrates: SRa – average feature heights, SRz – average maximum feature heights, and SRq – root mean square of feature heights.

	SRa (µm)	SRz (µm)	SRq (µm)	Number of substrates evaluated
Control	0.171 ± 0.019	1.119 ± 0.038	0.231 ± 0.019	2
0.5 A	0.205 ± 0.017	1.509 ± 0.441	0.282 ±0.026	4
1.0 A	0.387 ± 0.063	2.807 ± 0.964	0.508 ± 0.089	3

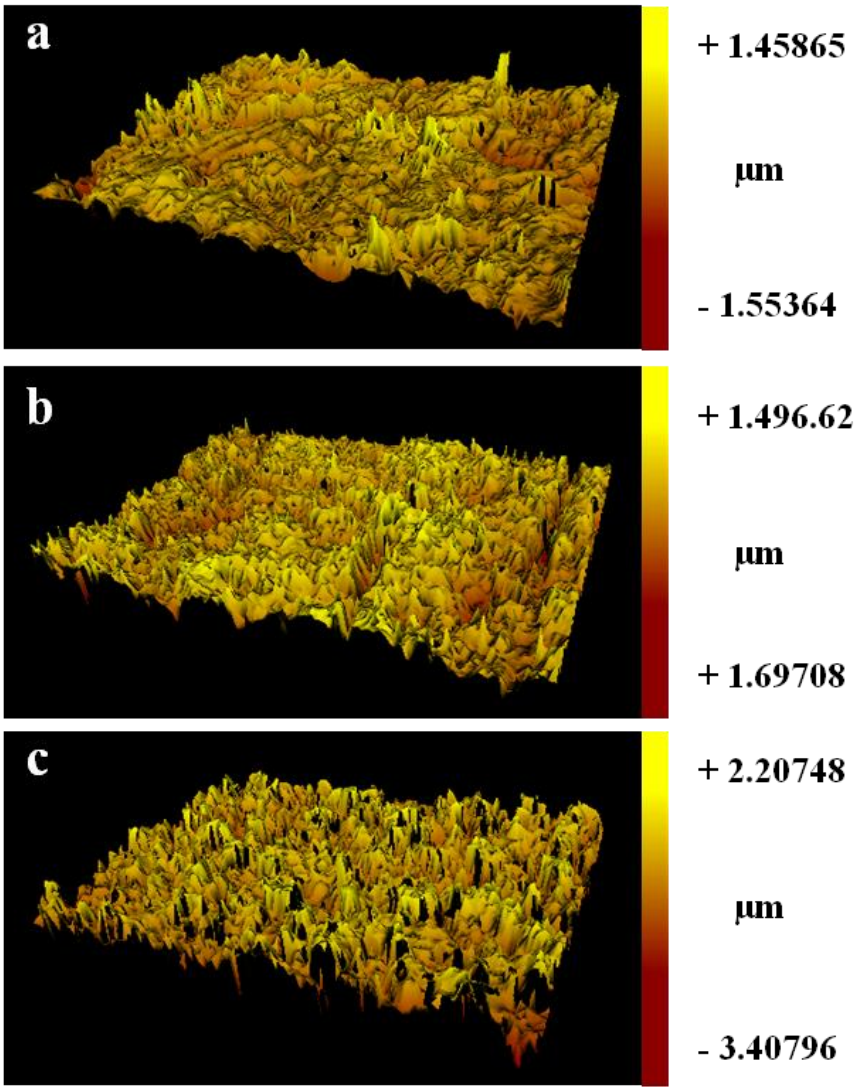

Figure 28 - White light interferometer scans show the topographies of samples from the a) control, b) 0.5 A condition, and c) 1.0 A condition. The black areas across the surface of image c) are a result of data dropout due to the deep pores in the material.

7.3.3 hFOB Cell Culture

A culture of cells from the immortalized hFOB 1.19 lineage was used to assess the potential compatibility of these surfaces with osteoblasts. Celled substrates were cultured at a proliferation permissive temperature of 33.5 °C for 4 days before the temperature was raised to 39 °C for an additional 3 days to allow the cells to express a mature osteoblastic phenotype.

Calcein AM staining was used to assess cell adhesion and spatial organization on Days 1, 4 and 5 (Day 5 is one day after the temperature was raised to 39 °C). Representative images from the staining are shown in Fig. 29. The live stain revealed no significant differences in cell quantity or spacing between either of the helium etched substrates and the control.

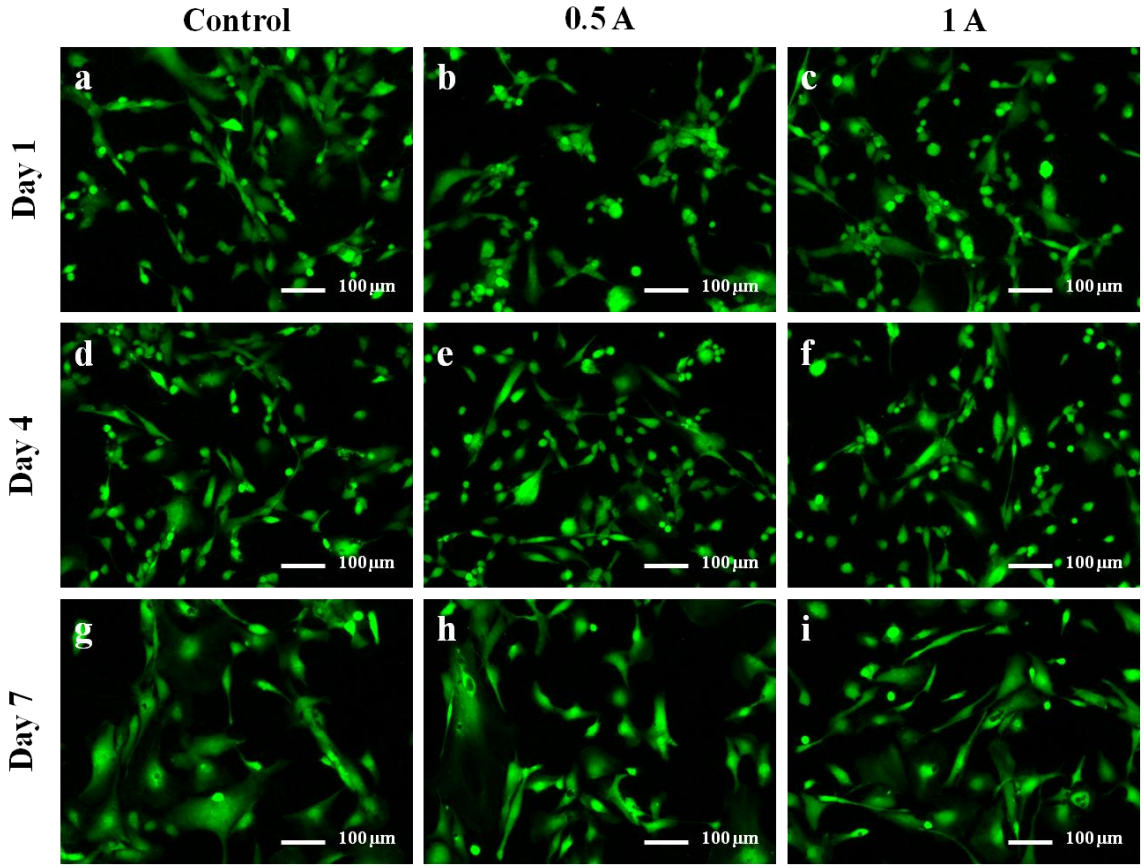

Figure 29 - These representative images taken after calcein AM staining. No notable variations in cell conformations or densities between the tested surfaces were observed over the course of the study.

Cell viability was also assessed on Days 1, 4, and 5 by measuring mitochondrial activity with a MTT assay. Figure 30 shows the absorbance values obtained by the colorimetric assay. Absorbance values from the helium etched substrates were significantly ($p > 0.05$) lower than the

control substrate. This indicates the helium substrates either had lower densities of adhered cells or the cells on the etched surfaces were less active. The steady increase in absorbance values between each evaluation time point shows cells were healthy and viable on all substrates. Although the helium treated substrates initially had lower absorbance values, by Day 5 these values were comparable to the control (with the 1.0 A substrates eventually surpassing the control). This could indicate that initial cell adhesion is decreased by the helium texturization, but once cells are established on the surface cellular activity is increased.

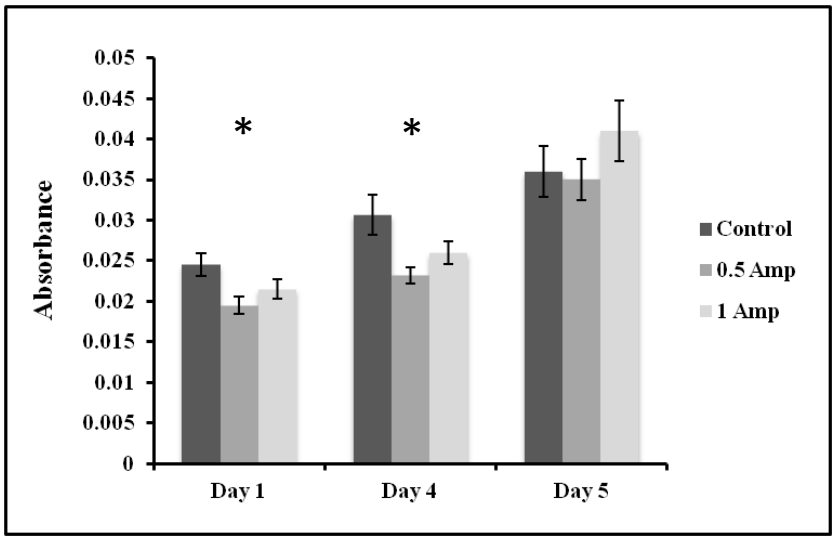

Figure 30 - Absorbance values from the MTT assay indicating cell viability. On Day 1 and Day 4, both helium etched substrates had absorbance values significantly lower than the control substrate.

Findings of the SEM analysis were similar to the results observed in the Calcein AM staining. The imaged substrates displayed comparable cell behavior at each time point evaluated over the course of the study. Cell morphology was unaffected by the variance in both surface topography and roughness. Figure 31 displays representative cell images from the Day 7 evaluation point.

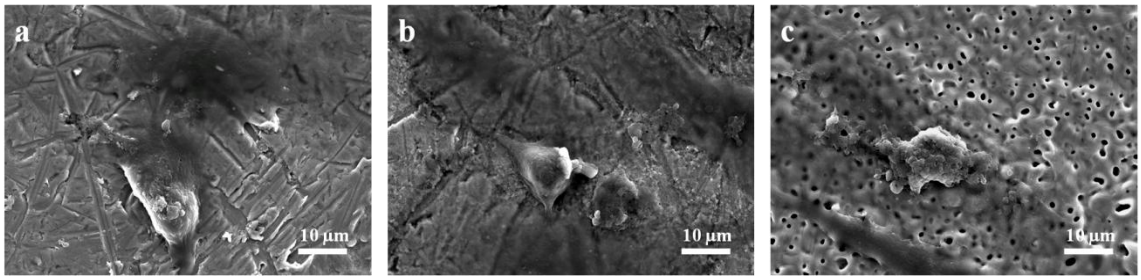

Figure 31 - SEM images (x1,500) taken from Day 7 of the hFOB culture (a) control, b) 0.5 A condition, and c) 1.0 A condition). No significant differences in cell morphology were observed on the different treatments over the course of the study.

7.4 Conclusion

This work demonstrates that 300 eV helium ions can be used to create a micro-porous surface on Ti6Al4V titanium alloy. Furthermore, the relative size and number of pores created is dependent on the processing temperature; substrates processed at a temperature of approximately 450 °C produced a large number of sub-micron sized pores, while temperatures near 600 °C resulted in fewer but larger pores. A week long culture of hFOB 1.19 cells on the substrates showed the helium etched topographies had no negative impact on cell health. Results from the MTT assay suggest the helium treatment increases cellular activity once cells have adhered to the surfaces. In addition, the porous nature of these surfaces may be useful for applications such as better securing biomedical coatings like hydroxyapatite, or serving as a carrier for antibacterial agents in targeted drug delivery on implants. The results of this study demonstrate that helium texturization is a technique that warrants further investigation for use on orthopedic devices. Future efforts will be directed towards elucidating the exact roles of temperature and ion energy on pore formation, as well as a more in-depth evaluation of how these surfaces will affect osteoblast function in a culture of primary cells.

8 Helium Etching to Create Aluminum Nanostructures and their Relevance to Ice Phobic Surfaces

(Specific Aim 5)

8.1 Introduction

8.1.1 Helium Texturization

Over the course of fusion materials research, the low energy, high flux helium irradiation of tungsten has lead to discovery of complex nanostructuring events not previously associated with helium damage. During these investigations, tungsten samples were immersed in dense helium plasma and biased to irradiate the surface with ions. This is a departure from traditional helium implantation techniques that have previously relied on ion accelerators or the tritium trick to introduce helium into a material. The mechanisms responsible for the formation of these unique fibrous surfaces (known as fiberform) remain largely un-elucidated, though the trends observed in the characteristics and topographies produced by the exposure of tungsten surfaces to helium plasma suggest that they may be controlled.

These texturizations have only been observed under a limited range of conditions in fusion diverter simulators. The formation of this nanostructure is dependent mostly on: substrate temperature, ion energy, ion flux, and ion fluence. Since the formation of these nanostructured surfaces is relatively new, the evolution of different materials under similar irradiation conditions have not been previously investigated. It is possible that the limited understanding of these helium/material interactions available in the published literature on tungsten can be used to guide the development of similar surfaces on new materials.

8.1.2 Ice Resistant Surfaces

The interactions between water and a surface can often be correlated to the adhesion strength of ice. Typically, surfaces displaying super-hydrophobic properties (high water contact angle and low contact angle hysteresis) are capable of reducing ice adhesion. Super-hydrophobic surfaces are traditionally created by taking a hydrophobic material and texturizing the surface to alter the wetting properties and induce a Cassie-Baxter wetting regime. One example of an effective and well know super-hydrophobic surface is the lotus leaf. The observed wetting properties are owed to both the slightly hydrophobic properties of its waxy coating and the complex nodule and fibrous structuring of the leaf surface. By creating a lotus-like nano-structure on aluminum, it may be possible to mimic the super-hydrophobic effects result in improved ice resistance. Although aluminum is naturally hydrophilic, it has been theoretically proven that the creation of super-hydrophobic surfaces from hydrophilic materials may be possible [157].

8.1.3 Helium Processing for Ice Resistant Surfaces

The purpose of this work is twofold: 1) characterize the evolution of aluminum surface topographies under helium ion bombardment, 2) investigate the possible use of helium ion bombardment to produce robust super-hydrophobic topographies capable of reducing the adhesion strength of ice. Changes in surface structure were characterized as a function of helium ion energy and substrate temperature through scanning electron microscopy (SEM). Results were obtained for two of the most widely used aluminum alloys: 2024 and 6061. These findings were then used to create aluminum surfaces with topographies mimicking the micro- and nano-

structures observed on the lotus plant, in efforts to create a super-hydrophobic surface. Ice adhesion was then characterized by measuring the shear strength of the ice/surface interface.

8.2 Materials and Methods

Sheets of 20 ga. aluminum alloys 2024-T3 and 6061-T6 (Online Metal Supply) were mechanically sheared into 2.5 cm x 2.5 cm substrates. The top of each substrate was protected by a thin polyvinylchloride (PVC) layer, laid by the manufacturer to protect the surface. Immediately before helium treatment, the PVC coating was peeled off and surfaces were wiped with acetone to remove possible residue.

8.2.1 Helium Ion Bombardment

To irradiate substrates with helium, a custom plasma reactor was designed and constructed. Titanium sheet metal was sheared and assembled as shown in Fig. 32. The reactor consisted of an open box cathode (held at negative potential), a biased substrate holder (held at a second negative potential), and a plate anode (grounded). This configuration offered a wide range of processing flexibility and allowed substrates to be biased independently of the cathode to control the energy of the irradiating ions. A ceramic-potted resistive heater (P-VFR-6-6, Thermcraft, Inc.) placed beneath the reactor heated substrates to temperatures of nearly 475 °C. Ceramic wool insulation (Superwool, Morgan Thermal Ceramics, Inc.) was placed around the outer surfaces of the cathode to limit plasma coupling to the chamber walls.

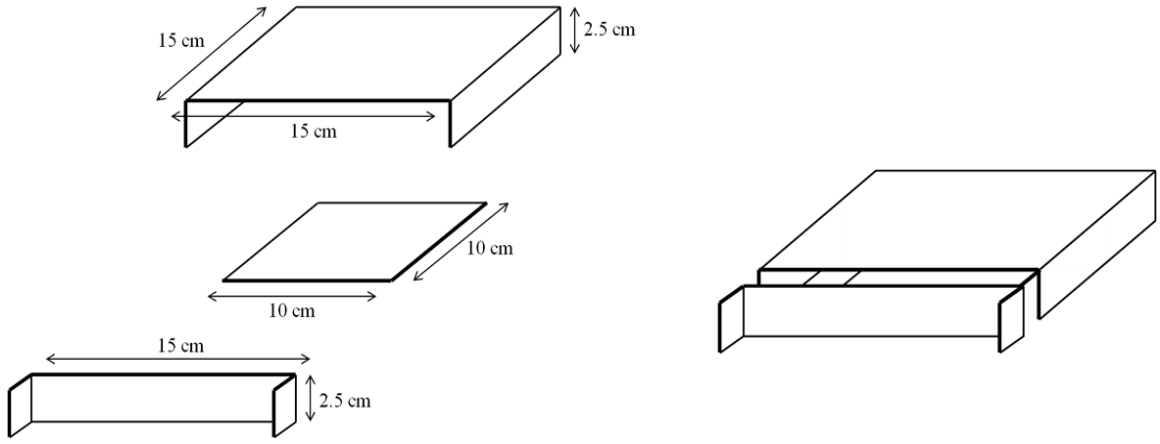

Figure 32 - (Left) Dimensions of the plasma reactor components (top – cathode; middle – substrate holder; bottom – anode), (Right) assembled reactor.

A Leybold-Heraeus D16A mechanical pump was used to evacuate the chamber to a baseline of 150 mTorr. During processing, the mechanical pump was left running and the chamber was continuously backfilled with helium to a pressure of approximately 2 Torr. A MDX Magnetron power supply (Advanced Energy) was used to negatively bias the cathode and drive the plasma discharge. The substrate holder was negatively biased with a Spellman SL600 supply.

Processing voltages and currents varied depending on the parameters tested. Aluminum 6061-T6 substrates were tested at 150, 250, and 350 °C with bombarding ion energies of approximately 50, 100, 200, 300, 400, and 500 eV. This alloy was additionally tested at 200, 300, and 400 °C with bombarding ion energies of approximately 100 and 200 eV to better characterize surface transformations over this temperature range. Aluminum 2024-T3 substrates were tested at 150 °C with bombarding ion energies of approximately 100, 300, and 500 eV; and 250 °C with bombarding energies of approximately 100, 200, 300, 400, and 500 eV. These temperature ranges were selected as they correspond to the approximate absolute temperatures wehre surface feature development has been observed on tungsten. Four substrates were

processed at a time for durations of 15 minutes. First, a plasma discharge was struck by biasing the cathode. Once stable plasma was formed, the substrates were biased to the value desired. The cathode discharge was then current regulated at 0.2 A and the cathode voltage was allowed to fluctuate as needed. Current regulation was used to provide a similar flux to the substrates across all the testing conditions.

The temperature in the reactor was monitored by submersing a thermocouple (potted in a ceramic compound inside an alumina tube) in the plasma environment during operation. A small band of stainless steel sheet metal was also placed over the alumina, allowing the probe to be biased and exposed to a plasma environment that closely simulated the exposure conditions of the substrates. Temperatures during processing ranged ± 20 °C due to thermal lag between the heater and the substrate holder as well as heat gained from the plasma environment.

A Langmuir probe was used to characterize the plasma in the reactor near the substrate locations for several running conditions. Electron densities ranged from 2×10^{14} to 1×10^{16} m^{-3} with electron temperatures ranging from 3 to 5 eV. Plasma potential varied from -11 to -26 V depending on conditions of operation (Fig. 33). To achieve more accurate ion energies during bombardment, substrate bias was set 10 V more negative of the desired voltage to partially compensate for the plasma potential being -11 to -26 V from ground.

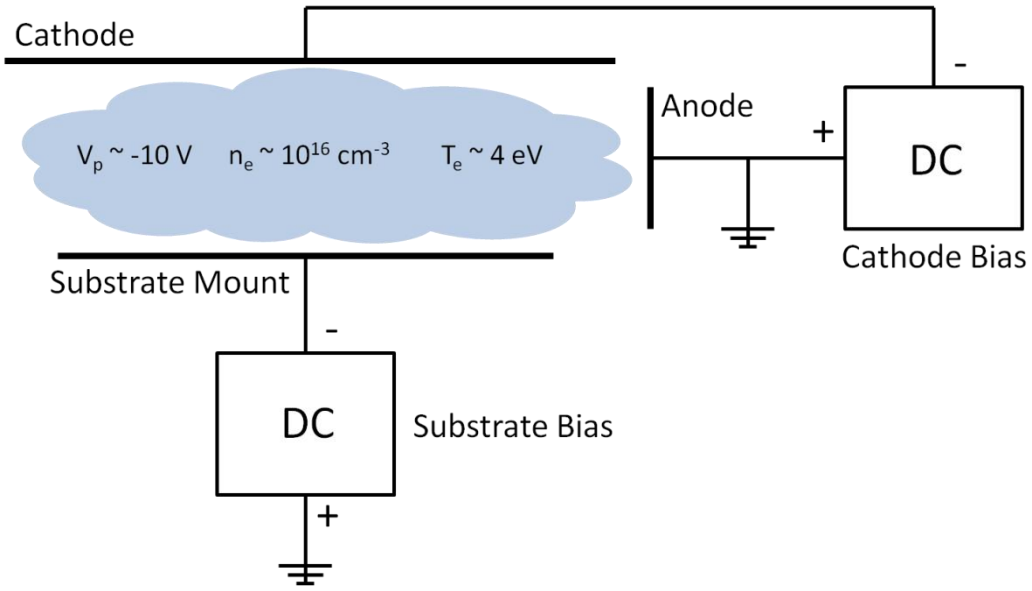

Figure 33 - Electrical schematic of the reactor with typical plasma properties. Note, for these operating conditions, ions from the plasma are accelerated to the substrate and strike with an energy equivalent to the potential difference between the substrate and plasma.

Mass measurements (with a resolution of 20 µg) of substrates taken before and after plasma exposure were unable to distinguish any net loss of material sputtered during the 15-min long treatment time. This was expected due to the low sputter yield of helium ions.

Substrate topography was evaluated using a scanning electron microscope (SEM, JEOL JSM-6500F). Surface imaging was performed without gold coating with 15 keV electrons at a working distance of 10 mm.

Water contact angle measurements were also performed on the substrates using a FTA1000 B Class (First Ten Angstroms, Inc.) goniometer. A droplet of distilled water, approximately 50 µL in volume, was formed on the tip of the syringe and pushed down until the bottom of the droplet contacted and moved to the surface. An image was captured 5 seconds after surface contact by a camera level with the substrate. Images were then processed with the

accompanying Fta32 software to calculate the contact angles. One substrate from each preparation was tested in three separate locations, the reported values are the average of these three tests.

8.2.2 Measuring Ice Adhesion

Ice adhesion was measured by shearing frozen water columns from the substrate surfaces. Spent 9mm bullet casings were used to contain the water due to their convenience and known orifice diameter. The used primer was drilled from the back of each shell to allow them to be filled while the casings were face down on the substrates. Residual gunpowder contamination was removed through ultrasonic cleaning consisting of 15 min. periods in Simple Green solution, water, and finally acetone. After the casings were placed on the substrates, a syringe was used to fill each shell with 0.6 mL distilled water. The substrates with filled casings were then moved to a commercially available chest freezer (FCCS151FW3, Frigidaire) and cooled to ~ -10 °C. Substrates were held at temperature for at least 12 hours before testing.

Without removing from the freezer, substrates were then individually mounted on a linear track and manually loaded until a floating beam sheared the frozen casings from the surface. During this process the applied force was monitored by strain gauges. Ice adhesion strength was calculated by taking the maximum force obtained before the break and dividing by the known cross-section of the casing. This method is similar to the one presented by Meuler et al. [106].

8.3 Results and Discussion

8.3.1 Aluminum 6061-T6 Helium Irradiation

Aluminum alloy 6061-T6 is well known for its enhanced mechanical properties; the T6 temper designates that the alloy has been solution heat treated and artificially aged. This alloy and temper were chosen because of its popularity and widespread general use. The primary alloying elements in 6061 consist of (percentage by weight): magnesium (0.8 - 1.2 %), silicon (0.4 - 0.6 %), copper (0.15 - 0.4 %), and chromium (0.04 - 0.35 %). Other elements are also present, but in low concentration. The melting for this alloy can occur between 582 - 652 °C. For analytical purposes in this work, the melting point is assumed to be 617 °C. Additionally, as is the case with aluminum and all aluminum alloys, 6061 forms a thin, fully dense native oxide layer when exposed to atmospheric conditions and is therefore naturally corrosion resistant.

Helium ion exposure was performed according to the previously defined test matrix. Averaged results for the ion flux and total ion fluence delivered to the substrates during processing are provided in Table 4 and Table 5 respectively. The values reported were calculated using the current read from the power supply used to bias the substrates and have not been corrected for secondary electron emissions from the aluminum substrates or the exposed portions of the underlying titanium plate used as the substrate mount. Due to this fact, these estimates could be as much as 30 % higher than the conditions actually experienced by the substrates [156].

Table 4 - Average ion flux recorded during each testing condition.

Ion Flux (Ions/m^2*s)						
	50 eV	**100 eV**	**200 eV**	**300 eV**	**400 eV**	**500 eV**
150 °C	3.73E+19	5.33E+19	6.64E+19	8.85E+19	1.14E+20	1.01E+20
200 °C	-	5.38E+19	8.14E+19	-	-	-
250 °C	4.94E+19	6.18E+19	7.79E+19	9.40E+19	1.12E+20	1.03E+20
300 °C	-	6.50E+19	8.76E+19	-	-	-
350 °C	5.57E+19	6.18E+19	7.32E+19	9.72E+19	1.21E+20	-
400 °C	-	1.15E+20	1.16E+20	-	-	-

Table 5 - Total ion fluence as recorded during each testing condition.

Total Ion Fluence (Ions/m^2)						
	50 eV	**100 eV**	**200 eV**	**300 eV**	**400 eV**	**500 eV**
150 °C	3.35E+22	4.80E+22	6.23E+22	8.08E+22	1.01E+23	6.69E+22
200 °C	-	4.87E+22	7.46E+22	-	-	-
250 °C	4.51E+22	5.45E+22	7.04E+22	8.31E+22	1.04E+23	8.07E+22
300 °C	-	5.85E+22	7.67E+22	-	-	-
350 °C	5.02E+22	5.57E+22	6.41E+22	8.82E+22	1.07E+23	-
400 °C	-	1.03E+23	1.04E+23	-	-	-

SEM evaluation of the helium ion irradiated substrates revealed dramatic changes to the surface of the aluminum. Three modes of feature formation were observed: sub-oxide hole formation, nodule formation, and nanostructure formation. These modes could be seen independently or in combination, depending on the conditions tested. Appendix A provides SEM images taken from many of the substrate surfaces.

The dominant feature observed during most irradiation conditions was the evolution of small collections of material or “nodules” across the surface of the material. Below 300 °C, these structures ranged from ~100 nm in size (low temperature) up to several microns in diameter

(high temperature) as shown in Fig. 34. Slight surface texturization was evident even at the lowest values tested (50 eV, 150 °C) though development was more pronounced at elevated energies and temperatures. The highest energies tested resulted in both the formation of nodules as well as the appearance of unique nanostructures across the surface (Fig. 35). This is the first time either formation has been observed on aluminum as a result of helium ion bombardment, likely owing to the method of irradiation used. Previous investigations have relied on the use of high energy ion accelerators or tritium trick to introduce helium into the aluminum substrate. The technique applied in this work allows for the irradiation of low energy ions in a plasma immersion environment, resulting in the formation of the unique surface structures.

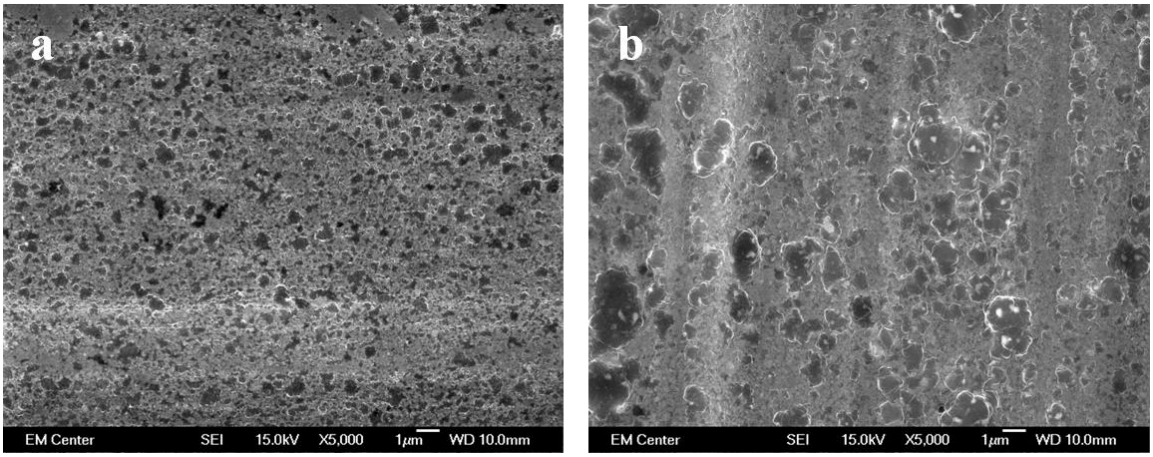

Figure 34 - Images of nodule formation on (a) 150 °C, 300 eV, and (b) 200 °C, 200 eV substrates.

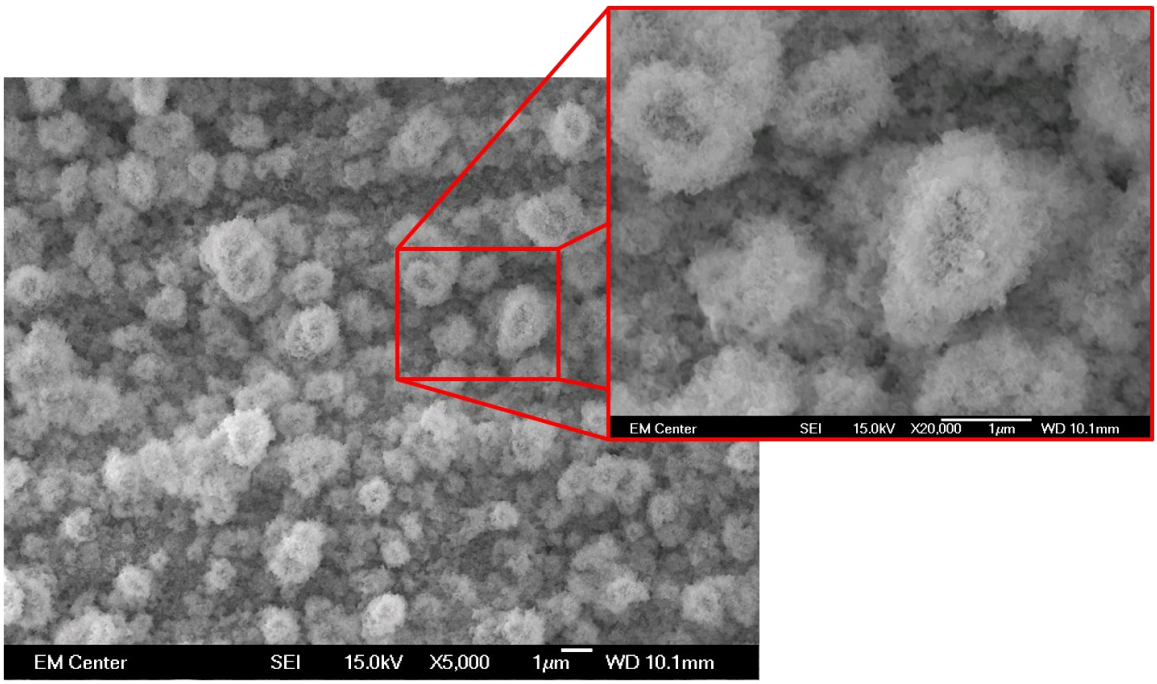

Figure 35 - Nodule and nanostructure formation at 250 °C, 500 eV.

Under conditions of high ion energy bombardment at high temperatures, nodule formation was still observed, but on a much larger scale; individual nodules could be resolved on some substrates without the aid of instrument magnification (Fig. 36). The geometry and physical structure of these formations were similar to those observed at lower temperatures, suggesting no difference in formation mechanics. It is therefore probable that the larger structures are a product of increased surface atom mobility and diffusion resulting from elevated temperatures. Irradiation at 350 °C, 400 eV produced similar nanostructures to substrates bombarded at 150 and 250 °C, however a stable plasma discharge could not be maintained at 350 °C, 500 eV and consequently was not evaluated.

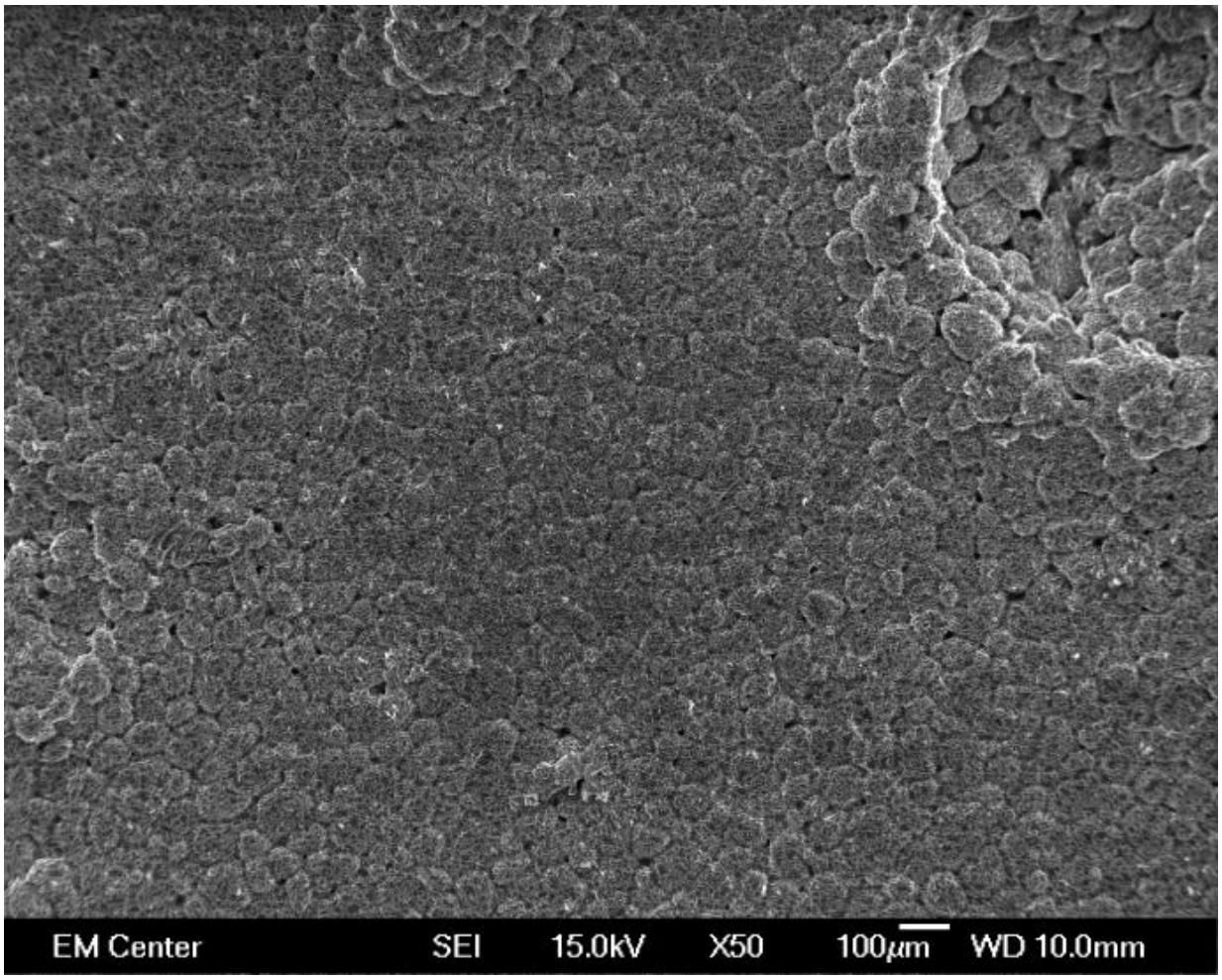

Figure 36 - Large nodule formation as seen on a substrate treated at 350 °C, 400 eV. A crater left by the collapse of a large bubble is visible in the top right corner of the image.

At lower ion energies (200 eV and below) and higher temperatures (above 250 °C), the native oxide layer remained largely intact over the aluminum and no features were generated on the surface. However, helium was still able to penetrate the oxide and create a porous surface beneath the protective cover. Fig. 37 shows some SEM images of these substrates. This regime is unique as there appears to be little or no evolution of surface features; all material displacement from bubble growth occurs in the bulk of the substrate. It is likely that similar void nucleation and bubble growth between the oxide and alloy were occurring for temperatures 250

°C and below on a scale too small to be observed, or may have been obscured by nodule growth. At energies greater than 200 eV the oxide was no longer visible and presumably had been sputtered away.

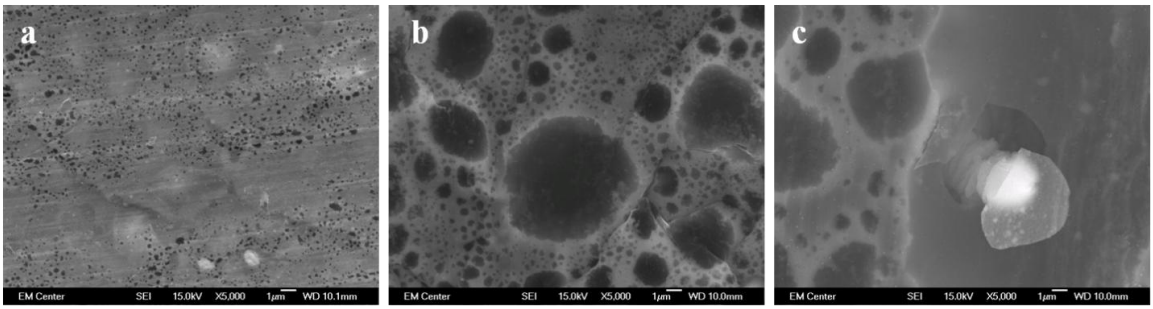

Figure 37 - SEM images of sub-oxide hole formation: (a) 300 °C, 100 eV, (b) 350 °C, 200 eV, and (c) 400 °C 100 V. Hole size can be directly correlated to substrate temperature. Image (c) shows an aluminum microstructure that has broken through the oxide layer.

Finally, the most extreme conditions tested resulted in dramatic physical alterations to the samples. Under these conditions substrates would warp, resulting in a change to the bulk dimensions, and form millimeter size bubbles that could either stay entirely contained in the alloy or burst on the surface leaving gaping craters. Substrates suffering from this damage were considered destroyed (Fig. 38). A representative plot of the observed surface evolutions is presented in Fig. 39.

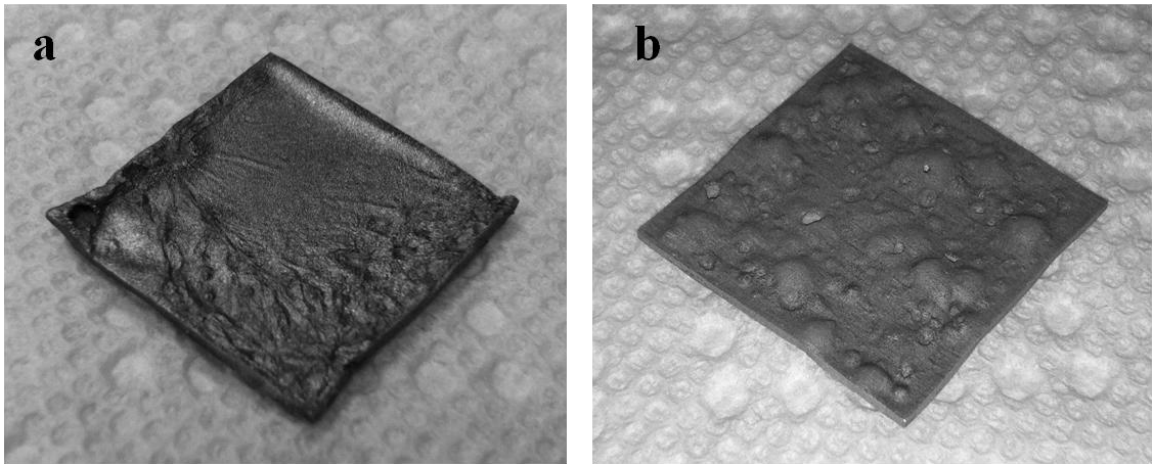

Figure 38 - Examples of substrates destroyed by processing: (a) 400 °C, 100 eV and (b) 350 °C, 400 eV.

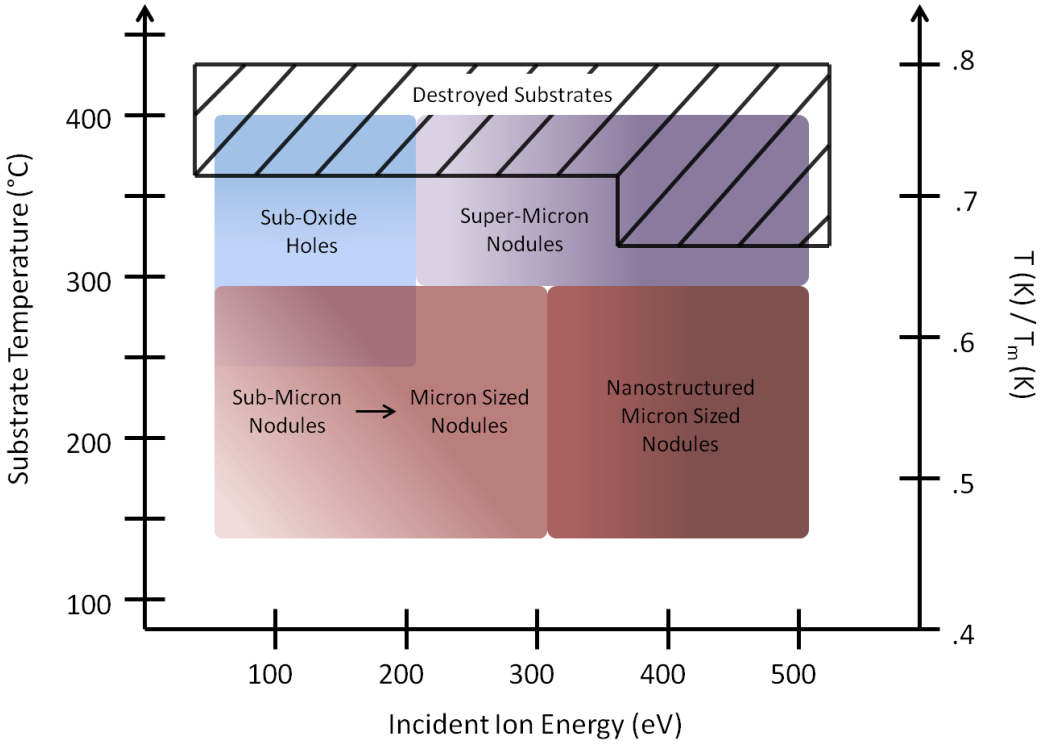

Figure 39 - Representative plot of surface modification as a function of substrate temperature and ion energy for an ion fluence of ~ 10^{23} ions/m^2.

8.3.1.1 Surface Evolution

To better understand the formation of these surfaces, several tests of varying duration were run at 250 °C, 300 eV. Images from these tests are shown in Fig. 40. After only 1 min. of exposure, the surface is uniformly covered in thin, micron sized nodules. By 5 min., larger nodules have begun to group and coverage becomes more sporadic; a decrease in the size of thin nodules over the remaining surface is also observed. This suggests material is being transported to the surface from the bulk, and once on the surface, smaller material aggregations remain mobile and capable of migration. The 10 min. substrate showed continued growth of the larger nodules while the background surface remained populated by much smaller collections of material. By 15 min., nodules have appeared to reach a critical size and growth has abated. Between 15 and 30 min. the material begins to form a nanostructure, covering the surface. Steady state surface development appears to be achieved by 30 min. as there are no changes to the surface after 60 min.

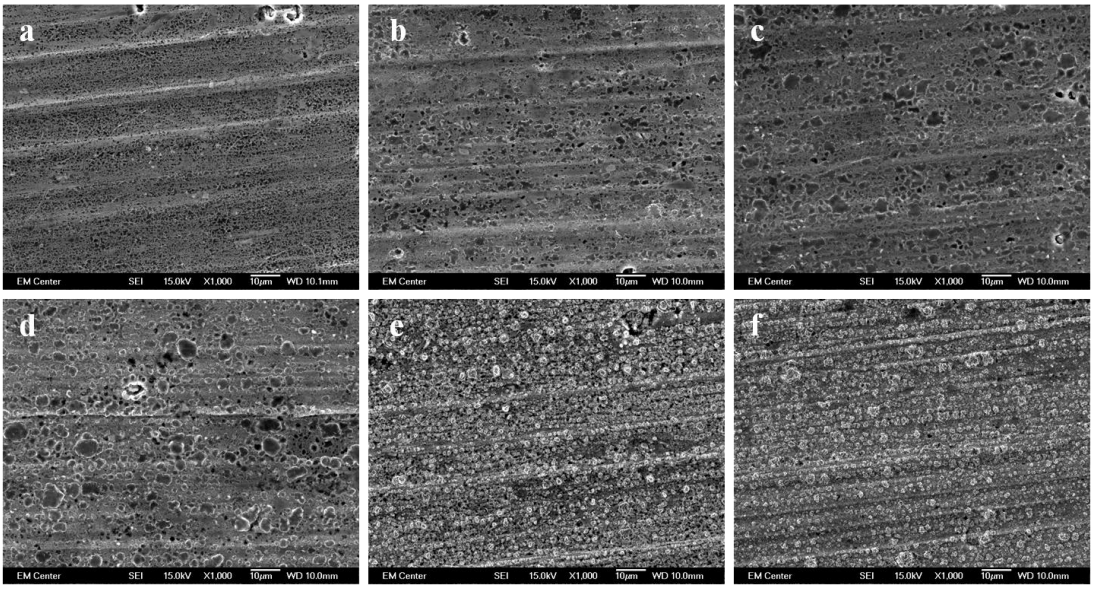

Figure 40 – Substrates processed at 250 °C, 300 eV after: (a) 1 min., (b) 5 min., (c) 10 min., (d) 15 min., (e) 30 min., and (f) 60 min.

The effect of ion flux on the development of the surface structure was also briefly investigated. Fig. 41 compares the normal substrate treated at 250 °C, 300 eV with a substrate treated under the same conditions with a lower flux. Specifically, the standard sample was processed with a flux of 9.40 x 10^{19} ions/m^2*s to a total fluence of 8.31 x10^{22} ions/m^2. The low flux substrate was treated with a flux of 3.40 x 10^{19} ions/m^2*s to a total fluence of 6.02 x 10^{22} ions/m^2. Although the total number of ions delivered to the surface was similar, feature formation on the low flux substrate was much less pronounced than the substrate treated by the higher flux. It is possible that lower fluxes and the resulting lower helium concentrations limit self-trapping mechanisms, reducing the displacement and subsequent migration of alloy atoms. Less material is then relocated to the surface, hindering development of features. Complete elucidation of the role ion flux plays in feature formation was beyond the scope of this work; however, future studies should note flux is clearly an important variable.

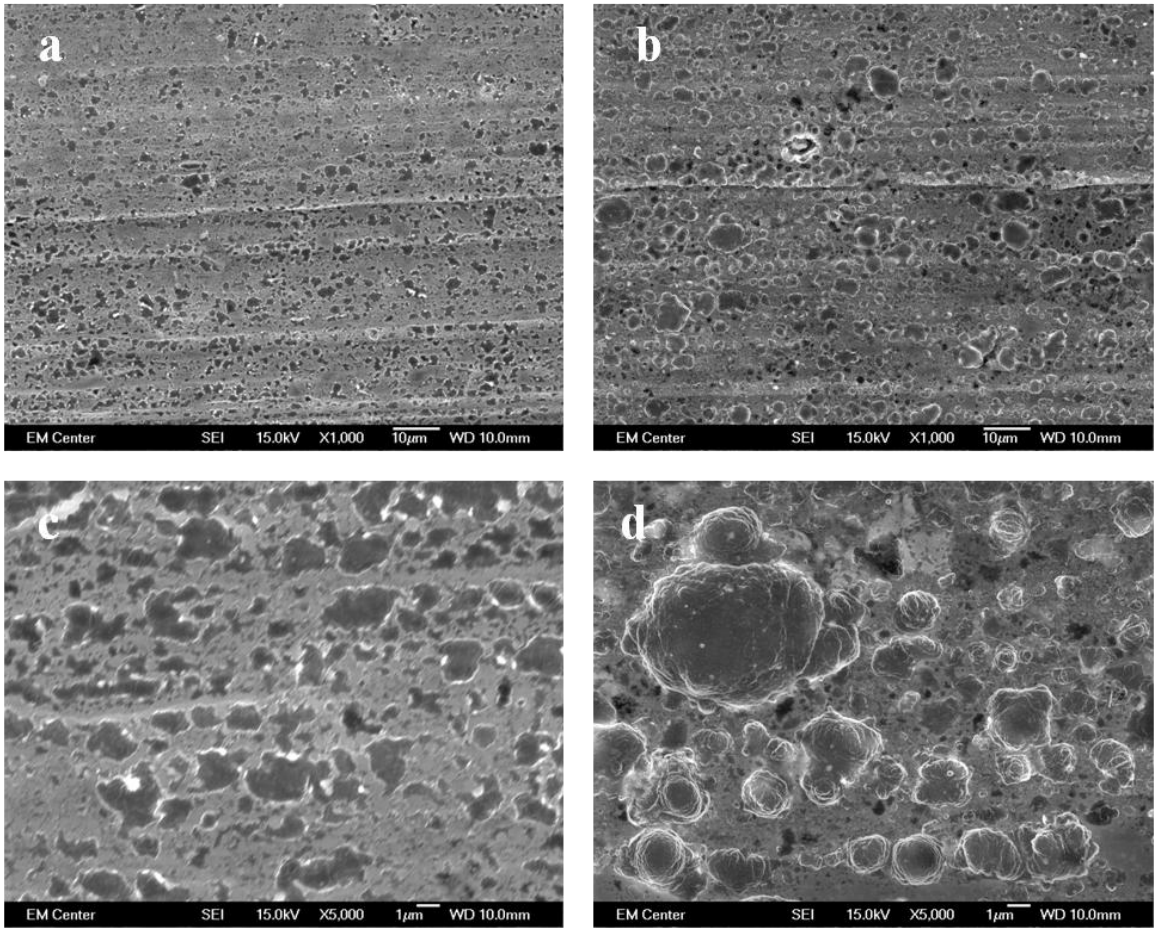

Figure 41 - Low flux samples (a) and (c) compared to standard treatment (b) and (d) at two different magnifications. Features on the low flux substrates are underdeveloped in comparison.

8.3.1.2 Mechanisms of Formation

Traditional helium damage such as void and bubble formation was evident in nearly all conditions tested except the lowest temperatures and ion energies. Mechanisms for the formation of these features have been well documented by other researchers and were discussed in the introduction. However, the formation process of unique micro- and nano- structures, such as fiberform on tungsten (or the structures on aluminum alloys as observed in this work) is not well understood. Precise determination of the mechanisms responsible for these surface evolutions is difficult due to the fundamental complexity of the systems. In addition to the

traditional damage associated with helium implantation and diffusion through the material, a number of other factors must be considered including: influence of the oxide layer, elevated temperatures, sputtering events, and effects of the induced electric field between the plasma and biased substrate surface.

8.3.1.2.1 *Oxide Effects*

The SRIM (Stopping and Range of Ions in Matter) software package was used to calculate average implantation depths of 2.4 nm (1.3 nm straggle) and 7.2 nm (4.0 nm straggle) for helium ion energies of 100 eV and 500 eV respectively in an aluminum target. The thickness of native oxide is dependent on the processing conditions during sheet metal formation, but typically results in an oxide thickness of a few nanometers. This means implantation potentially occurs mostly in the oxide layer at low energies and very near the oxide/alloy interface at high energies. Despite the ability to maintain a protective layer under low energy bombardment, the oxide appeared largely inconsequential. Fig. 42 shows preferential bubble nucleation at a crack in the oxide, indicating the oxide was slightly inhibitory though mostly ineffective at abating the helium bombardment. Helium is also known for its affinity to trap at lattice defects when diffusing through a material. It is possible that bubble nucleation favored the oxide/alloy interface and the natural defects resulting from lattice mismatch. This was not experimentally confirmed as this confirmation would have required the development of complex controls beyond the scope of this work.

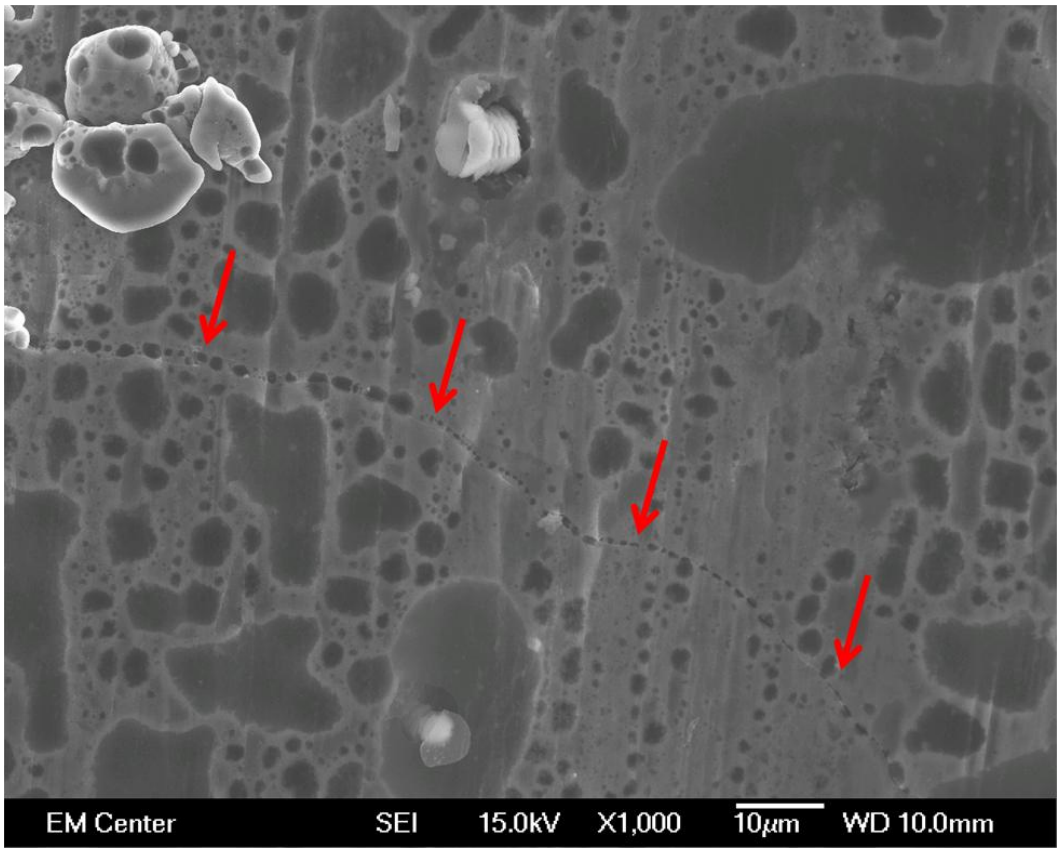

Figure 42 - Increased bubble nucleation along a crack in the oxide (400 °C, 100 eV).

8.3.1.2.2 *Temperature Effects*

Substrate temperature was one of the most influential factors in the development of topographical features. Self diffusion rates increase exponentially with temperature, allowing small increases in temperature to dramatically effect atomic movement and reorganization in the alloy structure. This likely explains the variation in feature sizes. As the temperature was increased, the dimension of the features grew (a trend observed in both bubble and nodule sizes). Since more diffusion was naturally occurring, atomic rearrangement resulting from helium damage and the other factors shaping the features was exaggerated.

8.3.1.2.3 *Sputtering Effects*

The sputtering threshold for helium atoms on aluminum has been measured to be as low as 35 eV [158]. This meant that under all the conditions tested, helium would be able to sputter exposed aluminum surfaces. However, since helium is such a small atom it is unable to deliver much energy to the surface and therefore has a very low sputter yield. Reported values are 0.005 atoms/ion at 200 eV, 0.008 atoms/ion at 300 eV, and 0.021 atoms/ion at 600 eV [156]. No information could be found for the sputtering of aluminum oxide by helium. The increased bond strength of the oxide is likely to result in a higher sputtering threshold and lower sputter yield compared to the aluminum. It appears the oxide remains unaffected up to energies of 200 eV. At energies of 300 eV and higher, it is unclear if the removal of the oxide is a result of helium sputtering or physical disturbance from the evolving microstructure beneath. Measurements made before and after each run were unable to record a loss of mass on the substrates, even at the highest ion energy studied. It is therefore unlikely material removal plays a key role in the formation of the microstructure, though limited sputtering may still influence nanostructure development.

8.3.1.2.4 *Electric Field Effects*

One aspect that has been previously ignored in discussions of helium induced micro- and nano- topographies has been the influence of the electric potential between the biased substrates and the irradiating plasma. Most previous studies examining the damage effects of helium ion bombardment have used high energy ion beams or the tritium trick to irradiate samples, so no electric field above the substrate surface was induced. Consequently, the only damage mechanisms observed were the bubbles, blisters, and holes previously discussed. More recent

studies have immersed substrates in a plasma environment and biased the samples to induce ion bombardment. It is only in these studies that the formation of complex surface features (such as fiberform and the features observed in this work) has been observed. Under such conditions, a strong electric field (dependent on the substrate bias relative to the plasma as well as the characteristics of the plasma sheath) is created at the substrate surface.

Although individual alloy atoms are never themselves ionized, bombarding helium ions can create partial polarization as they move into and through the aluminum [159-161]. It is possible that high flux of helium ions to the surface could result in the polarization of atoms at the surface. This region could then respond to the high electric field and experience forces strong enough to influence the migration already occurring due to the increased temperature and displacement of alloy atoms by the irradiating helium. Under average testing conditions, the sheath thickness was a little under 1 cm. Electric field strength was therefore approximated as the substrate bias voltage per cm. This would not be the first time such events have been witnessed as electric fields of comparable intensities have been used to influence the growth of surface features [162-170]. Characteristic responses of material reorganization under electric fields include enhanced coalescence of material (formation of nodules) as well as increased roughness (growth of features); both of which were directly observed in the formation of surfaces in this work.

If the material is indeed forming micro- and nano- structures in response to an applied electric field, this would explain why such features had not been seen previously under traditional irradiation. More research needs to be done focusing on this interaction to state conclusively the effects of the electric field are responsible for the self-organization of these complex surfaces, but the observed results support this theory.

8.3.2 Aluminum 2024-T3 Helium Irradiation

Aluminum alloy 2024 has become an industry standard in the aerospace industry due to its high strength and excellent fatigue resistance. The primary alloying elements in 2024 consist of (percentage by weight): copper (4.3 - 4.5 %), magnesium (1.3 - 1.5 %), and manganese (0.5 - 0.6 %). Again, additional elements may be present but in lower concentration. There is no single melting point for 2024 alloy; high diffusion from phase transitions and localized melting occur between 502 - 638 °C. Since processing occurs well below these temperatures, for comparative purposes an intermediate melting point (570 °C) will be used as an assumed absolute melting temperature.

Feature formations observed on the 2024 alloy were similar to those observed for 6061. The helium irradiation again resulted in the formation of nodular structures over most of the conditions tested. Appendix B provides SEM images taken from many of the substrate surfaces. Fig. 43 shows a comparison of the alloys when subjected to the same processing conditions. Features on the surface of the 2024 substrates are much larger and more developed than the counterparts on the 6061 alloy. This difference is likely attributed to the increased diffusion of the 2024 alloy (a result of the lowered melting point) where more material is able to reach the surface and therefore feature development is enhanced. The same trends observed in the 6061 could be applied to the 2024 substrates when referenced to the absolute melting temperature (Fig. 44). It is likely that this relation of surface modification to absolute temperature and ion energy could continue to be applied to all aluminum alloys and possibly other materials assuming diffusion and charging mechanisms remain similar.

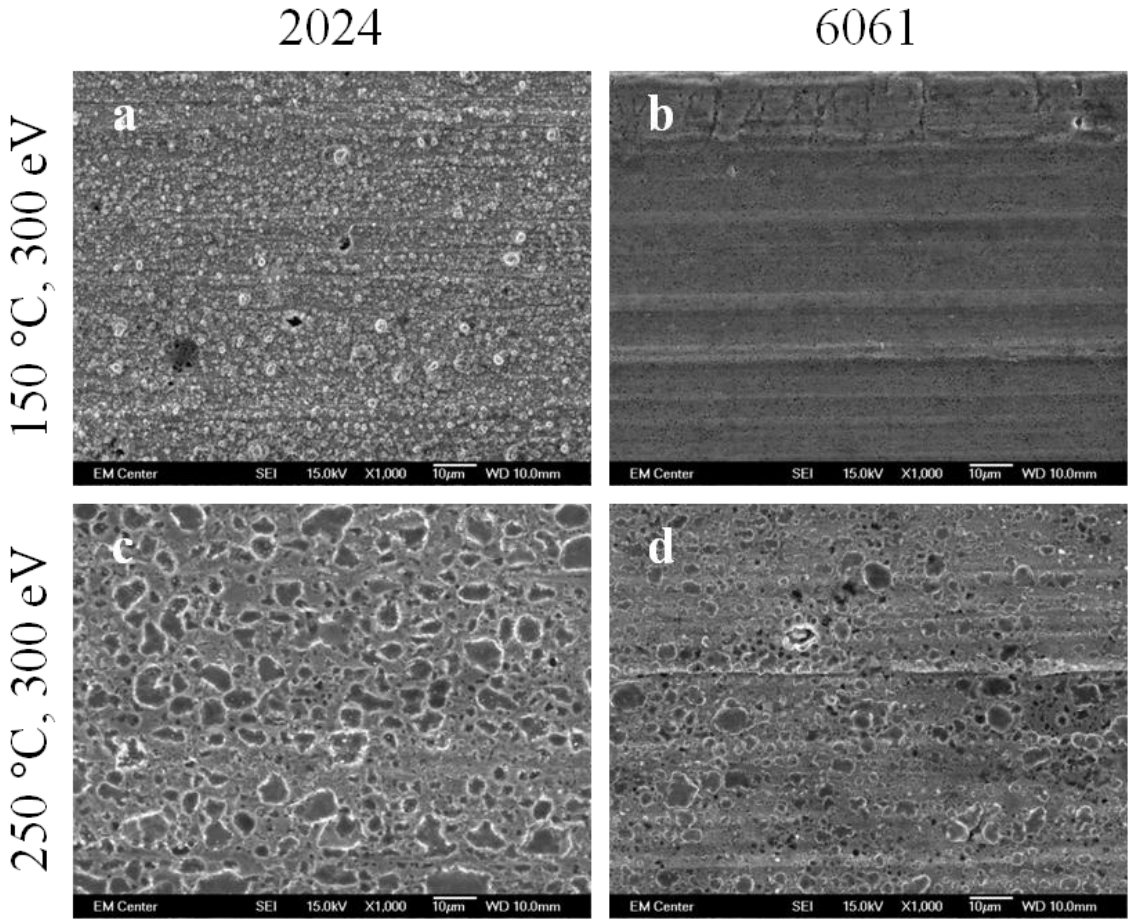

Figure 43 - Comparison of the 2024 alloy (a) and (c) with 6061 alloy (b) and (d), treated at two seperate conditions.

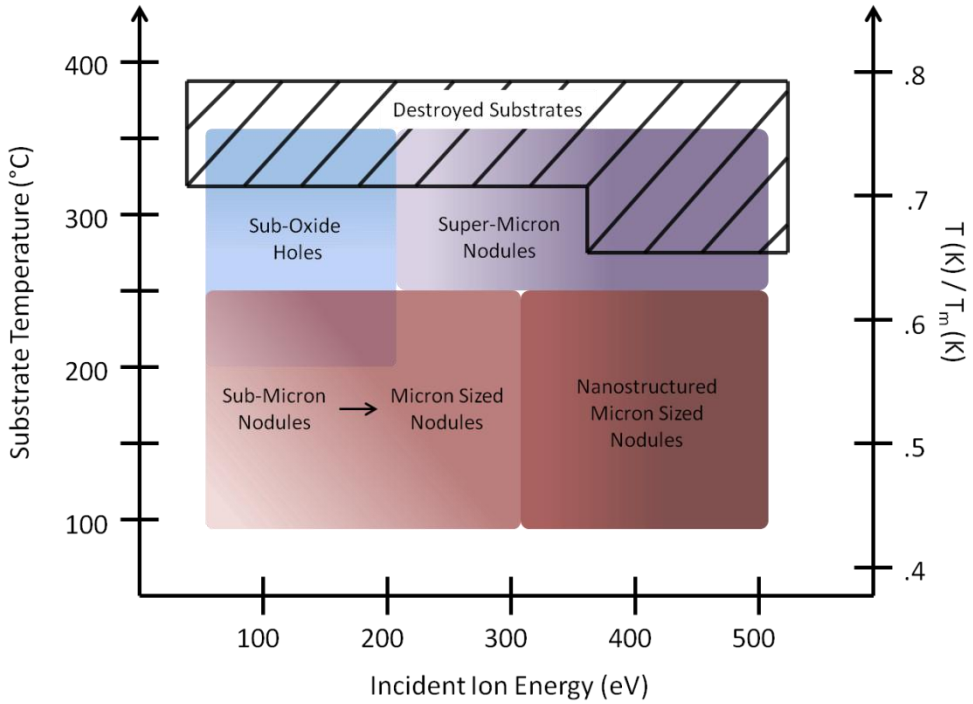

Figure 44 - Representative plot of surface modification as a function of substrate temperature and ion energy for 6061 alloy, shifted to reflect the results seen on the 2024 alloy.

The method of processing used raised two concerns: a) since the cathode is also biased and under helium bombardment, is it possible that titanium is being sputtered onto the aluminum substrates and a seeding effect is responsible for development of these features, b) since an alloy is being used, is it possible that the alloying elements are experiencing increased diffusion and that the features formed are not aluminum but consist largely of an alloying element. To investigate these possibilities, the elemental composition of the 2024 alloy surface after treatment at 250 °C, 500 eV was examined using energy-dispersive x-ray spectroscopy (EDS). The results are shown in Fig. 45. It can be clearly seen that the features consist primarily of aluminum. Alloying elements of copper and magnesium are also clearly present, as well as the

oxygen associated with the aluminum oxide layer. This indicates the features are evolving primarily as a result of increased diffusion and displacement from all alloying elements, not preferential migration of any single element. Also, no titanium was detected on the surface indicating that seeding events were not a factor in the generation of these topographies.

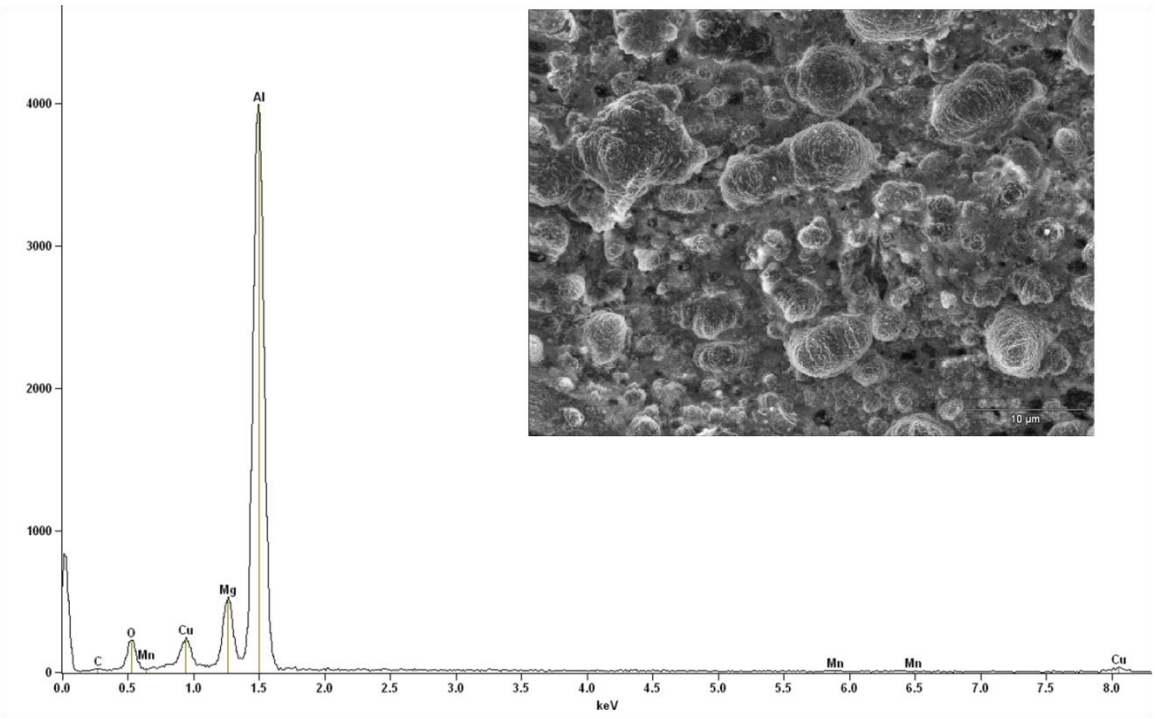

Figure 45 - EDS spectrum for 2024 alloy treated at 250 °C, 500 eV.

8.3.3 Ice Resistant Surfaces

One goal of this study was to use helium ion texturization to create a surface mimicking the micro- and nano- structure of the lotus leaf. It was believed that such topography would be capable of reducing the contact area of water with the aluminum surface and thereby decrease ice adhesion. Helium texturization proved capable of creating this complex hierarchical structure,

however the observed results were opposite of those anticipated (Table 6 and Table 7). Water contact angle studies revealed that the more the topography of the aluminum surface resembled that of a lotus, the affinity for water increased. Instead of features inducing a Cassie-Baxter state, extreme Wenzel wetting was observed. The complex nature of the surface induced a wicking effect capable of completely pulling the water droplet to the aluminum surface (superhydrophilic).

Table 6 - 6061 Water Contact Angle

Water Contact Angle (Degrees) - Alloy 6061						
	50 eV	**100 eV**	**200 eV**	**300 eV**	**400 eV**	**500 eV**
150 °C	60.9	58.2	58.3	45.5	13.7	Too Low
200 °C	-	61.3	71.3	-	-	-
250 °C	56.4	62.2	59.2	Too Low	Too Low	Too Low
300 °C	-	52.2	34.3	-	-	-
350 °C	48.3	62.1	53.0	30.3	-	-

Table 7 - 2024 Water Contact Angle

Water Contact Angle (Degrees) - Alloy 2024					
	100 eV	**200 eV**	**300 eV**	**400 eV**	**500 eV**
150 °C	35.4	-	17.8	-	Too Low
250 °C	40.7	34.2	22.4	Too Low	Too Low

Ice shearing of helium irradiated surfaces was unable to reveal any variation in adhesion from untreated aluminum. Additionally, the breakage of ice from the surface was often violent enough to damage or remove the aluminum microstructure. Furthermore, surfaces displaying superhydrophilic properties were unable to be evaluated because on these substrates, water would wick out from under the casing to cover the entire sample surface. This situation resulted

in it not being possible to maintain a fixed area for evaluation. Even if a fixed area were maintained there is no evidence that these surfaces would have been more robust than those tested.

8.4 Conclusion

This study has demonstrated that low energy helium irradiation of 6061 aluminum alloy is capable of forming complex surface features. The dominant feature observed during most irradiation conditions was the evolution of small collections of material or "nodules" across the surface of the material; although hole and bubble formations were also seen. At sufficiently high ion energies, the surfaces also developed a complex nano- structured "fuzz". The size of these structures was directly related to the substrate temperature; higher temperatures resulted in larger features. It was also shown that the formation trends observed on the 6061 alloy could be applied to the 2024 alloy when referenced to the absolute melting temperature of the material. This suggests that these results may be extended to additional aluminum alloys or other materials entirely. Although the precise mechanisms of feature development where not ascertained, evidence suggests a combination of increased material transport to the surface from elevated temperatures and helium displacement and interactions between mobile atomic aggregates and the induced electric field are responsible.

Helium texturizatoin of aluminum was capable of producing a surface that closely mimicked the micro- and nano- structure of the lotus plant, however, these features resulted in superhydrophilic properties instead of inducing the superhydrophobic state seen in nature. When texturized surfaces were tested for ice adhesion, the surface structures were often damaged or destroyed and no difference could be observed between the treated and control surfaces. A lotus-

like structuring of aluminum alone is therefore not a viable method to produce ice phobic surfaces.

9 Conclusion and Future Work

9.1 Conclusion

The goal of this work was to demonstrate the ability of plasma processing to create self-organized surfaces with tailored patterning on the micro- and nano- scale or altered surface chemistry for practical industrial or biomedical applications. This ability was clearly demonstrated through five separate projects.

Argon etching at both normal and oblique incidences was used to create surfaces shown to alter cell behavior. Normal incidence argon etching produced a micro-scale texturization of plateaus and valleys due to the uneven etching of grains, as well as a nano-scale patterning of wave-like formations. This etching had a largely positive impact on cellular interaction with increases in cell spreading and mobility. Oblique angle etching at 30° and 75° was used create uniform networks of randomly distributed, needle-like structures. Cells on the 30° etched surface inhibited cell spreading while cells on the 75° etched surface showed preferential elongation. Combined, this work illustrates the ability of ion patterned surfaces to affect cell function with potential applications on biomedical devices.

Oblique angle oxygen etching was used to improve the native oxide layer on biomedical grade titanium. Results demonstrated that oxygen etching decreased platelet adhesion, activation and aggregation as well as reduced the clotting of whole blood on the surface. Similar protein adsorption between the control and treated substrates suggests the improved oxide layer inhibits denaturization of adsorbed proteins. This study demonstrated the ability of ion bombardment to alter the surface chemistry of a substrate for beneficial applications.

The use of low energy helium ion bombardment was also investigated for applications in the generation of biomedically relevant surfaces. Helium plasma immersion was used to create a micro- porous surface on Ti6Al4V titanium alloy. It was found that pore size could be controlled with changes in processing temperature. A week-long cell culture showed the etching had no detrimental effects and could possibly increase osteoblast activity. These surfaces also have potential application in securing biomedical coatings such as hydroxyapatite or serving as a carrier for targeted drug delivery. This again demonstrates the ability of ion etching to create unique and controllable topographies.

Finally, the use of helium texturization of aluminum alloys was investigated. This work represents the first comprehensive characterization of low energy helium ion feature formation on aluminum surfaces. It was observed that low energy irradiation was capable of forming complex surface features, including: nodules, holes, and bubbles. At sufficiently high ion energies, a nano-structuring "fuzz" was also observed. Feature size was directly related to the substrate temperature, with high temperatures resulting in larger features. Trends observed on the 6061 alloy could be applied to the 2024 alloy when referenced to the absolute melting temperature, suggesting these results could be extensible to additional aluminum alloys or other materials entirely. The knowledge gained from this characterization was then used to develop aluminum surfaces with a lotus-like surface topography. This resulted not in a decrease, but an increase in water wettability, and hence, the icing nature of the aluminum was not affected by the addition of these surface features. However, this work demonstrated the controllability of self assembly and patterning on aluminum surfaces under low energy helium ion irradiation. Additionally, the ability to create superhydrophilic surfaces could be useful in a number of industrial applications.

This entirety of this work represents only a limited assessment of the patterning capabilities of ion texturization. It appears that the most important factors impacting the formation of features are the ion species and substrate temperature. Titanium irradiation with argon and helium ions resulted in dramatically different structuring of the surfaces. Argon (the much larger ion) simply etched the surface while helium was able to penetrate the material and form a porous structure. Oxygen ions reacted with titanium to form an oxide, again altering the evolution of the surface in a unique manner. Substrate temperature was also a determining factor in the creation of these surfaces. Generally, the increased diffusion allowed by higher temperatures resulted in a more dramatic restructuring of the surface and larger features. It was shown that through controlling variables such as ion species, ion energy and substrate temperature, the patterning of the surfaces could be controlled. By continuing to develop an understanding of these interactions, ion etching could become an effective method for patterning on next generation materials.

9.2 Future Work

9.2.1 Ion Beam Etching Titanium for Enhanced Osteoblast Response

The normal ion etching of titanium yielded only modest improvements in biological response. It was observed that the micro-structure evolution of the titanium was dependant on the uneven etching of the individual grains. Future work could be directed at optimizing titanium pretreatment to obtain different grain sizes. This would then result in different feature sizes on the micro-scale after etching. Similarly, by changing substrate temperatures during etching and increasing material diffusion it may be possible to influence the relative size and spacing between the nano-ripples generated on the surface. Changes to either of these features

could lead to improvements in cellular response. It would also be interesting to pursue plasma immersion processing for the treatment of three dimensional objects such as dental implants or bone screws.

9.2.2 Improved Thrombogenicity on Oxygen Etched Titanium Surfaces

Results on the oxygen etched titanium surfaces were promising for reducing the activation of blood components and inhibiting thrombus formation. Future studies could be directed towards further characterization of the oxide layer formed by the oblique etching (oxide thickness, rutile vs. anatase composition, etc.). It was also hypothesized that the improved surface is a result of a reduction in protein denaturing from the improved oxide. To investigate this, a protein conformation study should be pursued to determine if this is truly the source of the enhanced response. Finally, it would be interesting to determine if angle etching is truly necessary or if normal incidence etching is capable of achieving the same results. For this, a study looking at the effects of varying the angle of incidence as well as ion energy on the formation of the oxide would be necessary. Similar blood component activation studies on these surfaces could also help elucidate the exact mechanisms responsible for improved compatibility.

9.2.3 Ion Etching for Sharp Tip Features on Titanium and the Response of Cells to these Surfaces

Cell morphology was dramatically affected by the needle like features created on titanium by oblique angle ion etching. Cells on the 30° etched surface showed reduced spreading. It would be of interest to measure the adhesion strength of the cells to evaluate if the cells are more easily removed from these surfaces than an untreated surface. This could be evaluated by constructing

a chamber to expose celled surfaces to a shearing fluid flow and increasing the flow until cells are removed. This would evaluate the surfaces for use on stents, where the force of blood flow may be adequate to remove cells and prevent fouling. The 75° etched surface was also of interest, as it displayed the ability to preferentially align cells. Further studies could be performed to evaluate the reactions of different cell types (osteoblasts, fibroblasts, etc.) on these surfaces focusing specifically on cells related to tissues showing preferential alignment in the body such as bone and muscle. These surfaces could then be considered on scaffolding for growing replacement tissue *in vitro* that would later be implanted to replace damaged tissue *in vivo*.

9.2.4 Low Energy Helium Ion Texturization of Titanium and Relevance to Biomedical Applications

The porous nature of the surfaces created by the helium etching makes them potentially well suited for bioactive coatings. Most bioactive coatings such as hydroxyapatite rely on mechanical interactions to adhere themselves to a surface. Deposition on a porous surface could result in complex mechanical interlocking, better securing the coating to the implant. Future studies could be directing at evaluating the adhesion of biomedically relevant coatings to these porous surfaces. Also, targeted drug delivery is of particular interest for administering antibiotics or pain medication locally at the implant. Evaluation of drug eluting properties from these porous surfaces would be an area for further research.

9.2.5 Helium Etching to Create Aluminum Nanostructures and their Relevance to Ice Phobic Surfaces

The field of structure formation resulting from low energy helium irradiation remains largely unexplored. Aluminum alloys characterization is only one step; many more materials must be evaluated before the mechanisms of formation can be fully understood. Future studies could be performed using a similar approach to that completed in this work, but on other widely used materials such as steel, titanium, etc. Also, a novel theory was put forward about the driving forces responsible for feature development on these surfaces. The ion-induced polarization of helium ion etched surfaces and subsequent response to electric fields should be evaluated. One potential way to do this would be to irradiate substrates under the same conditions (temperature, ion flux, ion fluence, etc.) with a directed ion beam rather than a plasma immersion method. This reduces electric field at the substrate surface to near zero values. If feature evolution is the same as the plasma immersed conditions, the hypothesis is disproven. However, if no surface structures are observed or greatly differ, then polarization effects are likely a contributing factor. Finally, the lotus-like structures that were developed were shown to be extremely hydrophilic. This was a result of the increased surface area and the natural hydrophilic affinity of aluminum. It has been shown that when texturized surfaces such as this are then coating with a slightly hydrophobic material, the surface will transition from superhydrophilic to superhydrophobic properties. Therefore, future work could be directing to develop coatings and coating processes to make superhydrophobic surfaces using these surfaces.

10 **References**

[1] S. Facsko, T. Dekorsy, C. Koerdt, C. Trappe, H. Kurz, A. Vogt, H.L. Hartnagel, Science, 285 (1999) 1551-1553.

[2] Q.M. Wei, X.L. Zhou, B. Joshi, Y.B. Chen, K.D. Li, Q.H. Wei, K. Sun, L.M. Wang, Adv Mater, 21 (2009) 2865.

[3] B. Ziberi, M. Cornejo, F. Frost, B. Rauschenbach, Journal of Physics-Condensed Matter, 21 (2009) .

[4] S. Kim, Arthritis Rheum, 59 (2008) 481-488.

[5] T.K. Fehring, S. Odum, W.L. Griffin, J.B. Mason, M. Nadaud, Clin Orthop Relat Res, (2001) 315-318.

[6] L. Linder, A. Carlsson, L. Marsal, L.M. Bjursten, P.I. Branemark, J Bone Joint Surg Br, 70 (1988) 550-555.

[7] P.I. Branemark, B.O. Hansson, R. Adell, U. Breine, J. Lindstrom, O. Hallen, A. Ohman, Scand J Plast Reconstr Surg Suppl, 16 (1977) 1-132.

[8] P.F. Sharkey, W.J. Hozack, R.H. Rothman, S. Shastri, S.M. Jacoby, Clin Orthop Relat Res, (2002) 7-13.

[9] H. Schliephake, D. Scharnweber, M. Dard, A. Sewing, A. Aref, S. Roessler, J Biomed Mater Res B, 73B (2005) 88-96.

[10] D.M. Ferris, G.D. Moodie, P.M. Dimond, C.W. Gioranni, M.G. Ehrlich, R.F. Valentini, Biomaterials, 20 (1999) 2323-2331.

[11] J. Dumbleton, M.T. Manley, J Bone Joint Surg Am, 86-A (2004) 2526-2540.

[12] F. Barrere, C.A. van Blitterswijk, K. de Groot, Int J Nanomedicine, 1 (2006) 317-332.

[13] G. Mendonca, D.B. Mendonca, F.J. Aragao, L.F. Cooper, Biomaterials, 29 (2008) 3822-3835.

[14] R. Branemark, L. Emanuelsson, A. Palmquist, P. Thomsen, Nanomedicine, 7 (2011) 220-227.

[15] K. Anselme, P. Davidson, A.M. Popa, M. Giazzon, M. Liley, L. Ploux, Acta Biomater, 6 (2010) 3824-3846.

[16] M.J. Dalby, D. McCloy, M. Robertson, H. Agheli, D. Sutherland, S. Affrossman, R.O. Oreffo, Biomaterials, 27 (2006) 2980-2987.

[17] R.L. Price, K.M. Haberstroh, T.J. Webster, Med Biol Eng Comput, 41 (2003) 372-375.

[18] D. Rekow, P. Van Thompson, J.L. Ricci, J Mater Sci, 41 (2006) 5113-5121.

[19] P. Colombo, C. Vakifahmetoglu, S. Costacurta, J Mater Sci, 45 (2010) 5425-5455.

[20] K. Anselme, M. Bigerelle, Acta Biomater, 1 (2005) 211-222.

[21] T.J. Webster, R.W. Siegel, R. Bizios, Biomaterials, 20 (1999) 1221-1227.

[22] J.I. Rosales-Leal, M.A. Rodriguez-Valverde, G. Mazzaglia, P.J. Ramon-Torregrosa, L. Diaz-Rodriguez, O. Garcia-Martinez, M. Vallecillo-Capilla, C. Ruiz, M.A. Cabrerizo-Vilchez, Colloid Surface A, 365 (2010) 222-229.

[23] G. Wang, X. Liu, H. Zreiqat, C. Ding, Colloids Surf B Biointerfaces, (2011).

[24] G. Zhao, A.L. Raines, M. Wieland, Z. Schwartz, B.D. Boyan, Biomaterials, 28 (2007) 2821-2829.

[25] M.J. Dalby, N. Gadegaard, R. Tare, A. Andar, M.O. Riehle, P. Herzyk, C.D. Wilkinson, R.O. Oreffo, Nat Mater, 6 (2007) 997-1003.

[26] P. Hanarp, D.S. Sutherland, J. Gold, B. Kasemo, Colloid Surface A, 214 (2003) 23-36.

[27] C. Vieu, F. Carcenac, A. Pepin, Y. Chen, M. Mejias, A. Lebib, L. Manin-Ferlazzo, L. Couraud, H. Launois, Appl Surf Sci, 164 (2000) 111-117.

[28] H. Morimoto, Y. Sasaki, K. Saitoh, Y. Watakabe, T. Kato, Microelectron Eng, 4 (1986) 163-179.

[29] J. Gan, H. Chen, F. Zhou, H. Huang, J. Zheng, W. Song, L. Yuan, Z. Wu, Colloids Surf B Biointerfaces, 76 (2010) 381-385.

[30] F. Romanato, M. Tormen, L. Businaro, L. Vaccari, T. Stomeo, A. Passaseo, E. Di Fabrizio, Microelectron Eng, 73-74 (2004) 870-875.

[31] R.D. Piner, J. Zhu, F. Xu, S. Hong, C.A. Mirkin, Science, 283 (1999) 661-663.

[32] W.J. Li, C.T. Laurencin, E.J. Caterson, R.S. Tuan, F.K. Ko, Journal of Biomedical Materials Research, 60 (2002) 613-621.

[33] F.L. Zhou, R.H. Gong, I. Porat, J Mater Sci, 44 (2009) 5501-5508.

[34] K.C. Popat, L. Leoni, C.A. Grimes, T.A. Desai, Biomaterials, 28 (2007) 3188-3197.

[35] J.M. Courtney, N.M.K. Lamba, S. Sundaram, C.D. Forbes, Biomaterials, 15 (1994) 737-744.

[36] B.D. Ratner, Biomaterials, 28 (2007) 5144-5147.

[37] J.Y. Chen, L.P. Wang, K.Y. Fu, N. Huang, Y. Leng, Y.X. Leng, P. Yang, J. Wang, G.J. Wan, H. Sun, X.B. Tian, P.K. Chu, Surf Coat Tech, 156 (2002) 289-294.

[38] K.R. Lee, R.K. Roy, H.W. Choi, J.W. Yi, M.W. Moon, D.K. Han, J.H. Shin, A. Kamijo, T. Hasebe, Acta Biomater, 5 (2009) 249-256.

[39] A. Mochizuki, T. Ogawa, K. Okamoto, T. Nakatani, Y. Nitta, Mat Sci Eng C-Mater, 31 (2011) 567-573.

[40] N. Huang, Y.J. Weng, Q.A. Song, Y.J. Zhou, L.P. Zhang, J. Wang, J.Y. Chen, Y.X. Leng, S.Y. Li, Biomaterials, 32 (2011) 1253-1263.

[41] M.E. Meyerhoff, M.C. Frost, M.M. Reynolds, Biomaterials, 26 (2005) 1685-1693.

[42] C.J. Lin, Y. Yang, Y.K. Lai, Q.Q. Zhang, K. Wu, L.H. Zhang, P.F. Tang, Colloid Surface B, 79 (2010) 309-313.

[43] T.L. Sun, H. Tan, D. Han, Q. Fu, L. Jiang, Small, 1 (2005) 959-963.

[44] D. Han, L. Chen, L. Jiang, Colloid Surface B, 85 (2011) 2-7.

[45] C. Mao, X.M. Hou, X.B. Wang, Q.S. Zhu, J.C. Bao, L.C. Jiang, J.A. Shen, Colloid Surface B, 80 (2010) 247-250.

[46] I. Tsyganov, M.F. Maitz, E. Wieser, Appl Surf Sci, 235 (2004) 156-163.

[47] F. Zhang, X.H. Liu, Y.J. Mao, N. Huang, Y. Chen, Z.H. Zheng, Z.Y. Zhou, A.Q. Chen, Z.B. Jiang, Surf Coat Tech, 104 (1998) 146-150.

[48] H. Nan, Y. Ping, C. Xuan, L. Yongxang, Z. Xiaolan, C. Guangjun, Z. Zihong, Z. Feng, C. Yuanru, L. Xianghuai, X. Tingfei, Biomaterials, 19 (1998) 771-776.

[49] M.F. Maitz, M.T. Pham, E. Wieser, Journal of Biomaterials Applications, 17 (2003) 303-319.

[50] J.Y. Chen, Y.X. Leng, X.B. Tian, L.P. Wang, N. Huang, P.K. Chu, P. Yang, Biomaterials, 23 (2002) 2545-2552.

[51] N. Huang, P. Yang, Y.X. Leng, J.Y. Chen, H. Sun, J. Wang, G.J. Wang, P.D. Ding, T.F. Xi, Y. Leng, Biomaterials, 24 (2003) 2177-2187.

[52] D.H. Kim, H.E. Kim, K.R. Lee, C.N. Whang, I.S. Lee, Mat Sci Eng C-Bio S, 22 (2002) 9-14.

[53] D. Nishijima, M.Y. Ye, N. Ohno, S. Takamura, J Nucl Mater, 329-33 (2004) 1029-1033.

[54] S. Nagata, B. Tsuchiya, T. Sugawara, N. Ohtsu, O.T. Shikama, J Nucl Mater, 307 (2002) 1513-1516.

[55] N. Yoshida, H. Iwakiri, K. Tokunaga, T. Baba, J Nucl Mater, 337-39 (2005) 946-950.

[56] D. Nishijima, M.Y. Ye, N. Ohno, S. Takamura, J Nucl Mater, 313 (2003) 97-101.

[57] A. Ebihara, M. Tokitani, K. Tokunaga, T. Fujiwara, A. Sagara, N. Yoshida, J Nucl Mater, 363 (2007) 1195-1200.

[58] E. Abramov, G. Solovioff, D. Eliezer, J Nucl Mater, 215 (1994) 1406-1410.

[59] E. Abramov, D. Moreno, G. Solovioff, D. Eliezer, J Nucl Mater, 215 (1994) 1390-1395.

[60] S. Kajita, T. Saeki, Y. Hirahata, N. Ohno, Jpn J Appl Phys, 50 (2011) -.

[61] K. Morishita, T. Inoue, N. Yoshida, J Nucl Mater, 269 (1999) 997-1002.

[62] T. Kawakami, K. Tokunaga, N. Yoshida, Fusion Eng Des, 81 (2006) 335-340.

[63] R. Behrisch, J Nucl Mater, 85-6 (1979) 1047-1061.

[64] B. Glam, D. Moreno, S. Eliezer, D. Eliezer, J Nucl Mater, 393 (2009) 230-234.

[65] S. Furuno, K. Hojou, K. Izui, N. Kamigaki, T. Kino, J Nucl Mater, 155 (1988) 1149-1153.

[66] W.D. Wilson, C.L. Bisson, M.I. Baskes, Phys Rev B, 24 (1981) 5616-5624.

[67] J.B. Adams, W.G. Wolfer, J Nucl Mater, 166 (1989) 235-242.

[68] M.J. Puska, R.M. Nieminen, Phys Rev B, 29 (1984) 5382-5397.

[69] B.Y. Ao, J.Y. Yang, X.L. Wang, W.Y. Hu, J Nucl Mater, 350 (2006) 83-88.

[70] L. Yang, X.T. Zu, F. Gao, Physica B, 403 (2008) 2719-2724.

[71] K. Morishita, R. Sugano, B.D. Wirth, T.D. de la Rubia, Nucl Instrum Meth B, 202 (2003) 76-81.

[72] A.A. Lucas, Physica B & C, 127 (1984) 225-239.

[73] G.P. Tiwari, J. Singh, J Nucl Mater, 172 (1990) 114-122.

[74] B. Glam, S. Eliezer, D. Moreno, D. Eliezer, J Nucl Mater, 392 (2009) 413-419.

[75] M.J. Baldwin, R.P. Doerner, J Nucl Mater, 404 (2010) 165-173.

[76] S. Kajita, W. Sakaguchi, N. Ohno, N. Yoshida, T. Saeki, Nucl Fusion, 49 (2009) -.

[77] M.J. Baldwin, R.P. Doerner, Nucl Fusion, 48 (2008) -.

[78] W. Sakaguchi, S. Kajita, N. Ohno, M. Takagi, J Nucl Mater, 390-91 (2009) 1149-1152.

[79] S. Kajita, S. Takamura, N. Ohno, D. Nishijima, H. Iwakiri, N. Yoshida, Nucl Fusion, 47 (2007) 1358-1366.

[80] K. Tokunaga, S. Tamura, N. Yoshida, K. Ezato, M. Taniguchi, K. Sato, S. Suzuki, M. Akiba, J Nucl Mater, 329-33 (2004) 757-760.

[81] M.J. Baldwin, R.P. Doerner, D. Nishijima, K. Tokunaga, Y. Ueda, J Nucl Mater, 390-91 (2009) 886-890.

[82] W. Sakaguchi, S. Kajita, N. Ohno, M. Takagi, H. Kurishita, Plasma and Fusion Research, 5 (2010).

[83] I.A. Ryzhkin, V.F. Petrenko, J Phys Chem B, 101 (1997) 6267-6270.

[84] A. Dotan, H. Dodiuk, C. Laforte, S. Kenig, J Adhes Sci Technol, 23 (2009) 1907-1915.

[85] R.N. Wenzel, Ind Eng Chem, 28 (1936) 988-994.

[86] A.B.D. Cassie, S. Baxter, T Faraday Soc, 40 (1944) 0546-0550.

[87] T.L. Sun, L. Feng, X.F. Gao, L. Jiang, Accounts Chem Res, 38 (2005) 644-652.

[88] M.J. Liu, Y.M. Zheng, J. Zhai, L. Jiang, Accounts Chem Res, 43 (2010) 368-377.

[89] W. Barthlott, C. Neinhuis, Planta, 202 (1997) 1-8.

[90] Y.M. Zheng, X.F. Gao, L. Jiang, Soft Matter, 3 (2007) 178-182.

[91] Y. Ding, S. Xu, Y. Zhang, A.C. Wang, M.H. Wang, Y.H. Xiu, C.P. Wong, Z.L. Wang, Nanotechnology, 19 (2008) -.

[92] P.P. Goodwyn, Y. Maezono, N. Hosoda, K. Fujisaki, Naturwissenschaften, 96 (2009) 781-787.

[93] T. Wagner, C. Neinhuis, W. Barthlott, Acta Zool-Stockholm, 77 (1996) 213-225.

[94] Y. Lee, Y. Yoo, J. Kim, S. Widhiarini, B. Park, H.C. Park, K.J. Yoon, D. Byun, J Bionic Eng, 6 (2009) 365-370.

[95] D. Byun, J. Hong, Saputra, J.H. Ko, Y.J. Lee, H.C. Park, B.K. Byun, J.R. Lukes, J Bionic Eng, 6 (2009) 63-70.

[96] E. Bormashenko, Y. Bormashenko, T. Stein, G. Whyman, E. Bormashenko, J Colloid Interf Sci, 311 (2007) 212-216.

[97] X.F. Gao, L. Jiang, Nature, 432 (2004) 36-36.

[98] M. Morra, E. Occhiello, F. Garbassi, Langmuir, 5 (1989) 872-876.

[99] K.K.S. Lau, J. Bico, K.B.K. Teo, M. Chhowalla, G.A.J. Amaratunga, W.I. Milne, G.H. McKinley, K.K. Gleason, Nano Lett, 3 (2003) 1701-1705.

[100] L. Feng, S.H. Li, H.J. Li, J. Zhai, Y.L. Song, L. Jiang, D.B. Zhu, Angew Chem Int Edit, 41 (2002) 1221-+.

[101] E. Occhiello, M. Morra, G. Morini, F. Garbassi, P. Humphrey, J Appl Polym Sci, 42 (1991) 551-559.

[102] H.Y. Erbil, A.L. Demirel, Y. Avci, O. Mert, Science, 299 (2003) 1377-1380.

[103] Y.Y. Yan, N. Gao, W. Barthlott, Adv Colloid Interfac, 169 (2011) 80-105.

[104] Z.G. Guo, W.M. Liu, B.L. Su, J Colloid Interf Sci, 353 (2011) 335-355.

[105] M.L. Ma, R.M. Hill, Curr Opin Colloid In, 11 (2006) 193-202.

[106] A.J. Meuler, J.D. Smith, K.K. Varanasi, J.M. Mabry, G.H. McKiney, R.E. Cohen, Acs Appl Mater Inter, 2 (2010) 3100-3110.

[107] R. Menini, M. Farzaneh, Surf Coat Tech, 203 (2009) 1941-1946.

[108] R. Jafari, R. Menini, M. Farzaneh, Appl Surf Sci, 257 (2010) 1540-1543.

[109] D.K. Sarkar, M. Farzaneh, J Adhes Sci Technol, 23 (2009) 1215-1237.

[110] S.A. Kulinich, M. Farzaneh, Appl Surf Sci, 255 (2009) 8153-8157.

[111] S. Farhadi, M. Farzaneh, S.A. Kulinich, Appl Surf Sci, 257 (2011) 6264-6269.

[112] L.L. Cao, A.K. Jones, V.K. Sikka, J.Z. Wu, D. Gao, Langmuir, 25 (2009) 12444-12448.

[113] M. Zou, S. Beckford, R. Wei, C. Ellis, G. Hatton, M.A. Miller, Appl Surf Sci, 257 (2011) 3786-3792.

[114] K.K. Varanasi, T. Deng, J.D. Smith, M. Hsu, N. Bhate, Appl Phys Lett, 97 (2010) .

[115] M.L. Malhotra, Metallography, 10 (1977) 337-347.

[116] R. Reiche, W. Hauffe, Appl Surf Sci, 165 (2000) 279-287.

[117] F. Frost, A. Schindler, F. Bigl, Phys Rev Lett, 85 (2000) 4116-4119.

[118] A. Toma, F.B. de Mongeot, R. Buzio, G. Firpo, S.R. Bhattacharyya, C. Boragno, U. Valbusa, Nucl Instrum Meth B, 230 (2005) 551-554.

[119] S.S. Makh, R. Smith, J.M. Walls, J Mater Sci, 17 (1982) 1689-1699.

[120] J. Pelletier, A. Anders, IEEE T Plasma Sci, 33 (2005) 1944-1959.

[121] Y. Yamamura, H. Tawara, Atom Data Nucl Data, 62 (1996) 149-253.

[122] B.S. Batic, M. Jenko, Journal of Vacuum Science & Technology A, 28 (2010) 741-744.

[123] S. Rusponi, G. Costantini, C. Boragno, U. Valbusa, Phys Rev Lett, 81 (1998) 4184-4187.

[124] S. Rusponi, C. Boragno, U. Valbusa, Phys Rev Lett, 78 (1997) 2795-2798.

[125] R.M. Bradley, J.M.E. Harper, J Vac Sci Technol A, 6 (1988) 2390-2395.

[126] H.C. Anderson, Curr Rheumatol Rep, 5 (2003) 222-226.

[127] B.D. Boyan, Z. Schwartz, L.D. Swain, Bone Miner, 17 (1992) 263-268.

[128] H. Shin, K. Zygourakis, M.C. Farach-Carson, M.J. Yaszemski, A.G. Mikos, J Biomed Mater Res A, 69 (2004) 535-543.

[129] G.N. Bancroft, V.I. Sikavitsas, J. van den Dolder, T.L. Sheffield, C.G. Ambrose, J.A. Jansen, A.G. Mikos, Proc Natl Acad Sci U S A, 99 (2002) 12600-12605.

[130] M. Rinner, J. Gerlach, W. Ensinger, Surf Coat Tech, 132 (2000) 111-116.

[131] C.-H. Yang, Y.-T. Wang, W.-F. Tsai, C.-F. Ai, M.-C. Lin, H.-H. Huang, Clinical Oral Implants Research, (2011) .

[132] G. Thorwarth, S. Mandl, B. Rauschenbach, Surf Coat Tech, 136 (2001) 236-240.

[133] Z.W. Kowalski, J Mater Sci, 19 (1984) 2845-2854.

[134] D. Ghose, P. Karmakar, Nucl Instrum Meth B, 230 (2005) 539-544.

[135] F. Shen, E. Zhang, Z.J. Wei, Mat Sci Eng C-Mater, 30 (2010) 369-375.

[136] S. Takemoto, T. Yamamoto, K. Tsuru, S. Hayakawa, A. Osaka, S. Takashima, Biomaterials, 25 (2004) 3485-3492.

[137] K.E. Healy, P. Ducheyne, Journal of Biomedical Materials Research, 26 (1992) 319-338.

[138] W. Gopel, J.A. Anderson, D. Frankel, M. Jaehnig, K. Phillips, J.A. Schafer, G. Rocker, Surf Sci, 139 (1984) 333-346.

[139] J.M. Anderson, A. Rodriguez, D.T. Chang, Semin Immunol, 20 (2008) 86-100.

[140] L. Tang, J.W. Eaton, Mol Med, 5 (1999) 351-358.

[141] C.J. Wilson, R.E. Clegg, D.I. Leavesley, M.J. Pearcy, Tissue Eng, 11 (2005) 1-18.

[142] M.C. Sunny, C.P. Sharma, J Biomater Appl, 6 (1991) 89-98.

[143] N.A. Riedel, J.D. Williams, K.C. Popat, J Mater Sci, 46 (2011) 6087-6095.

[144] A.K. Sen, D. Ghose, J Mater Sci, 28 (1993) 1525-1531.

[145] Z.W. Kowalski, J Mater Sci, 20 (1985) 1521-1555.

[146] C.H. Choi, S.H. Hagvall, B.M. Wu, J.C.Y. Dunn, R.E. Beygui, C.J. Kim, Biomaterials, 28 (2007) 1672-1679.

[147] L.Z. Zhao, L.S. Hu, K.F. Huo, Y.M. Zhang, Z.F. Wu, P.K. Chu, Biomaterials, 31 (2010) 8341-8349.

[148] J.Y. Lee, B.S. Kang, B. Hicks, T.F. Chancellor, B.H. Chu, H.T. Wang, B.G. Keselowsky, F. Ren, T.P. Lele, Biomaterials, 29 (2008) 3743-3749.

[149] P.B. Johnson, P.W. Gilberd, A. Markwitz, W.J. Trompetter, G.A. Collins, K.T. Short, D.D. Cohen, N. Dytlewski, Surf Coat Tech, 136 (2001) 217-222.

[150] S.H. Chen, G. Schumacher, Z.Y. Xu, M. Richter, J Nucl Mater, 358 (2006) 26-34.

[151] A. Markwitz, P.B. Johnson, P.W. Gilberd, G.A. Collins, Nucl Instrum Meth B, 190 (2002) 718-722.

[152] A. Markwitz, P.B. Johnson, P.W. Gilberd, G.A. Collins, D.D. Cohen, N. Dytlewski, Nucl Instrum Meth B, 161 (2000) 1048-1053.

[153] J.L. Li, X.X. Ma, M.R. Sun, Z.L. Song, Nucl Instrum Meth B, 267 (2009) 482-486.

[154] Z. Gao, Y.Z. Gao, Y.H. Li, T.S. Zhang, Y. Li, Nanostruct Mater, 11 (1999) 867-872.

[155] P.B. Johnson, V.J. Kennedy, A. Markwitz, Curr Appl Phys, 6 (2006) 327-330.

[156] D. Rosenberg, G.K. Wehner, J Appl Phys, 33 (1962) 1842-&.

[157] A. Marmur, Langmuir, 24 (2008) 7573-7579.

[158] M. Okada, Y. Murata, Surf Sci, 311 (1994) 257-262.

[159] Z. Vager, D.S. Gemmell, Phys Rev Lett, 37 (1976) 1352-1354.

[160] R.A. Mccorkle, J.L. Cox, Phys Lett A, 87 (1982) 149-151.

[161] E. Fermi, Phys Rev, 57 (1940) 485-493.

[162] T. Hofman, J. Mazur, J. Nikliborc, J. Rafalowicz, British Journal of Applied Physics, 12 (1961) 342.

[163] J.E. Morris, Metallography, 5 (1972) 41-58.

[164] K.L. Chopra, J Appl Phys, 37 (1966) 2249.

[165] L.B. Kish, P. Chaoguang, J. Ederth, W.H. Marlow, C.G. Granqvist, S.J. Savage, Surf Coat Tech, 142 (2001) 1088-1093.

[166] K. Mihama, M. Tanaka, Journal of Crystal Growth, 2 (1968) 51-53.

[167] Y. Murayama, Thin Solid Films, 12 (1972) 287-&.

[168] N. Parkansky, B. Alterkop, S. Goldsmith, R.L. Boxman, H. Wulff, M. Quaas, A. Quade, Thin Solid Films, 377 (2000) 507-511.

[169] C. Bower, W. Zhu, S.H. Jin, O. Zhou, Appl Phys Lett, 77 (2000) 830-832.

[170] H. Kashani, J Mater Sci, 30 (1995) 6090-6096.

11 Appendix A

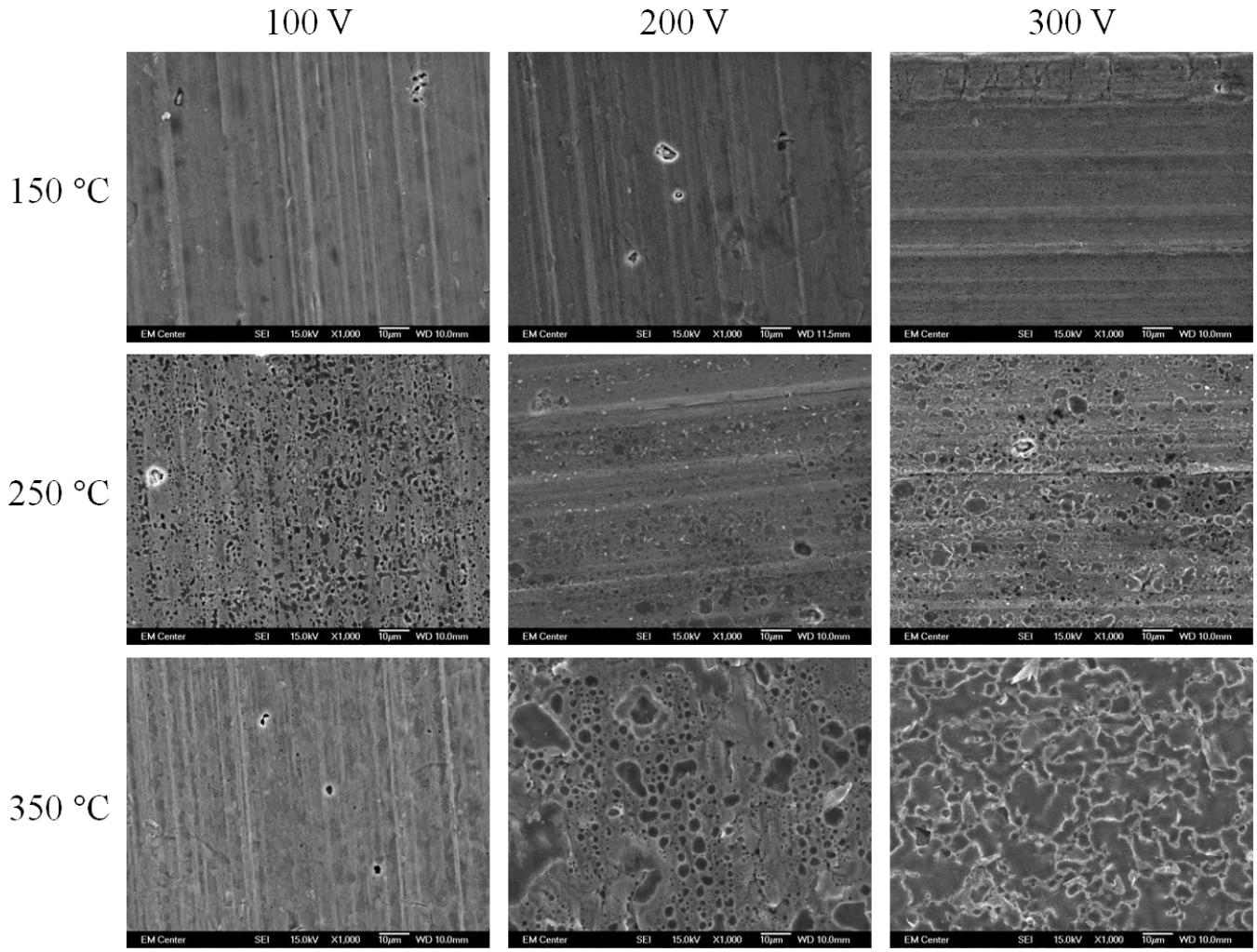

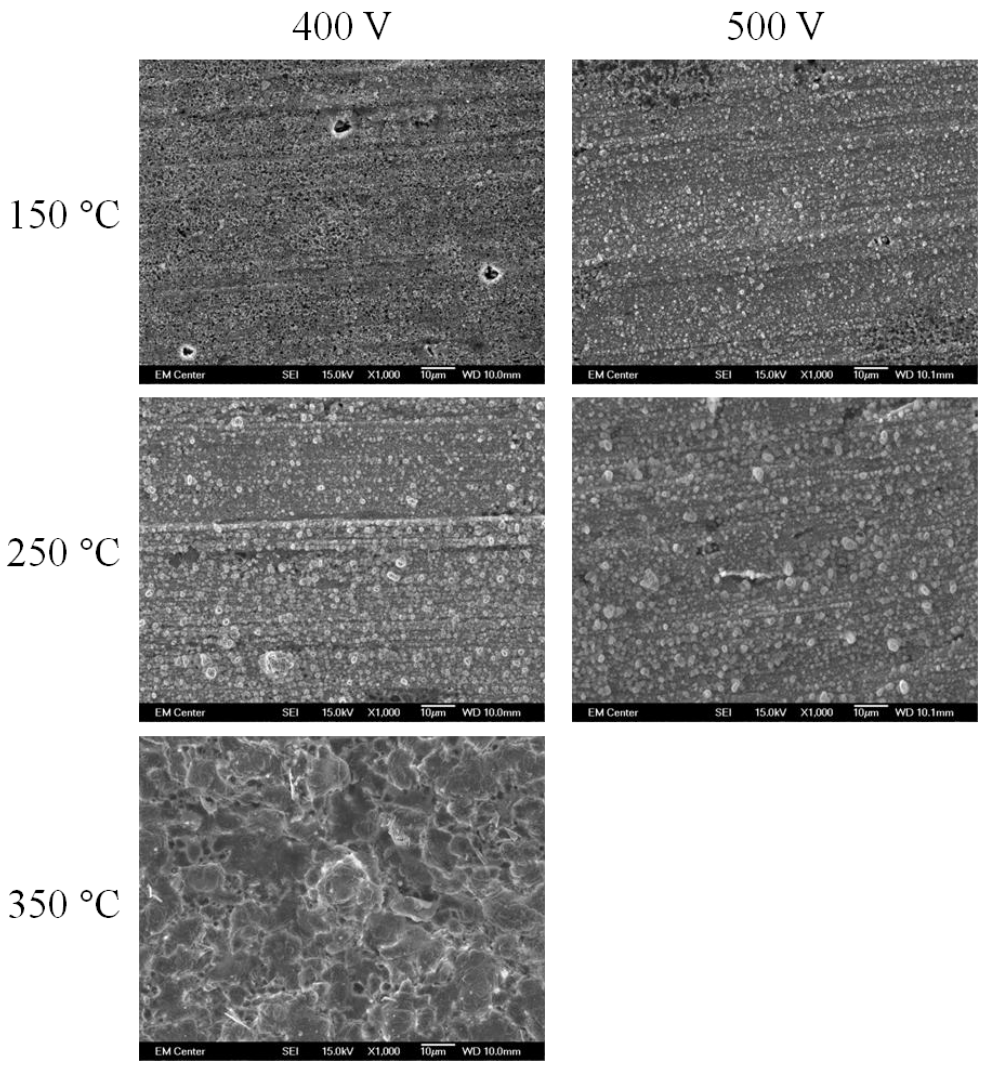
400 V
500 V
150 °C
250 °C
350 °C
EM Center SEI 15.0kV X1,000 10μm WD 10.0mm
EM Center SEI 15.0kV X1,000 10μm WD 10.1mm
EM Center SEI 15.0kV X1,000 10μm WD 10.1mm
EM Center SEI 15.0kV X1,000 10μm WD 10.0mm
EM Center SEI 15.0kV X1,000 10μm WD 10.0mm

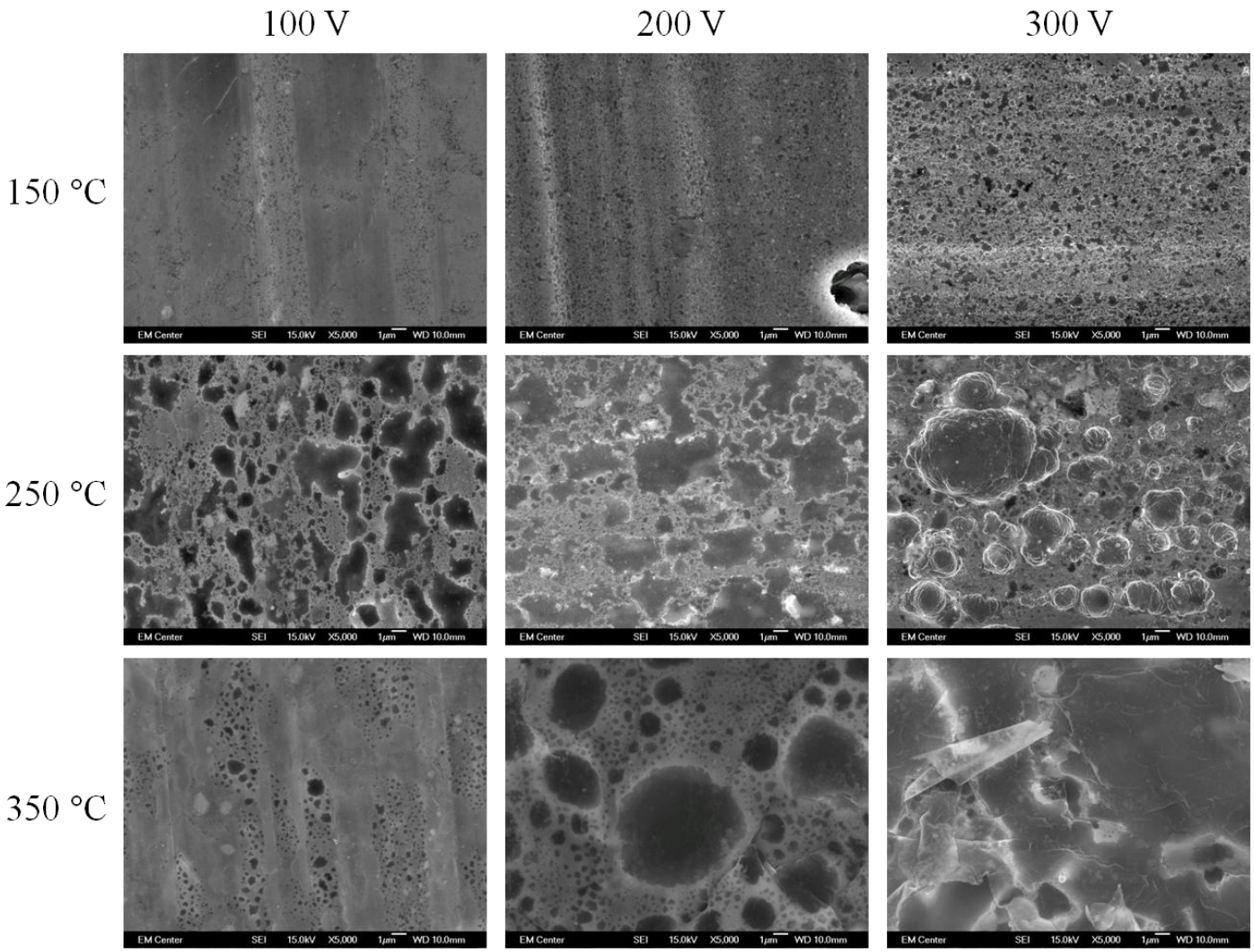
100 V
200 V
300 V
150 °C
250 °C
350 °C
EM Center SEI 15.0kV X5,000 1μm WD 10.0mm

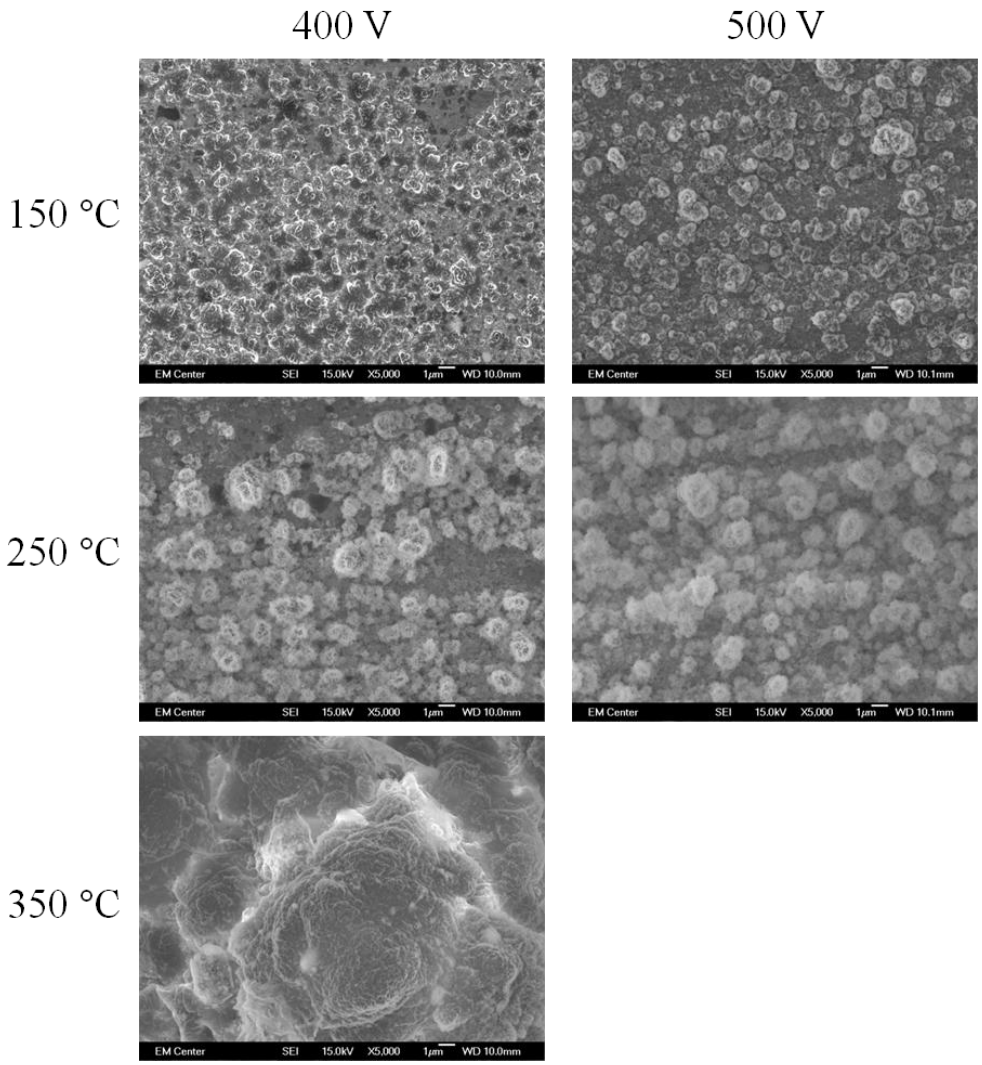
400 V
500 V
150 °C
250 °C
350 °C
EM Center SEI 15.0kV X5,000 1μm WD 10.0mm
EM Center SEI 15.0kV X5,000 1μm WD 10.1mm
EM Center SEI 15.0kV X5,000 1μm WD 10.1mm
EM Center SEI 15.0kV X5,000 1μm WD 10.0mm

12 Appendix B

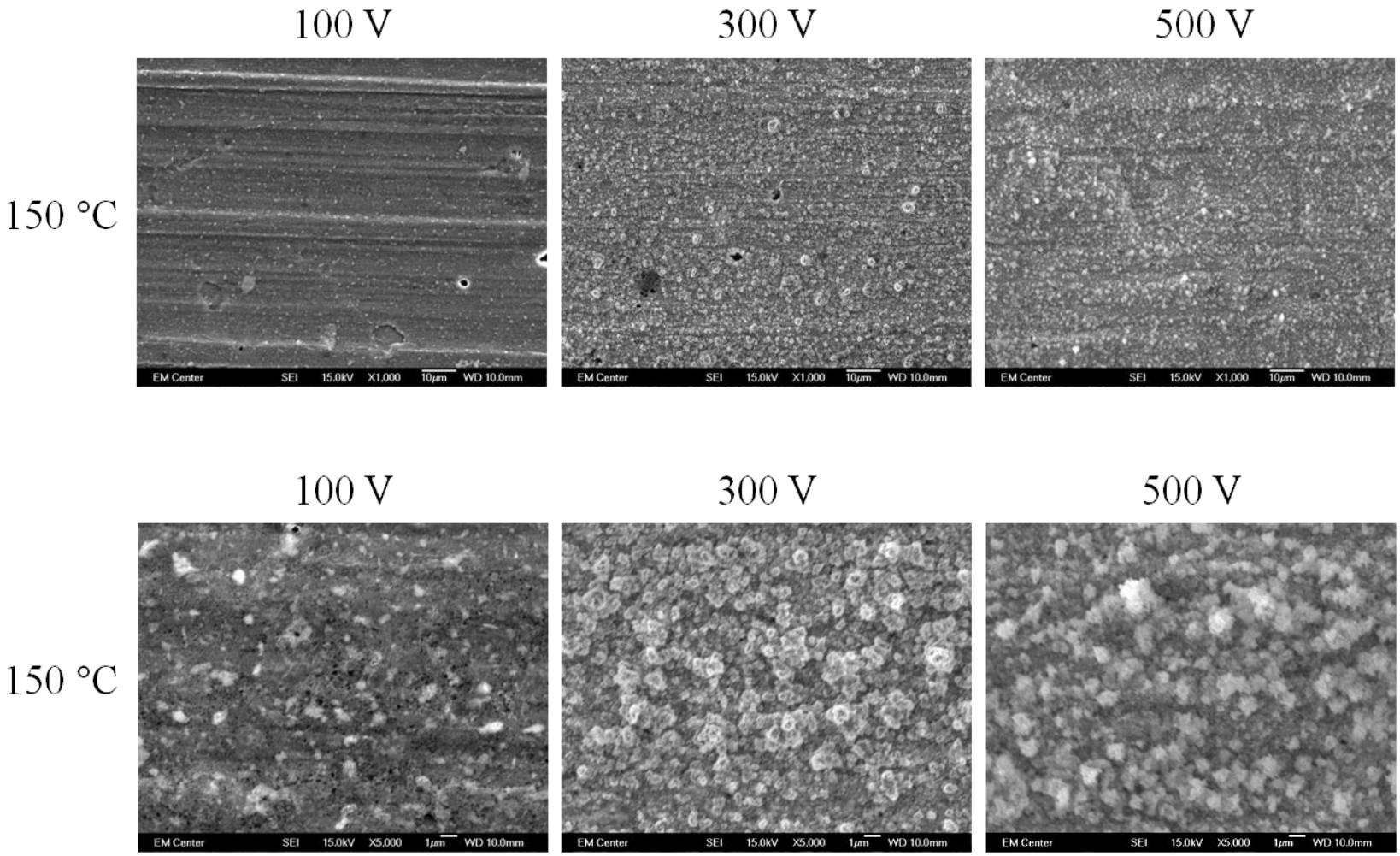

100 V

200 V

300 V

250 °C

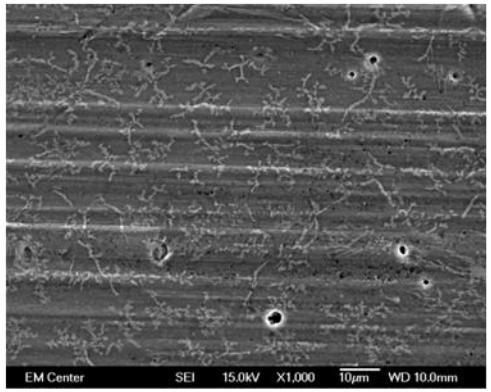

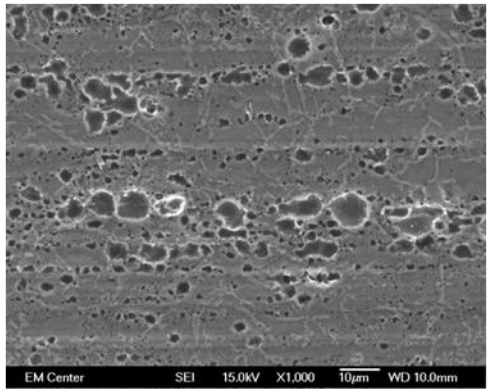

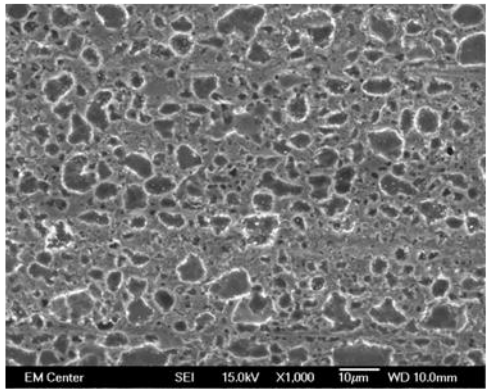

400 V

500 V

250 °C

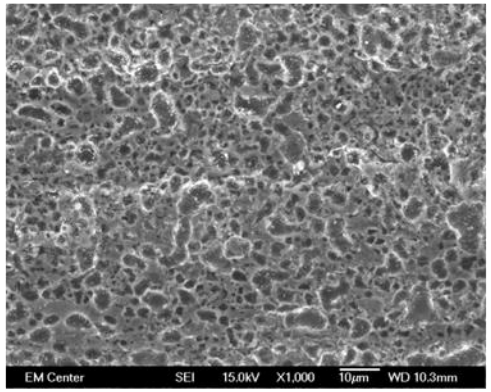

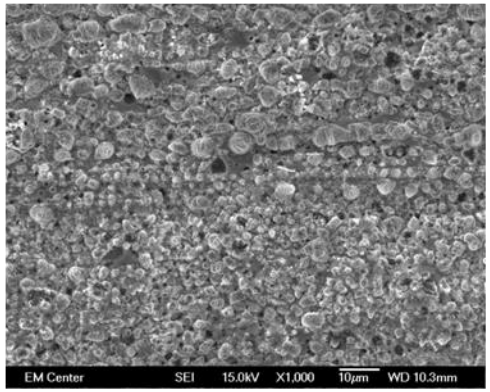

100 V

200 V

300 V

250 °C

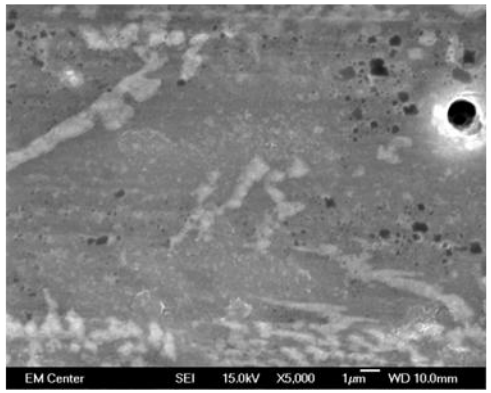

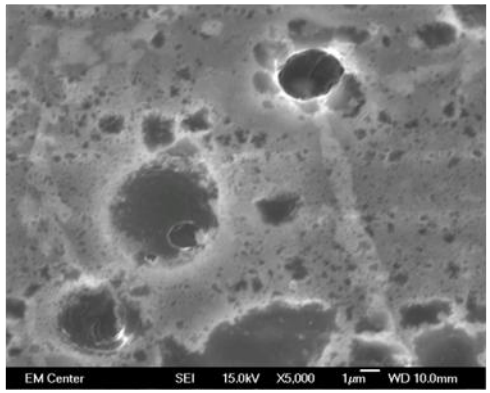

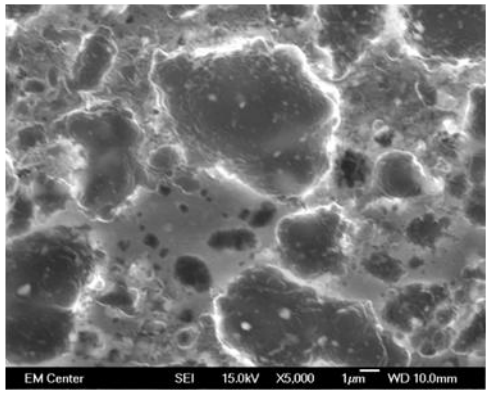

400 V

500 V

250 °C